PROZESKY, VICTOR MARCUS

THEORETICAL AND EXPERIMENTAL ASSESSMENT OF ASPECTS OF TOKAMAK CONFINEMENT

PhD UP 1992

Theoretical and experimental assessment of aspects of tokamak confinement

Victor Marcus Prozesky

Submitted in partial fulfilment for the degree PhD
in the Faculty of Science
University of Pretoria

1992

Theoretical and experimental assessment of some aspects of tokamak confinement

Candidate: Victor Marcus Prozesky

Promotor: Prof. E. Friedland

Department of Physics

Degree: PhD

Abstract

This work is a study of the importance of some of the aspects of the generally negative influence of imperfect confinement of particles and energy on a fusion plasma. In some cases, however, the imperfect confinement of impurities is necessary to keep the plasma burning. The criteria for maintaining a steady state burn condition in a reactor by linking the confinement of the helium and energy shows that steady state burn conditions can be achieved in a D,T plasma within certain limits of the ratio of helium confinement time to energy confinement time. The maximum ratio decreases sharply when impurities are included in the plasma. When profile effects are added to such a model, this ratio is not significantly affected, and for a limited one - dimensional approach the values are similar. The one - dimensional model is also compared with an exact solution of the one - dimensional diffusion equations for energy and helium.

Time dependent reactor operation is also simulated, including impurity generation as a result of the ion flux leaving the plasma and bombarding the divertor material. This study shows the crucial effect of the confinement of these impurities and helium ash in the plasma. When confined for too long in the plasma, the burn is quenched.

A new definition of the maximum impurity concentration, allowed in the plasma during steady state operation based on the zero - dimensional model, leads to strict limits on impurity concentrations allowed for the operation of a reactor in steady state conditions.

Results are presented of an experimental study of the ion loss from the plasma and subsequent bombardment of the walls and limiters in JET. The measurements

were made for the different stages of the plasma discharge, as a function of the radial distance from the plasma volume. Probes implanted with depth markers were inserted into the edge plasma of JET and analyzed after plasma exposure.

Experimental data presented on the measurement of the creation of abnormally high energy particles in the edge plasma during the application of additional heating by the ICRH (Ion Cyclotron Resonance Heating) method confirms the existence of fast particles in the edge plasma with energies ($\sim$ 1 keV) that contribute dominantly to the higher concentration of impurities in the plasma of ASDEX.

The large number of neutral particles that are created are lost from the plasma volume. These particles have several effects on the plasma, such as sputtering of the wall material with subsequent dilution of the plasma fuel and radiative losses. A simple model to describe the neutral flux from the plasma volume during ohmic discharges is presented, and the effects of sputtering of the wall material is simulated for the JET configuration as well as for ITER.

A direct effect of the neutrals bombarding the walls is their contribution to the fusion process inside the walls, and this process is discussed. The contribution of this process during discharges on JET and ITER are considered and results presented.

Teoretiese en eksperimentele studie van aspekte van tokamak inperking

Kandidaat: Victor Marcus Prozesky

Promotor: Prof. E. Friedland

Fisika Departement

Graad: PhD

Opsomming

Hierdie tesis behels die studie van die belangrikheid van sommige van die negatiewe aspekte van die invloed van onvolledige inperking van deeltjies en energie op die plasma. In teenstelling hiermee moet die inperking van die helium en ander onsuiwerhede juis onvolledig wees, om akkumulasie van onsuiwerhede te voorkom. Die kriteria vir die behoud van ewewigstoestande tydens ontbranding, deur die koppeling van die helium en energie inperkingstye, toon dat ewewigstoestande slegs bereik kan word in 'n D,T-plasma binne sekere limiete van die verhouding van heliumtot energie-inperkingstyd. Die maksimum verhouding daal skerp met die insluiting van onsuiwerhede in die plasma. As profiel - effekte tot die model toegevoeg word, word die verhouding nie noemenswaardig beïnvloed nie, en dieselfde geld vir 'n een - dimensionele benadering. Die een - dimensionele benadering word ook vergelyk met 'n eksakte oplossing van die een - dimensionele diffusievergelykings vir energie en helium.

Tydafhanklike reaktor bedryf word ook gesimuleer, met inagneming van tweede generasie onsuiwerhede as gevolg van die ione wat op die omleiermateriaal inval. Daar word getoon dat die effek van onsuiwerhede en helium krities is vir reaktorbedryf. As die onsuiwerhede en helium te goed ingeperk word, word die ontstekingskondisie nie meer bevredig nie en is ekwilibrium ontsteekte toestande nie bereikbaar nie.

'n Nuwe definisie van die maksimum toegelate onsuiwerheidskonsentrasie in die plasma word aangebied, gebaseer op die zero-dimensionele model. Die definisie lei tot streng beperkings ten opsigte van die toegelate onsuiwerheidskonsentrasies in die plasma by ewewigstoestande.

Eksperimentele resultate word ook aangebied van 'n studie van die ioonverlies uit die plasma en die gevolglike bombardering van die wande en beperkers in JET. Die metings is uitgevoer vir verskillende stadia van die plasma-ontlading, as 'n funksie van die radiale afstand vanaf die plasma. Monsters wat vooraf met dieptemerkers geïnplanteer is, is vir die doel aan die randplasma blootgestel en daarna geanaliseer.

Eksperimentele data oor die versnelling van ione in die omgewing van die antennas, wat gebruik word tydens die toepassing van addisionele verhitting deur die ICRH-metode (Ioon-siklotron-resonansverhitting), word aangebied. Die resultate bevestig die bestaan van energieke deeltjies ($\sim$ 1 keV) wat grootliks bydra tot die totale onsuiwerheidskonsentrasie in ASDEX.

Die groot aantal neutrale deeltjies wat in die plasma ontstaan, word nie ingeperk nie en ontsnap uit die plasmavolume. Die deeltjies kan onsuiwerhede van die wandmateriaal verstuif, wat tot verdunning van die brandstof en hoër stralingsverliese lei. 'n Eenvoudige model word aangebied wat die neutrale vloed tydens ohmiese verhitting beskryf, en die effek van verstuiwing word gesimuleer vir JET, asook vir ITER.

'n Direkte gevolg van die neutrale deeltjies wat die wande bombardeer, is hulle bydrae tot versmeltingsreaksies binne die wande. Hierdie proses word bespreek en die bydraes van die prosesse tydens ontladings in JET en ITER word oorweeg en die resultate aangebied.

Acknowledgements

I am very grateful to the following people:

Dr. Rainer Behrisch for the time spent working with him, his immense knowledge of the subject and his continuous support throughout this study.

Dr. D. W. Mingay for his support, trust and help. He played an instrumental role in the secondment to Garching.

Dr. G. Nothnagel who acted as supervisor for the study, for all the support during the final stretch of the study.

Prof. E. K. H. Friedland who acted as promoter of this thesis.

The AEC for giving me the oppertunity to undertake further study, and for the secondment to the Max Planck Institute which allowed the bulk of the work to be performed at Garching.

My wife Frances and the kids for their love, support and patience throughout the study.

To God for giving me the privilege to study the beautiful subject of physics.

Contents

List of Figures

List of Tables

Chapter 1

Introduction

Energy has always been of the utmost importance to the existence and development of the activities of man, especially so in the current industrial era. The sources of energy have changed over the years from firewood to the use of other fossil fuel, such as coal, oil and natural gas. More recently, solar-related and nuclear energy have been introduced.

During the last decade the advantages and disadvantages of the different energy sources have become apparent, largely due to uncontrolled increases in population and industrialisation to a scale where the entire globe is being affected. The biggest problems associated with fossil fuel are the release of CO_2 (a gas enhancing the global greenhouse effect) and sulphur, together with other potentially hazardous pollutants. Nuclear fission energy, i.e. the release of energy from splitting heavy nuclei, has always been controversial due to the large quantities of high-level radioactive waste involved and the inherent instability of the energy-releasing process, with a probability of large-scale radioactive contamination. The possible connection of nuclear reactors to military activities has also contributed to widespread opposition to fission reactors.

Although solar power (hydro, direct solar, and also bio-mass) is environmentally inherently the most desirable, it is still an open question whether this source can serve the vast energy needs of an industrial world.

An exciting alternative to fission of heavy nuclei is fusion of light nuclei to form heavier nuclei with less binding energy per nucleon, thus releasing energy in the process. Nuclear energy has potentially the largest energy release per unit mass when compared to chemical energy (fossil), and also compares favourably with solar energy, considering the large areas needed for the utilisation of the latter source of energy.

Source	Mass (grams) needed for 1 MJ of energy
Fossil	170
Fission	$9.5 \cdot 10^{-4}$
Fusion	$2.6 \cdot 10^{-5}$

Table 1.1: **Mass needed to produce 1 MJ of energy for different energy sources**

The mass needed from different energy sources to generate 1 MJ of energy is indicated in Table 1.1 [SCI90]. From this table it is clear that the fusion process uses minute quantities of fuel compared to fossil fuel, and considerably less than the fission process. The mass needed for fossil fuel was obtained considering burning of coal and the mass for the fission process was obtained considering the use of 3 % enriched ^{235}U in a light-water reactor. The fusion process considered was a deuterium - tritium (D,T) plasma, operating with a 10 % burnup of the fuel.

Fig. 1.1 illustrates the binding energy per nucleon as a function of the atomic mass of the different elements. The vast energy difference between fission and fusion reaction processes is apparent, and this is the reason for the difference in mass needed per energy unit for a fusion reactor compared to a fission reactor. This fact has led to an intensive research effort into the ultimate achievement of a commercial reactor based on the fusion of the lighter nuclei. Several other advantages exist for fusion when compared to fission. The fuel (deuterium and tritium) is obtainable in large quantities, and although the process is also inherently unstable, these instabilities tend to quench the fusion process, eliminating the possibility of a major environmental disaster.

The radioactive waste is also considerably less than for the fission process, although the release of neutrons will lead to large-scale activation of reactor components. The major disadvantage of the fusion reactor will probably be the technological skills required to operate the reactor, and the difficulty of maintenance.

1.1 Nuclear fusion

The concept of nuclear fusion has at its basis the fusing reactions of light particles, converting mass to energy, with practical application of the energy. Due to the positive charge of the nuclei, and consequently the Coulomb repulsive force between them, this barrier must be overcome or penetrated for fusion to occur. Quantum me-

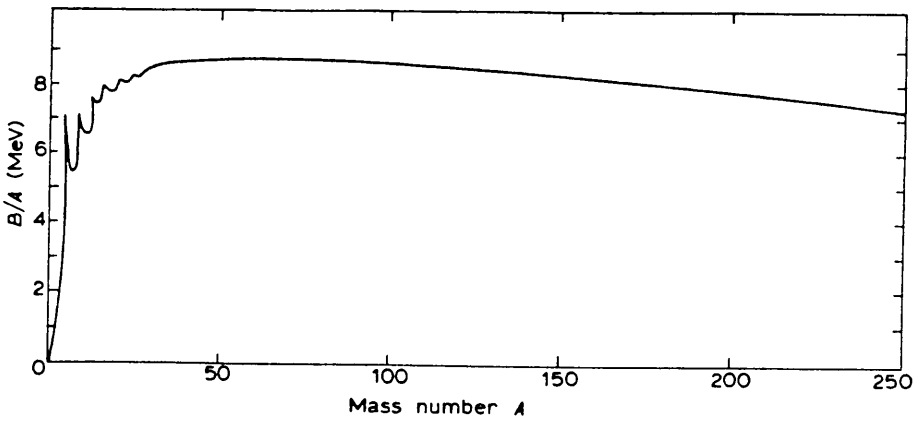

Figure 1.1: **Binding energy per nucleon as a function of atomic mass**

chanical penetration of the Coulomb barrier is permissible, but to obtain significant yields for fusion, the nuclei must be able to get very close to each other.

The process of fusion can be approached in a number of ways. The two fundamental approaches are through thermonuclear or "hot" processes, and through "cold" fusion. Cold fusion is centered around the replacement of an electron around the nucleus of one of the fuel particles by a muon, with a mass of $\sim$ 250 times that of an electron. This larger mass allows the fuel particles to approach each other to smaller separation distances, allowing the fusion process to occur at low ($\sim$ 300 K) temperatures. Cold fusion, however, still suffers from the burden that it is more energy consuming to produce muons than the energy gained from the process, considering the lifetime of the muon and consequently the number of fusion cycles a muon can be involved in.

The approaching distances between the nuclei can also be decreased by heating or by acceleration of the nuclei to energies where they can penetrate the Coulomb barrier and allow fusion reactions to take place. Thermonuclear fusion is dependent on the addition of sufficient energy ($\sim 10^8$ K) to the fuel particles to penetrate the Coulomb barrier.

The main reactions of interest are the following:

$$D + T \rightarrow \text{n (14.1 MeV)} + {}^4\text{He (3.5 MeV)} \tag{1.1}$$

$$D + D \rightarrow \text{n (2.5 MeV)} + {}^3\text{He (0.8 MeV)} \tag{1.2}$$

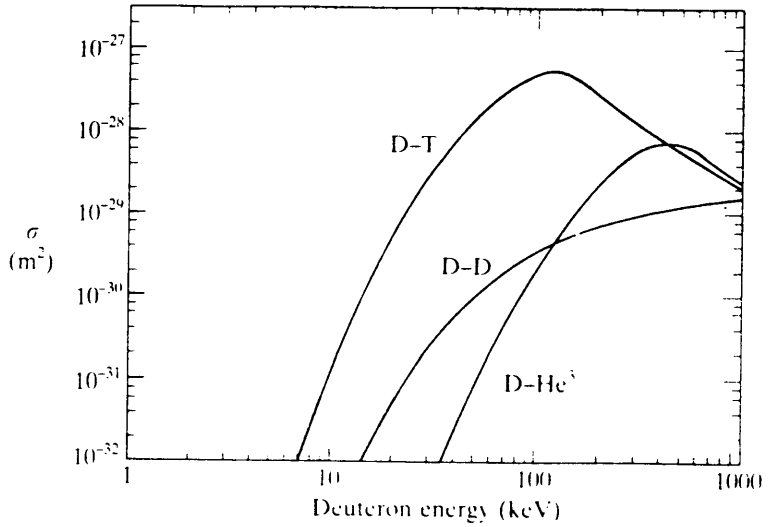

Figure 1.2: **Cross sections for reactions of interest as a function of bombarding energy**

$$D + D \rightarrow \mathrm{T}\ (1.0\ \mathrm{MeV}) + \mathrm{p}\ (3.0\ \mathrm{MeV}) \tag{1.3}$$

The energy released per reaction, ϵ_f, of these reactions are 17.59, 3.27 and 4.03 MeV respectively. There is also some renewed interest [GAL91] in the use of ^{3}He + D plasmas with the reaction of interest being the following:

$$D + {}^3\mathrm{He} \rightarrow \mathrm{p}\ (14.7\ \mathrm{MeV}) + {}^4\mathrm{He}\ (3.6\ \mathrm{MeV}) \tag{1.4}$$

The cross sections for these reactions are shown in Fig. 1.2 as a function of bombarding energy with D-D indicating the sum of the cross sections of reactions (1.2) and (1.3), the two cross sections being approximately equal.

It is clear that considerable energies must be given to the nuclei before fusion will occur, in the case of the D(T,n)^{4}He reaction this energy must be $\sim$ 100 keV. There are two options for this acceleration process, namely primary acceleration of one or both of the ion species, or the creation of a plasma, of which the energy of the particles is such as to allow fusion. In this respect the efficiency of such a process must be taken into account, as the end goal is nett production of energy. This demands that the energy used in accelerating these particles must be less than the energy released by fusion reactions. It is easy to look at simple global considerations and look at the efficiency of different mechanisms.

A first approach to thermonuclear fusion is to accelerate one of the fuel particles by some method of acceleration to interact with a target consisting of the other fuel particles, attaining fusion. A second way is to compress the fuel inertially for a short

time by implosion using an array of light or particle beams, obtaining significant fusion yields for a short time. The most studied method, however, is to heat the fuel particles to energies where they can get close enough to each other to fuse. At these temperatures the particles are in the plasma state, and therefore can be confined by magnetic fields. The merits of these three processes lie in the efficiency of the mechanism of obtaning fusion and the energy amplification of the process, i.e. the fundamental energy gain of such a reactor.

The amplification of the process of bombarding a sample with accelerated ions can be considered in the following way. The reaction with the highest energy release at low bombarding energies is (1.1). The most efficient way to obtain fusion in this scenario is to accelerate deuterium ions with an energy of $\sim$ 200 keV, impinging on a thin target of solid tritium. The ideal probability of a fusion reaction for an impinging ion is then given by:

$$P_{D,T} = \rho_T \int_{E_0-\Delta E}^{E_0} \frac{\sigma(E)}{S(E)} dE \tag{1.5}$$

with ρ_T the concentration of tritium atoms in the target, $\sigma(E)$ the cross section for the D,T reaction, $S(E)$ the stopping power of the deuterium ions in the target and ΔE the total energy loss of the deuterium ion in the target. The stopping power of the incoming ions is dominated by electronic interactions at these energies.

The energy amplification per reaction is the ratio of the energy gained ($\epsilon_{DT} \sim 20$ MeV) to the energy input, ΔE, assuming that the acceleration efficiency is 50 % and that the transmission energy of the deuterium ion is regained. Even considering the most efficient way of using this process, with a very thin target ($\sim$ 1 μm) of solid tritium ($\rho_T \sim 10^{23}$ atoms/cm^3), and being able to regain the energy of the deuterium ions that penetrated the target without nuclear interaction, the probability of obtaining a fusion event is $\sim 5{\cdot}10^{-5}$. This, in a very optimistic approach, leads to an amplification factor of $\sim$ 0.5025. This mechanism is therefore not suited to the nett generation of energy.

A simple global analysis shows that inertial confinement can yield amplification factors of order one and can thus not be ignored as a possible future means of direct fusion power production. In this thesis the emphasis is, however, on magnetic confined plasmas, which is discussed below.

1.1.1 Magnetically confined plasmas

The main drive of the thermonuclear fusion research effort, and especially the tokamak concept, is centered around the confinement of hydrogen (and/or its isotopes)

plasmas at extremely high temperatures to such a degree that a substantial number of fusion reactions take place between the fuel nuclei, thus releasing energy. These plasmas must be confined magnetically, as no material would be able to withstand these temperatures. Magnetic confinement is by no means perfect, and particles and energy are lost to the limiters and walls surrounding the plasma.

The initial energy amplification of the D,T reaction in a ($D + T + 2e^-$) plasma is $\sim$ 500 for a 10 keV plasma. Losses due to radiation are $\sim$ 50 %. Allowing 10 % burnup of the deuterium and tritium fuel, the amplification drops to $\sim$ 25. If we assume an efficiency of $\sim$ 30 % for the conversion of the energy to electricity, the final amplification is $\sim$ 8.

This analysis, although highly simplified, shows the merit of the main drive of current research on magnetically confined fusion plasmas when compared to other mechanisms, but also stresses the narrow margin of effectively operating a fusion plasma to deliver energy.

Today most of the research around the world on thermonuclear fusion revolves around magnetically confined plasmas, and especially around the tokamak concept of heating and confinement. The tokamak, an acronym originating from the Russian words "toroidal'naya kamera" and "magnitnaya katushka", meaning toroidal chamber and magnetic coil, is based on the creation of a plasma in a toroidal chamber. In 1950, almost 20 years before the tokamak concept achieved the recognition it has today, the Soviet scientists A. D. Sakharov and I. E. Tamm originated the idea of a plasma-containing device where a large current flowing axially around the torus produces an essential part of the confining magnetic field.

This was foreseen to be obtained by creating the current directly in the plasma using the inductive method, and this was the origin of the basic principle of all tokamak devices. Another method of confining plasmas magnetically without the need for the inductive current is by stellarators where the magnets that create the toroidal field are designed to also have a poloidal field component to create the helical field lines needed for stabilisation of the plasma.

By the end of the 1960's, the Soviet experiments done on tokamaks had revealed that this concept had shown the biggest promise in the quest for fusion, and after their results were confirmed by Western scientists, an extensive process of tokamak construction and research started.

With the fusion approach based on magnetic confinement of plasmas, the reaction rates ($\langle \sigma v \rangle$) of the reactions mentioned in section 1.1, based on Maxwellian velocity distributions of the plasma ions, are of interest in the choice of the preferred fuel. The fusion power (P_{Fus}) obtained is dependent on the energy release per reaction (ϵ_f) and reaction rate at obtainable temperatures in the following way:

$$P_{Fus} \propto \langle \sigma v \rangle \epsilon_f$$

The fusion power as a function of plasma temperature is shown for these reactions in Fig. 1.3 and it is clearly seen that the D + T reaction is the most appropriate in terms of achievable temperatures and energy efficiency. The D + ^{3}He plasma is of interest due to the much smaller number of neutrons produced in the fusion process (only in the D + D reactions) and also because the total fusion power of reaction (1.2) can be contained in the plasma as the resulting ions are thermalised very quickly, and contribute to the maintenance of the plasma temperature. The smaller number of neutrons lead to much lower levels of activation, which is environmentally much more desirable. The higher temperatures needed to obtain significant fusion rates are, however, making this reaction a doubtful candidate for a fusion reactor. This is due to the technological problems presented by higher temperatures and the extraction of the fusion energy from the plasma to generate electricity.

On the other hand, in reaction (1.1) most of the energy is lost from the plasma volume through the loss of the energetic neutrons which only lose a small fraction of their energy in the plasma before escaping. These neutrons can be stopped in a lithium blanket and their energy transformed to a more useful form.

Although the use of tritium is planned for future fusion programmes [KEI90], and has been introduced in JET (the Joint European Torus, which is the world's largest tokamak in Culham, England), current fusion programmes are centered around the use of deuterium plasmas, due to their relative safety of use (tritium is radioactive) and the fact that the magnetically confined plasma properties are mainly dependent on the charge of the ions, therefore showing the same plasma properties as a D,T plasma.

The confinement of the ions and energy in a tokamak is far from being perfect, and losses of particles and heat still pose the most important problems in fusion research. The energy must be confined long enough to maintain burning of the plasma, and the loss of particles from the plasma leads to interaction of these particles with the plasma-facing components of the tokamak. On the other hand the confinement time of the ash (reaction products) must be limited to avoid poisoning of the plasma fuel.

The magnetic field lines must be closed to allow the plasma particles to be contained, and the last closed flux surface is generally defined in a tokamak by material limiters, or the plasma is diverted into a remote chamber and allowed to bombard specially designed plates to transfer the energy load.

The interaction of these particles with the limiting devices, or divertor plates of the tokamak, leads to several undesirable effects on the plasma. The main problem is

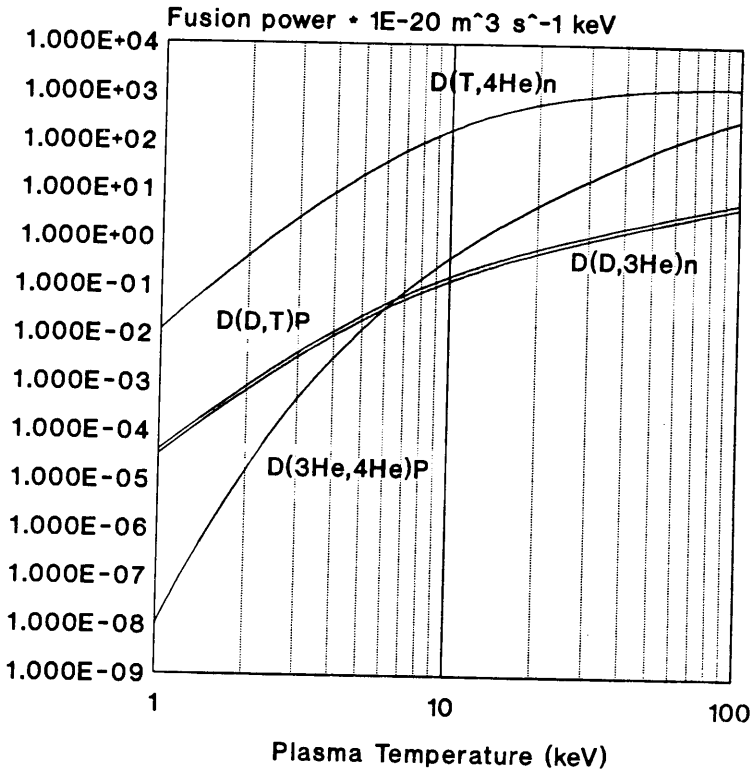

Figure 1.3: **Fusion power for different fusion reactions as a function of plasma temperature**

the release of material from these devices, and the subsequent contamination of the plasma by impurities. This leads to dilution of, and higher radiation losses from the plasma.

Other fundamental processes also play a role in these ion-solid interactions, such as reflection of the ions, trapping in the material which has an effect on the fuel inventory for the tokamak, sputtering processes, desorption of particles from the material surface, etc. These mechanisms are today still being studied in depth to yield a better understanding of their contributions to processes in tokamaks.

The main emphasis in this thesis will be to study the importance of some aspects of imperfect confinement of particles and to relate the findings to tokamak operation, with the ultimate goal of operation as a fusion reactor in steady-state conditions.

Firstly the criteria for maintaining a steady-state burn condition in a reactor are discussed. Global analyses are made of the energy confinement needed to sustain the burn, and this is coupled to the need for ^{4}He ash removal from the plasma. The study is then extended to provide a new definition of the critical concentration of impurities in such a reactor. Time-dependent operational conditions are also considered, including the generation of impurities from the plasma-facing components. The global analysis is also compared to a one-dimensional analysis of the transport of energy and helium, and conclusions are drawn.

Secondly, results are presented of an experimental study of ion loss from the plasma and subsequent bombardment of the walls and limiters of the JET tokamak. The effects of these ions which leave the plasma due to the imperfect confinement of the plasma were experimentally studied for the different stages of a plasma discharge, as a function of the radial distance from the plasma volume. The study was made by inserting probes into the edge plasma of JET. These probes were pre - implanted with molybdenum markers at a specific depth to study deposition and erosion processes, and the exposed probes were analysed with nuclear techniques based on the Van de Graaff accelerator at Garching. The results are presented and conclusions are drawn.

Thirdly, experimental data are presented on the measurement of the creation of abnormally high energy particles in the edge plasma during the application of additional heating by the Ion cyclotron resonance heating method (ICRH). These measurements were made following the detection of higher concentrations of impurities during ICRH heating periods in the tokamak ASDEX (Axisymmetrical Divertor Experiment) in Garching. The results confirm the existence of fast particles in the edge plasma with energies ($\sim$ 1 keV) that roughly corresponds to the maximum of the sputtering yield for typical wall materials, thus contributing dominantly to the higher concentration of impurities in the plasma of ASDEX.

Fourthly the thesis considers the large number of neutral particles that are created in the plasma volume, and as these particles are not confined by the magnetic field, they are lost from the plasma volume. These particles have several effects on the plasma, such as sputtering of the wall material with subsequent dilution of the plasma fuel as well as radiative losses. A simple model to describe the neutral flux from the plasma volume during ohmic discharges is presented. The model considers the contribution of gas fuelling and pellet fuelling to the creation of energetic charge exchange neutrals escaping from the plasma.

Finally, a direct effect of the particles, ions and neutrals, bombarding the limiting devices and walls is discussed. The effect of neutral fuel particles lost from the plasma through charge exchange processes leads to bombardment of the fuel-rich surface layers of the walls, and their contribution to the fusion process is discussed. The charge-exchange neutral distribution has a high energy tail, especially during neutral fuel injection, which allows fusion to take place when these particles escape from the plasma and bombard the tokamak wall. The contribution of this process during discharges on JET was considered, and results are presented.

Chapter 2

The tokamak as plasma device

The basic features of the tokamak are illustrated in Fig. (2.1). The plasma column is contained in a toroidal chamber, and the plasma is confined in this chamber by magnetic fields. Magnetic coils are placed around the torus, and these magnets create the toroidal field for particle confinement. This field is, however, not sufficient to create a stable plasma configuration, necessitating the use of an extra poloidal magnetic field. There is of course still a third field, the vertical magnetic field, needed for stable operation.

The poloidal field is produced by inducing a toroidal current in the plasma itself through transformer action, with the plasma being the secondary winding of the transformer. The electrical field induced by current flowing in the primary windings drives the plasma current, and produces the poloidal magnetic field. In the same action the plasma is also resistively heated by the current flowing in the plasma. Since transformer action is obtained by increasing the magnetic flux through the core, which can only be accomplished for a limited time, the tokamak is inherently a pulsed device. The resulting magnetic field is helical in shape, and the poloidal field therefore prohibits charge separation between the top and bottom of the plasma, which would otherwise lead to instabilities in the plasma.

The concept of plasma temperature will be used throughout the thesis, necessitating a clear definition of the temperature of a plasma. A gas in thermal equilibrium has particles of all velocities, with the Maxwellian velocity disribution described by the following equation, assuming one dimensional dependence:

$$f(v) = A \cdot \exp(-\frac{\frac{1}{2}mv^2}{kT}) \tag{2.1}$$

where $f(v)$ is the number of particles per volume unit with velocity between v and

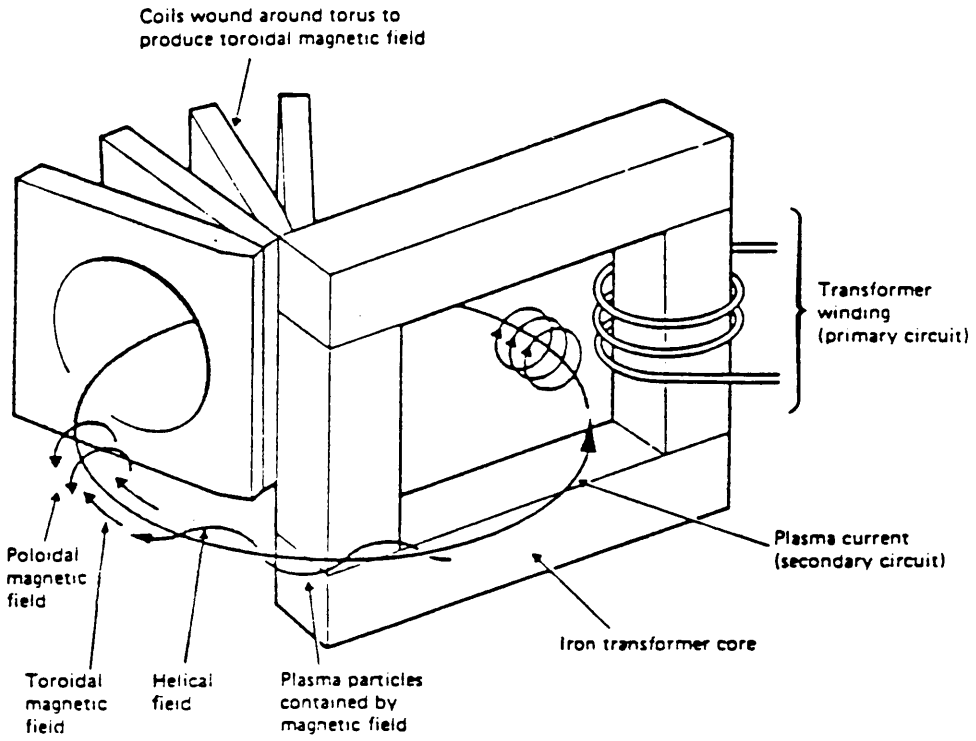

Figure 2.1: **Basic features of tokamak configuration**

$v + dv$. The kinetic energy is described by $\frac{1}{2}mv^2$, and the gas temperature by T in ^oK. The introduction of k, the Boltzmann constant, allows the expression of the plasma temperature in terms of energy units (joule). The value of k is:

$$k = 1.38 \cdot 10^{-23} J/^oK \tag{2.2}$$

Throughout the thesis the temperature will be indicated by kT (in joule) except in the use of specific values in examples and results, where it is useful to express the temperature in eV obtained from $\frac{kT}{e}$ where e is the electron charge, equal to $1.602 \cdot 10^{-19}$ J/eV. These values are often used to describe the temperature under typical tokamak conditions. When the plasma temperature is refered to in eV, the quantity $\frac{kT}{e}$ is used.

2.1 Plasma edge phenomena

One fundamental characteristic of a plasma is the formation of a sheath at the material/plasma interface of an electrically isolated body. When such a body is inserted into a plasma, it is subject to bombardment by all particles in the plasma. The smaller mass of the electrons, and consequently the higher mobility, results in the electron random flux to the material being much larger than the ion flux. The result is a negative nett charge on the material. This charge repels electrons and attracts the ions to the surface, and equilibrium is reached when the potential is such that the electron and ion fluxes to the material are equal.

This potential drop, ϕ, is limited to a small distance from the surface of the material, called the sheath. This sheath thickness is of the order of the Debye length, which is given by:

$$\lambda_D = \left[\frac{kT_e}{4\pi n e^2}\right]^{\frac{1}{2}} \tag{2.3}$$

with kT_e the plasma edge temperature and n the plasma density. This length is normally very small, typically tens of microns for plasma edge conditions in tokamak experiments.

The plasma edge of a tokamak can therefore be schematically demonstrated by Fig. (2.2). In this case the tokamak has limiters determining the last closed flux surface (LCFS). The magnetic field surfaces radially outward from the limiters are not closed and intersect the limiters, leading to particle bombardment of the limiters. This region is defined as the scrape off layer (SOL). In the SOL the transport is

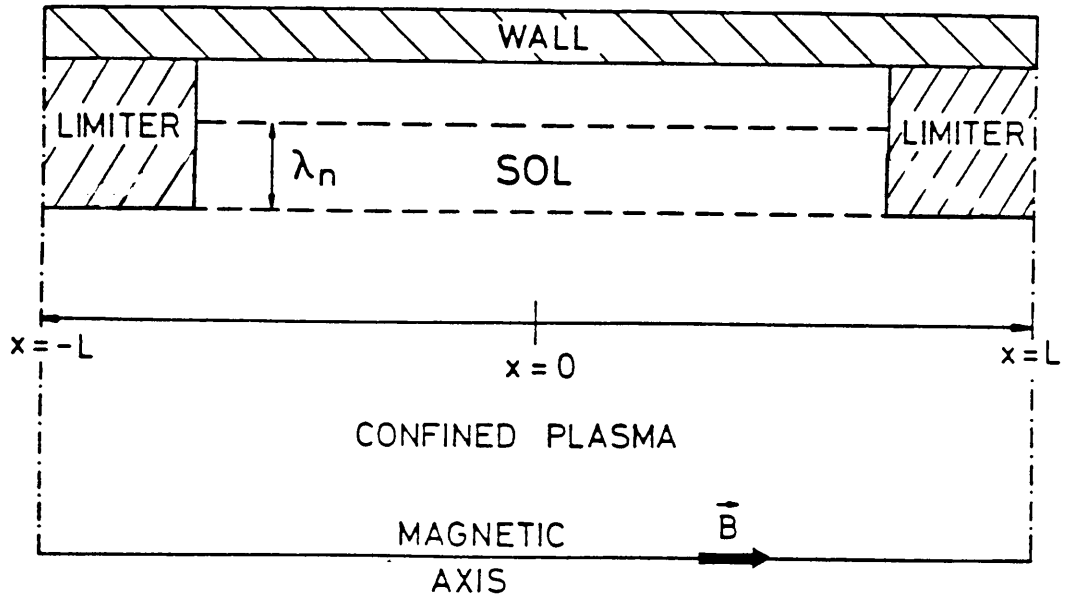

Figure 2.2: **The SOL and the main plasma**

dominated by fast transport along the magnetic field lines, and slow diffusion across the magnetic field lines. This has the result that the radial extent of the plasma in the SOL is much less than the toroidal connection length between the limiters.

For steady-state conditions in the SOL, the particle continuity equation is given by:

$$\vec{\nabla} \cdot (n\vec{v}) = S \tag{2.4}$$

and the full ion momentum equation by:

$$m_i n(\vec{v} \cdot \vec{\nabla})\vec{v} = Zen(\vec{E} + \vec{v} \times \vec{B}) - \vec{\nabla} \overline{\overline{p}}_i - \frac{m_i S\vec{v}}{Z} \tag{2.5}$$

with n the plasma density, $\vec{v}$ the plasma flow velocity, $\vec{B}$ the magnetic field, S the source strength in the SOL due to cross particle transport, $\vec{E}$ the electric field (also parallel to $\vec{B}$), $\overline{\overline{p}}_i$ the ion pressure tensor, and Ze and m_i the charge and mass of the plasma ions respectively.

In one dimension the plasma pressure due to the ions and the electrons is given by:

$$p_i = n_i k T_i \tag{2.6}$$

$$p_e = n_e k T_e \tag{2.7}$$

with kT_i and kT_e the ion and electron temperatures in the plasma. The electric field strength is given by:

$$E = -\frac{d\phi}{dx} \tag{2.8}$$

with ϕ the potential drop between the plasma and the material.

The electron momentum equation, equivalent to the ion momentum equation, can be written in one dimension with the distance x:

$$en_eE = -\frac{dp_e}{dx} \tag{2.9}$$

where terms containing the small quantity m_e were neglected. This equation can be solved [DOL82] to show that the electron density in the SOL satisfies the Boltzmann relation:

$$n_e = n_0 e^{\frac{e\phi}{kT_e}} \tag{2.10}$$

with n_0 the density at the point where $\phi = 0$, i.e. the plasma centre.

Returning to the ion momentum equation, and assuming one-dimensional geometry, we can use (2.8) and (2.6) together with the Boltzmann relation to obtain:

$$\frac{dM}{dx} = \frac{S}{nc_s}\frac{1+M^2}{1-M^2} \tag{2.11}$$

where $M = \frac{v}{c_s}$, with

$$c_s = \sqrt{\frac{k(T_i + ZT_e)}{m_i}} \tag{2.12}$$

the ion acoustic speed. Assuming that the flow in the SOL is subsonic, i. e. $v < c_s$, then $\frac{dM}{dx} > 0$ since $\frac{S}{nc_s}$ is inherently positive.

At $M \rightarrow \pm 1$, $\frac{dM}{dx} \rightarrow \infty$. This corresponds to the formation of the sheath at the plasma-limiter interface, and the break-up of the plasma, i.e. where quasi-neutrality becomes violated. Thus the ions are accelerated through the SOL, the fluid velocity rises from 0 at the symmetry point towards the ion acoustic speed at the sheath edge. At the sheath the acceleration becomes very large as the ions experience the strong electric field in the sheath, and the plasma quasi-neutrality condition breaks down. These results place a limit on the velocity of the ions entering the sheath, namely $v \leq c_s$.

Bohm [BOH49] showed in an analysis of the sheath that the ion should enter the sheath with at least the ion acoustic speed, i.e.,

$$v \geq c_s$$

The conclusion can now be drawn that the ions enter the sheath with the ion acoustic speed, referred to as the Bohm Criterion.

The behaviour of M, n and ϕ with x can now be investigated. The equations (2.4) to (2.11) can be rewritten to the form:

$$\frac{n(M)}{n_0} = \frac{1}{1+M^2} \tag{2.13}$$

and

$$\frac{e\phi(M)}{kT_e} = -ln(1+M^2) \tag{2.14}$$

The values of n and ϕ at the sheath edge ϕ_s can be obtained from substituting the value of $M = 1$ from the Bohm criterion:

$$n_s = \frac{1}{2}n_0 \tag{2.15}$$

$$\phi_s = -ln(2)\frac{kT_e}{e} \approx -0.69\frac{kT_e}{e} \tag{2.16}$$

The quantities M, $\frac{e\phi}{kT}$ and $\frac{n}{n_0}$ for the bulk plasma and for the SOL are shown in Fig. 2.3.

Considering a plasma flux tube in the SOL terminated at each end by a limiter, and neglecting ionisation, the source of particles is from cross-field diffusion. This is described by:

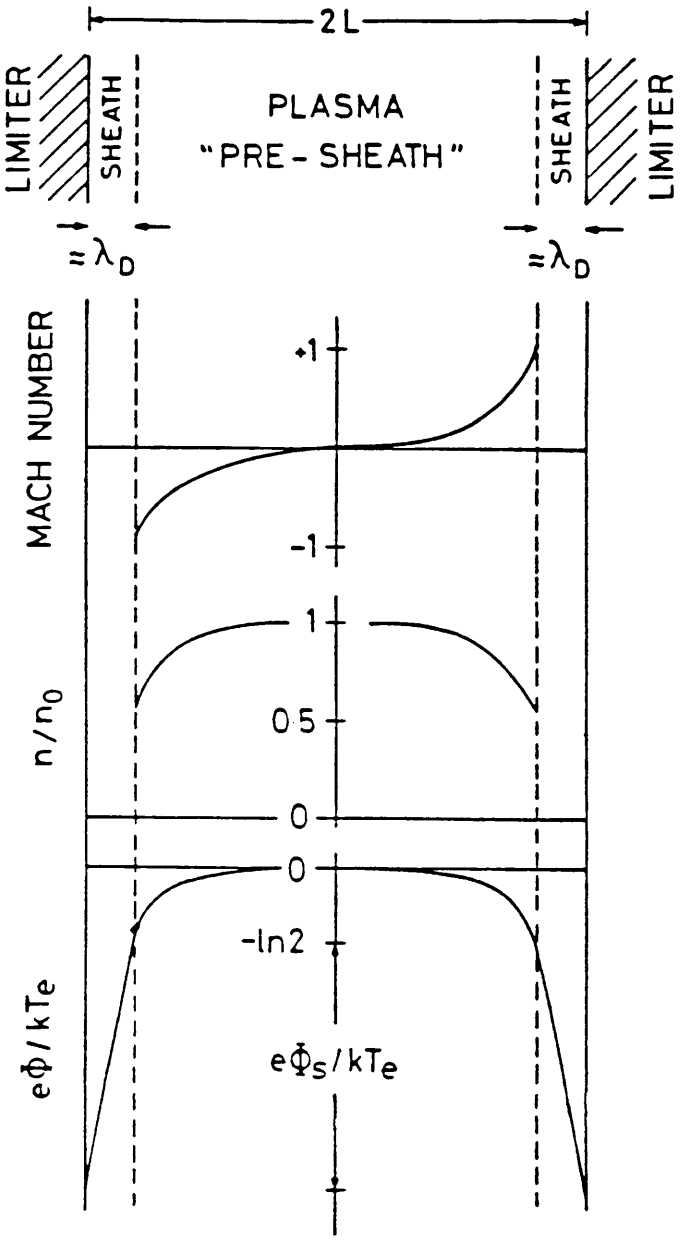

Figure 2.3: **Plasma spatial variations of density n, Mach number M and potential, ϕ, within the SOL**

$$\Gamma_\perp = -D_\perp \frac{dn}{dr} \tag{2.17}$$

with $D_\perp$ the anomalous cross-field diffusion coefficient. The particle balance as a result of the divergence of the cross-field flux, and the particle loss to the sheath are given by:

$$\frac{d}{dr}[D_\perp \frac{dn}{dr}] = \frac{c_s}{2L} n \tag{2.18}$$

with $2L$ the connection length between the limiters. It is normally found in the SOL that kT_e and kT_i decrease more slowly than n with minor radius, and we assume therefore that c_s(r) is constant. Assuming that $D_\perp$ is also constant we find:

$$\frac{d^2n}{dr^2} = \frac{1}{\lambda_n^2} n \tag{2.19}$$

with the scrape-off layer length λ_n, also called the e-folding length due to the exponential dependence, given by the following:

$$\lambda_n = \sqrt{2D_\perp \frac{L}{c_s}} \tag{2.20}$$

The definitions and quantities given above for the SOL will be used in analyzing results in this thesis.

Chapter 3

Particle and power exhaust for a D,T fusion plasma

3.1 Introduction

Major efforts are currently under way to develop and demonstrate designs for experimental test fusion reactors such as the International Toroidal Experimental Reactor (ITER). To obtain an ignited continuously burning thermonuclear D,T plasma [TOM88] the problems of particle and power exhaust have become of increasing concern. For such a burning fusion plasma the energy confinement has to be sufficiently good to fulfil the burn criterion [LAW57,MEA74]. However, the confinement must not be better than what is required by this criterion in order to prevent the plasma from overheating, and the helium particle confinement must be limited so that poisoning with too high an ash concentration is avoided. That is, $\frac{\tau_{He}}{\tau_E}$ must be as low as possible with $n_e kT\tau_E$ just satisfying the burn criterion, with τ_{He} the helium confinement time and τ_E the energy confinement time.

In today's plasma experiments the helium particle diffusion coefficient D_{He} is only now being investigated [HAW89,SIP89,FIN90]. In general the particle diffusion coefficient D, of the plasma ions, is found to be smaller than the energy diffusion coefficient χ by a factor of about 1 to 12 [SIP89,BEC88,BEC84,LOM89], and thus the particle confinement time is larger than the energy confinement time by about this factor. The particle and energy transport is experimentally found to be closely coupled [HOG90,BRO90,GON89].

During a workshop on helium transport and removal in Gatlinberg during April 1991 the first experimental results of helium removal were reported. Synakowski *et al.* [SYN91] reported from experiments, that although the ratio of energy diffusivity

Tokamak	He fuelling	Plasma edge	Conf. regime	Results
TEXT	He - plasma	Limiter	L	Transport caused by electrostatic turbulence
TEXTOR	Gas	Pumped limiter	L Polarisation mode	$\tau_\alpha^* \approx 1$ s, $\frac{\tau_\alpha^*}{\tau_E} \leq 2.4$ τ_α^* increases
TFTR	Gas	Limiter	L/supershot	$\chi_{He} \approx 3$ m^2/s, $D_{He} \approx (0.1 - 1)\chi_i$
D-III	Gas (Ar)	Exp. boundary	L	Strong Ar exhaust
JT-60	Gas/Beam	Divertor	L	Enrichment factor ≤ 1
JET	Beam 7kA/ 120keV	Divertor	L/H	$\Gamma/\nabla n \approx 0.5$ m^2/s

Table 3.1: **The state of experimental knowledge on helium transport and exhaust**

to the helium diffusion coefficient is machine specific, values of $\frac{\chi}{D_{He}} \approx 0.5$ - 2 were typical. Hillis *et al.* [HIL91] reported that the experimental database from TEXTOR for L mode discharges indicate that this ratio is less than 2.4. They found the energy and helium transport to be closely coupled for all experiments. This coupling is expected to be amplified in a burning reactor, due to the origin of the helium in a reactor as opposed to external helium fuelling in the TEXTOR experiments. From modelling of the intrinsic helium diffusion in TEXTOR, Hogan *et al.* [HOG91] found that $\frac{\tau_{He}}{\tau_E} \approx 1$ - 3, which is compatible with the experimental results. Recycling of helium, however, will tend to increase this ratio.

The results presented at the workshop is summarised in Table 3.1 [BOS91].

Nakamura *et al.* [NAK91] measured D_{He} absolutely on JT-60 for core fuelling with 30 keV helium beams, finding that $D_{He} \approx 0.4$ m^2/s. Chang [CHA91A] modelled preferential ICRH removal of helium, and found no degradation of the energy confinement. Their results led to values of $\frac{\tau_{He}}{\tau_E} < 1$, a positive result for preferential removal of helium. About 30 MW of ICRH, which is achievable in practice, will be needed to remove the helium from the ITER core to acceptable levels.

In today's plasma experiments, however, impurity ions with a higher charge than the hydrogen ions tend to accumulate in the plasma centre [FUS89]. Here the ions diffuse inward from the edge of the plasma, and unlike helium, are not created in the plasma volume. The experimental results on helium removal tend to show no such accumulation of helium at the centre, although transport in a burning reactor

may be different due to the different origin of the helium. These results are positive for reactor operation, although recycling of helium at the vessel walls and limiters or divertors [REI90,RED89] (not explicitly included in the analysis presented in this thesis) will tend to increase the helium particle density at the edge and consequently that of the bulk plasma.

As a starting point in discussing the helium confinement problem a zero-dimensional model is presented in section 3.2 to show the limitations imposed by helium production in coincidence with the energy, and the effect of finite confinement of both energy and helium on burning D,T fusion reactor conditions.

3.2 The Burn and exhaust Criterion

The first criterion for the determination of an ignited operational state of a fusion reactor was made by Lawson [LAW57], where he obtained a criterion for steady-state burning, requiring that the effective fusion power must exceed the power losses. The fusion parameter $n_e\tau_E$ (i.e. the product of the electron density and energy confinement time) was found to have to exceed at least 10^{22} s/m^3 at a plasma temperature of 20 keV to maintain burn.

While the burn criterion determines the required values of the confinement parameters $n_e\tau_E$, the exhaust criterion determines the maximum values of $n_e\tau_{He}$ (i.e. the product of the electron density and helium confinement time) for a given helium concentration in the plasma. These two criteria are closely coupled, and are defined in the equations below [BEH90A].

Using a zero-dimensional model for a burning fusion plasma with a D,T particle density, $n_D = n_T = n = \frac{1}{2}n_{D,T}$, the increase in helium and the simultaneous decrease in the fuel density are given by [ART64,GLA64]

$$\frac{dn_{He}}{dt} = \frac{n_{DT}^2\langle\sigma v\rangle_{DT}}{4} \tag{3.1}$$

where $\langle\sigma v\rangle_{DT}$ is the D,T fusion reaction rate obtained by averaging the D,T cross section over a Maxwellian velocity distribution [ART64,GLA64,MIL74] and n_{He} is the helium density. For a plasma not in thermal equilibrium, other appropriate velocity distributions must be used.

If the helium produced in fusion reactions is confined in the D,T plasma for a time τ_{He}, we have the following particle balance equation:

$$\frac{dn_{He}}{dt} = \frac{n_{DT}^2 \langle \sigma v \rangle_{DT}}{4} - \frac{n_{He}}{\tau_{He}} \tag{3.2}$$

The densities of D and T are assumed to be kept constant by refuelling. If the density of helium ions in the burning D,T plasma is a fraction f of the fuel density, i.e. $n_{He} = f n_{DT}$, and stationary conditions are assumed, eq. (3.2) yields:

$$n_{DT} \tau_{He} = \frac{4f}{\langle \sigma v \rangle_{DT}} \tag{3.3}$$

For a quasi-neutral plasma the electron density is given by

$$n_e = n_{DT}(1 + 2f + \sum_i f_i Z_i) \tag{3.4}$$

with $f_i = \frac{n_i}{n_{D,T}}$ the concentration of impurities with charge state Z_i. Introducing eq. (3.4) into eq. (3.3) gives for the exhaust criterion

$$n_e \tau_{He} = \frac{4f(1 + 2f + \sum_i f_i Z_i)}{\langle \sigma v \rangle_{DT}} \tag{3.5}$$

For a 10 keV D,T plasma the fusion reaction rate is $\langle \sigma v \rangle_{DT} \approx 10^{-22}$ m^{3}s^{-1} [ART64, GLA64,MIL74]. If the maximum helium concentration in the plasma is 5 - 10 % [TOM88] and if there are no other impurities, $n_e \tau_{He} = 2.2 \cdot 10^{21}$ to $4.8 \cdot 10^{21}$ m^{-3}s.

According to the burn criterion for a D,T fusion plasma [MEA74], during a given energy confinement time, τ_E, the energy density of the produced helium ions (they are assumed to be immediately thermalised in the plasma) minus the energy density radiated from the bulk plasma by bremsstrahlung, recombination, line radiation and other radiative losses, must be equal to the energy density lost by convective and conductive heat transport [MEA74]:

$$(P_\alpha - P_{Brems} - P_{rad})\tau_E = \frac{3}{2}(n_e k T_e + n_{DT} k T_i + \sum_i n_i k T_i) \tag{3.6}$$

with P_{Brems} the bremsstrahlung losses and P_{rad} includes in general recombination, line and cyclotron radiation, and charge-exchange power losses. It is also assumed that any external power applied to the plasma is negligible when compared to the helium particle power.

The helium particle power density due to the fusion reactions is

$$P_\alpha = \frac{n_{DT}^2 \langle \sigma v \rangle_{DT} E_\alpha}{4} \tag{3.7}$$

Inserting relation (3.4) into (3.7), it is found that:

$$P_\alpha = \frac{n_e^2}{4(1 + \sum_i f_i Z_i)^2} \langle \sigma v \rangle_{DT} E_\alpha \tag{3.8}$$

with $E_\alpha = 5.63 \cdot 10^{-13}$ J (= 3.52 MeV). In the following we omit cyclotron radiation from P_{rad}, which is important only at plasma temperatures above about 25 keV [TAY90], as well as power losses due to charge-exchange neutrals leaving the plasma volume. It will later be shown (section 3.5) that this is not a serious limitation, as the operation of a tokamak reactor suffers from other limitations such as the β-limit and power dissipation on the divertor plates, which also tend to generally limit temperatures to less than 30 keV.

The bremsstrahlung, line radiation and recombination radiation depend on the square of the electron density. For the radiation losses of the D, T, helium ions and low Z impurities ($Z \leq 6$), only bremsstrahlung losses were used [GLA64], [RAE81] with the numerical factor given in [MEA74] and the Gaunt factor ($g(Z^2/kT)$) equal to unity. The Gaunt factor is a quantum mechanical correction term and for conditions of interest, $g \approx 2\sqrt{3}/\pi$ [WES87]. The bremsstrahlung power density is given by:

$$P_{Brems}(\mathrm{J \cdot s^{-1} \cdot m^{-3}}) = 3.842 \cdot 10^{-29} \sqrt{kT} n_e (n_{DT} + 4n_{He} + \sum_i n_i Z_i^2) \tag{3.9}$$

Here equal temperatures for all particles in the plasma volume were assumed, with the plasma temperature kT in J and the densities n in $\mathrm{m^{-3}}$. Inserting relation (3.4) into (3.9), we obtain for the bremsstrahlung of D, T and helium:

$$P_{Brems} = \frac{n_e^2}{(1 + 2f + \sum_i f_i Z_i)} B \tag{3.10}$$

with

$$B = 3.842 \cdot 10^{-29} \sqrt{kT}(1 + 4f) \tag{3.11}$$

For the radiation of heavier impurities in the plasma, i. e. $Z_i > 6$, the approximation proposed by Vernickel and Bohdansky [VER78], [ROT90] was used:

$$P_{rad}(\mathrm{J}\cdot\mathrm{s}^{-1}\cdot\mathrm{m}^{-3}) = \sum_i n_e n_i (1+0.3kT)10^{-37} Z_i^{(3.7-0.33ln(kT))} \tag{3.12}$$

with kT in keV and n in m^{-3}. Inserting relation (3.4) into (3.12):

$$P_{rad} = \frac{n_e^2}{(1+2f+\sum_i f_i Z_i)} R \tag{3.13}$$

with

$$R = (1+0.3kT)10^{-37} \sum_i f_i Z_i^{(3.7-0.33ln(kT))} \tag{3.14}$$

Using eqs. (3.4), (3.7), (3.8), (3.10), (3.13), and $T_e = T_i = T$, relation (3.6) can be transformed to obtain the usual form of the burn criterion:

$$n_e\tau_E = \frac{\frac{3}{2}kT(2+3f+\sum f_i(Z_i+1))}{\frac{\langle\sigma v\rangle_{DT}E_\alpha}{4(1+2f+\sum f_i Z_i)} - (B+R)} \tag{3.15}$$

If no impurities and no helium are present, i.e. if $f_i = f = 0$, the burn criterion simplifies to:

$$n_e\tau_E = \frac{12kT}{\langle\sigma v\rangle_{DT}E_\alpha - 12.13\cdot 10^{-15}\sqrt{kT}} \tag{3.16}$$

Eq. (3.15) represents the burn criterion as derived in [MEA74], where it was called "ignition criterion".

The exhaust criterion eq. (3.5) and the burn criterion eq. (3.15) can be combined in order to eliminate the explicit presence of the fusion reaction rate $\langle\sigma v\rangle_{DT}$ and to obtain a relation between the ratio of the particle confinement time and the energy confinement time, the helium concentration, the concentration of other impurities in the fusion plasma and the plasma temperature:

$$\xi = \frac{\tau_{He}}{\tau_E} = \frac{fE_\alpha - n_e\tau_{He}(B+R)}{\frac{3}{2}kT(2+\sum f_i(Z_i+1))} \tag{3.17}$$

This equation together with eq. (3.5) may also be arranged to obtain the helium concentration f as a cubic function of the plasma temperature, the ratio between

particle confinement time and the energy confinement time, and the impurity concentration.

The ratio (ξ) can also be rewritten to include the fusion reaction rate $\langle\sigma v\rangle_{DT}$:

$$\xi = \frac{2f[E_\alpha - \frac{4(1+2f+\sum f_i Z_i)(B+R)}{\langle\sigma v\rangle_{DT}}]}{3kT(2+3f+\sum f_i(Z_i+1))} \tag{3.18}$$

If helium, impurities and radiation losses are neglected, eqs. (3.17) and (3.18) reduces to:

$$\xi = \frac{\tau_{He}}{\tau_E} = \frac{fE_\alpha}{\frac{3}{2}kT(2+3f)} \tag{3.19}$$

A similar relation has been used in the ITER design [COP80]. It shows that for a pure D,T plasma at a temperature of 10 keV and a helium concentration of 5 - 10 %, the ratio between the particle confinement time and the energy confinement time may be as high as 5 - 10.

3.2.1 Results

The ratio $\frac{\tau_{He}}{\tau_E}$ from eq. (3.17), which includes radiation and the helium exhaust (3.5), is plotted as a function of the plasma temperature in Fig. 3.1 for a D,T plasma with a helium concentration of $f = 0.1$ and different additional impurity concentrations. The figure shows that, only for the case of no impurities and in a narrow temperature interval around about 8 keV, this ratio can be as high as 9. For the maximum of $\frac{\tau_{He}}{\tau_E}$ the peak value occurs at $\sim$ 7 keV. Previously, when the definition for the helium concentration of $f = \frac{n_{He}}{n_e}$ was used [REI90], they found this value to be $\approx$ 14. This difference results from the helium concentration f as a fraction of the total number of electrons in the plasma, and not only of the fuel ions, therefore with helium present their definition leads to less strict constraints. When impurities are included as well as with any change in plasma temperature, ξ decreases sharply.

In comparing the values of $n_e\tau_E$ and of $n_e\tau_{He}$, the relation between the particle confinement time and the energy confinement time has to be explicitly considered. The energy and the helium particles are deposited in about the same volume of the plasma where the helium ions come to rest. Thus the global confinement times should in general be inversely proportional to the corresponding diffusion coefficients χ and D_{He} of the energy and the helium ions in the plasma. Although the edge

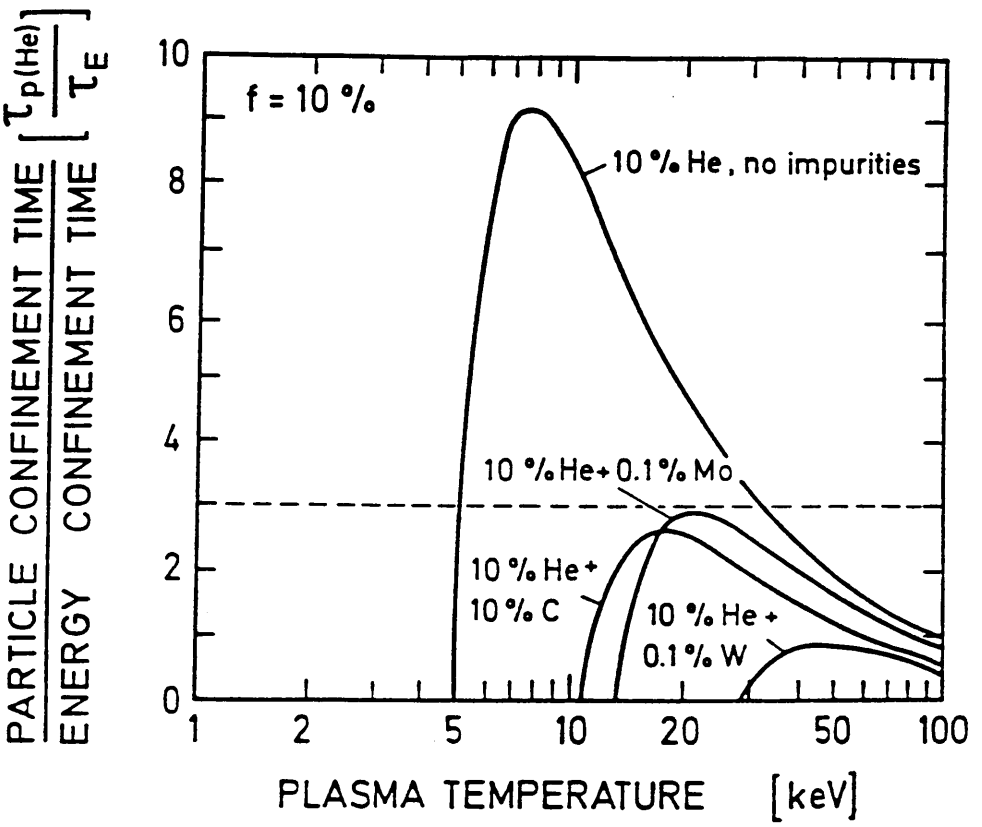

Figure 3.1: **Ratio between the helium particle confinement time and the energy confinement time, for a steady-state burning D,T fusion plasma with a helium concentration of $f = 0.1$ and different additional impurity concentrations. The dashed line indicates the ratio of 3.**

density of helium is not covered in this analysis, it is required implicitly that not only the plasma temperature, but also the helium density at the edge of the plasma volume, i.e. at the wall, has to be low due to the relation between the central and edge density inherent in tokamaks [ENG78]. This implies that the recycling coefficient of helium should be low, which may be difficult to fulfil, especially for helium [KAU85].

Since only the exhaust of the helium ions enters the equations and is therefore important, the allowable maximum values for the general particle confinement time $\tau_{D,T}$ may be larger, provided that the helium can be preferentially removed from the plasma ($\tau_{He} < \tau_{D,T}$) without increasing the energy transport.

The values of the confinement parameters $n_e\tau_{He}$, from the exhaust criterion, and $n_e\tau_E$ from the burn criterion are plotted in Fig. 3.2 for $f = 0.1$ as a function of plasma temperature. $n_e\tau_{He}$ has been divided by a factor of 3 in order to display the operational range for which the requirements $\tau_{He} = 3\tau_E$ and $f \leq 0.1$ [SIP89], [BEC88] can be fulfilled. The ratio of 3 is chosen to represent a realistic value based on the recent helium exhaust experiments described earlier. The quantities $n_e\tau_E$ and $n_e\tau_{He}/3$ are also presented in the case of an additional amount of 0.05 % Mo. The values of $n_e\tau_E$ for a clean plasma, i.e. $f = 0$, and the best confinement parameter obtained so far in JET [KEI90] are shown for reference.

For the relation $n_e\tau_{He} = 3n_e\tau_E$ and for a helium concentration of $f = 0.1$, there are only two points (◯) where both the burn criterion and the exhaust criterion are simultaneously fulfilled, and therefore represent possible steady-state operation. For other helium concentrations the curves for the burn criterion and the exhaust criterion also generally intersect at two points. The simultaneous solution of both the exhaust and the burn criterion, for various f values, is represented by a line (solid line in Fig. 3.2) which connects these points for helium concentrations between $f = 0.025$ (representing the lowest helium concentration) and $f = 0.2$.

For a burning fusion plasma with a given ratio $\tau_{He}/\tau_E = 3$ and no impurities, the confinement parameters must lie on this curve, otherwise steady state burn of the plasma is not possible. If we keep $f \leq 0.1$ but allow a different ratio of the particle confinement time to the energy confinement time, this curve is accordingly different.

The values of $n_e\tau_E$ and $n_e\tau_{He}$ show similar dependencies on the plasma temperature, as shown by eqs. (3.5) and (3.15). The exhaust condition (dotted line in Fig. 3.2) gives an upper limit for $n_e\tau_{He}$ that is consistent with $f \leq 0.1$. This relates from the fact that the helium confinement must be lower than specified by the condition, otherwise helium will accumulate in the plasma. On the other hand, the burn criterion gives the required values for the energy confinement parameter. If the energy confinement is less, the plasma will not burn.

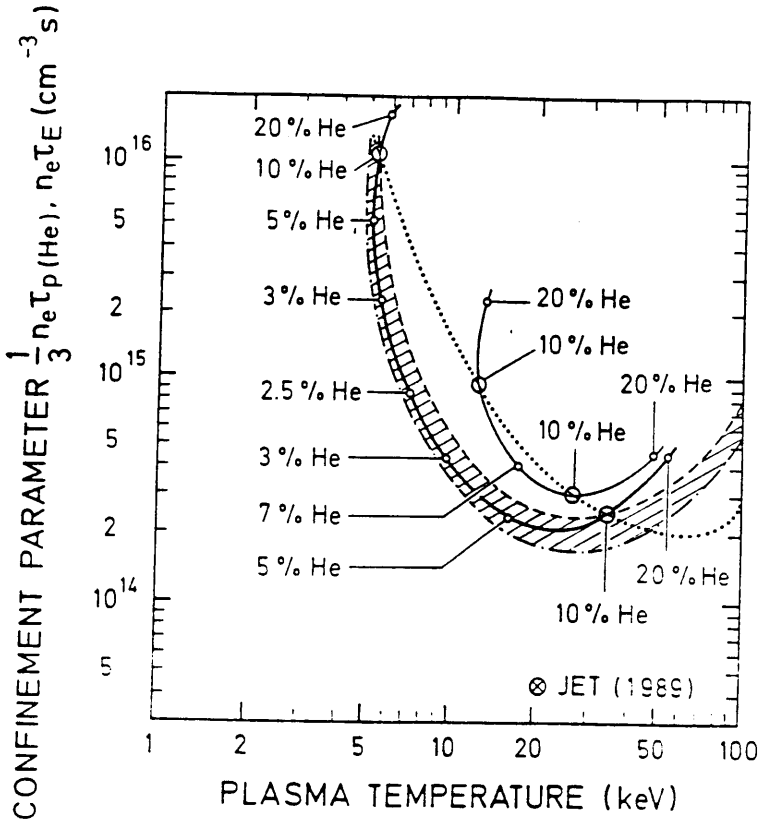

Figure 3.2: **Confinement parameters $n_e\tau_{He}/3$ and $n_e\tau_E$ as obtained from the exhaust criterion for a helium concentration of $f = 0.1$ (dotted line), and from the burn criterion for $f = 0.1$ and $f = 0$ (dashed and dash-dotted lines respectively). The thick solid line gives the values of the necessary confinement conditions for a burning plasma with $\xi = 3$ and for different helium concentrations with no other impurities present. The thin solid line gives the necessary confinement conditions for an impurity concentration of 0.05 % Mo. For different values of $\xi \leq 3$, $f \leq 0.1$, and no impurities, the energy confinement parameters must lie in the hatched area between the dashed line and the dash-dotted line. The best value obtained for JET for the energy confinement parameter is also shown.**

Both Fig. 3.1 and Fig. 3.2 show that, for a helium concentration of $f = 0.1$, it is only for plasma temperatures between about 5.5 keV and 35 keV (cyclotron radiation losses make this limit somewhat more stringent) that the required values of $n_e\tau_E$ from the burn criterion lie below the maximum values of $n_e\tau_{He}/3$ from the exhaust criterion if there are no further impurities in the plasma.

The intersection points, where the required parameters for both the energy confinement and the particle confinement are given, must lie in the hatched area between the curves for the ignition criterion at $f \leq 0.1$ and $f_i = 0$ in Fig. 3.2. For different helium concentrations the values will lie above or below the solid line representing the ratio $\tau_{He}/\tau_E = 3$, depending on whether this ratio is larger or smaller than 3. This area represents the operation parameters for a burning fusion plasma with $f \leq 0.1$ and no other impurities. If other impurities are present, the operational area is shifted to higher temperatures and larger values of the confinement parameters. The corresponding operational curve for 0.05 % Mo is also shown in Fig. 3.2 for values of $f = 0.07$ (minimum concentration) to $f = 0.2$. For larger impurity concentrations, plasma burn can only be achieved with helium concentrations larger than 0.1, which has serious implications for the fusion power density in a reactor.

Although not of much practical importance due to the density and β limits [UCK88, RED89], these lines of steady-state operation for different helium concentrations were calculated for the whole operational window, and were found to be closed curves, in agreement with the results of Reiter and Wolff [REI90] and Taylor *et al.* [TAY90]. These closed curves are shown in Fig. 3.3 for the cases of no impurities (solid line), 5 % carbon (·····) and 0.05 % molybdenum (- - -). For no impurities the theoretical allowable helium concentration varies from 3 - 140 %. These values change for the addition of the impurities. The exhaust criterion, eq. (3.5), is shown in bold together with these curves and the burn criterion (- - - and not closed) for the cases of no impurities and for no helium, and 10 % helium.

3.2.2 Discussion

This analysis, which appeared simultaneously with the results of Reiter *et al.* [REI90] and Taylor *et al.* [TAY90] obtained independently, is the first phenomenological analysis to link the process of helium and energy creation in a burning plasma in such a simple mathematical form.

The relations describing helium particle exhaust and burn of a D,T fusion plasma show that for the case of no impurities and a helium concentration of $f \leq 0.1$ there is only a limited range of values of the confinement parameters τ_{He} and τ_E as well as plasma temperatures for which a continuously burning thermonuclear D,T plasma can exist. If impurities build up in the plasma, the range where the plasma

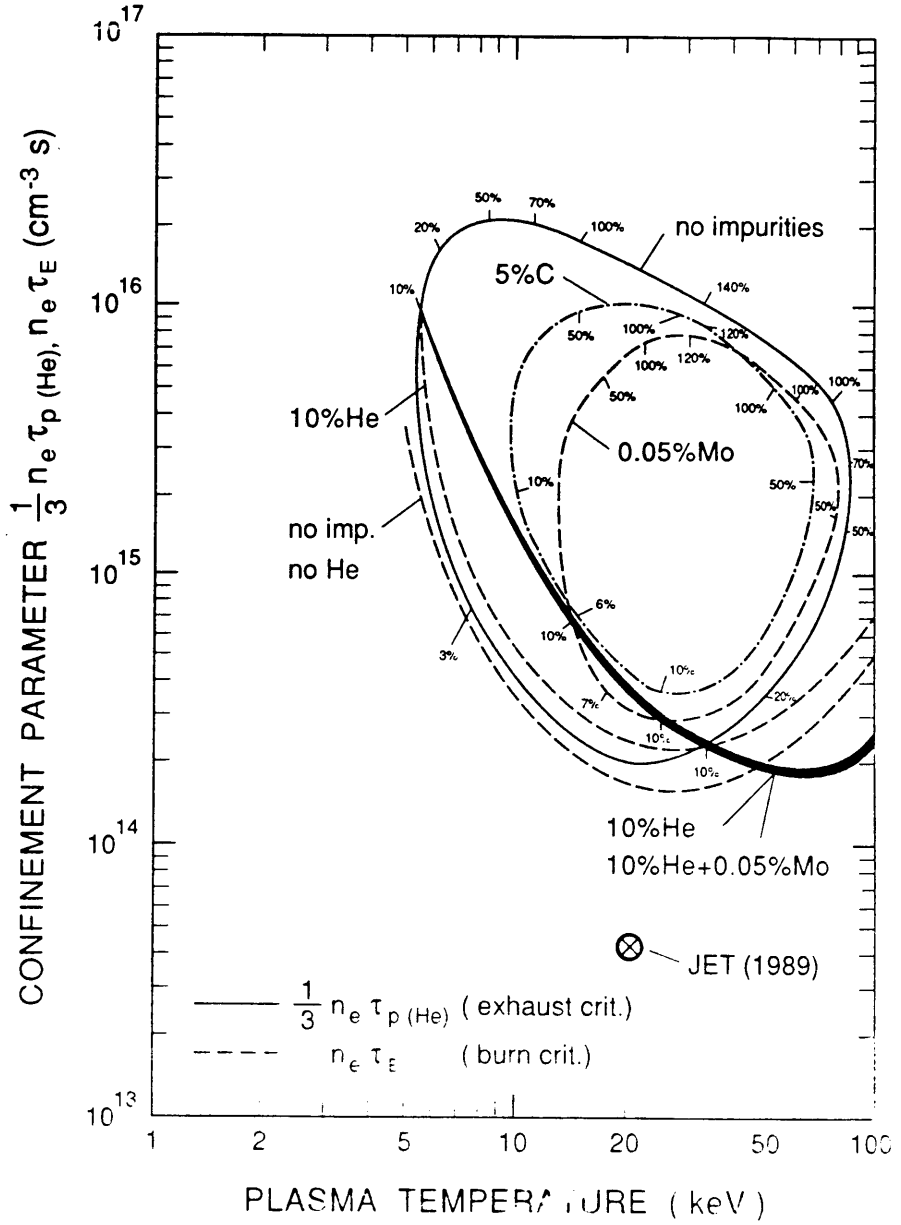

Figure 3.3: **Global closed lines of operation for no impurities (thin solid line), 5 % carbon (dashed-dotted line) and 0.05 % molybdenum (dashed line). The helium concentrations corresponding to various sections of the curves are also indicated. The helium exhaust criterion and burn criterion are also indicated by the open lines, the thick solid line with $f = 0.1$ plus impurities, and the dashed lines respectively.**

is ignited and the helium can be exhausted is shifted to higher temperatures and becomes narrower.

In the zero-dimensional algebraic estimates presented here, only averaged quantities and confinement times are considered, and particle density and temperature profiles or spatial variations of the diffusion coefficients are disregarded. Detailed calculations, taking into account the profiles as well as the locations of the sources and sinks for particles and energy, modify the criteria and show the operational space for a thermonuclear D,T plasma is fractionally different from that obtained with the present estimates. These calculations are presented in section 3.3, and a 1-dimensional approach in section 3.6. However, the general conclusions presented here remain valid and should also apply for an arbitrary confinement geometry.

These conclusions emphasize the necessity of finding effective means to keep the impurities in a D,T plasma at extremely low levels, as well as the need to control the confinement parameters $n_e\tau_{He}$ and $n_e\tau_E$; this may imply the requirement of finding means to preferentially remove helium without degrading the energy confinement [MIL89,CHA91A].

3.3 Re-evaluation of tolerable impurity concentrations in a D,T fusion plasma based on energy and helium particle exhaust

3.3.1 Introduction

The critical role of impurities in a fusion plasma has been known for a long time and will probably be one of the main problem areas in the successful operation of a D,T reactor [ENG80,VOJ90]. In a fusion reactor the energy produced by fusion reactions (i.e. the α energy) deposited in the plasma, as well as the ash have to be extracted from the vessel, and it is therefore impossible to isolate the plasma from the surrounding material walls. On the other hand the plasma bombardment of the vessel walls causes the release of wall atoms which may enter the plasma as impurities. It is therefore very important to know what concentrations of impurities can be tolerated in a burning fusion plasma.

The impurity ions in such a plasma have several disturbing effects. They cause additional energy losses from the plasma through radiation (i.e. bremsstrahlung, recombination and line radiation). Secondly their electrons contribute to the plasma pressure and electron density, i.e. for a given plasma pressure or electron density the presence of impurity ions causes a dilution of the fuel ions, which effects the

fusion rate negatively.

Based on these criteria, and using different approaches [MEA74,JEN77,VER78, CEC80] the influence of impurities in a fusion plasma has been studied in detail before and maximum allowable impurity concentrations were established for the different impurity elements.

The critical impurity concentrations calculated from the burn criterion [JEN77, VER78] (sometimes also called the ignition criterion [MEA74]) are based on the energy confinement time τ_E, demanding that the α fusion energy must be confined in the plasma long enough to replace convective and diffusive heat losses in order to maintain the plasma temperature. The critical impurity concentrations are then calculated as a function of temperature or atomic number for a single impurity, using a power balance between radiative and convective losses, and the α fusion power production. This has been the standard way [VER78] to determine the critical concentrations of single impurities to first order, but the method leads to impurity concentrations which cause the burn criterion to be infinitely large (compare eq. (3.15)), which is naturally not a physical result for a reactor environment.

An analysis based on this principle, where the total radiation of impurities was described by an "average ion model", was used by Jensen and Post [JEN77] to calculate the effect of impurity concentrations on the confinement criterion $n_e\tau_E$, from which critical concentrations were derived.

A similar analysis was made by Vernickel and Bohdansky [VER78], using a simple approximation to the total radiation of impurities, described by eqs. (3.13) and (3.14). The impurity concentrations were found from the steady-state power balance.

Another approach was used by Cecchi [CEC80] where the effect of an impurity on the fusion power gain Q (dilution of the fuel) and on the ratio (β) between the plasma pressure and magnetic pressure was considered, with the two quantities defined by

$$Q = \frac{(n_e - \sum_i n_i Z_i)^2}{4} \langle \sigma v \rangle_{DT} E_\alpha \tag{3.20}$$

and

$$\beta = \frac{n_{tot} kT}{\frac{B^2}{2\mu_0}} \tag{3.21}$$

with

$$n_{tot} = n_e + n_{DT} + \sum_i n_i$$

the total particle density in the plasma, B the magnetic field and μ_0 the magnetic permeability in vacuum. For a constant plasma temperature changes of 10 % in Q and $\sim$ 5 % in β were arbitrarily assumed to determine the critical concentration of an impurity. A 10 % reduction in Q roughly corresponds to a 5 % fractional decrease in β [CEC80]. An impurity concentration of element i leading typically to a fractional reduction of 5 % in β was found to be described by the expression

$$\frac{n_i}{n_e} < \frac{10}{Z_i^3} \tag{3.22}$$

For a 10 % reduction in Q due to fuel dilution, the critical impurity concentration was described by the relation

$$\frac{n_i}{n_e} < \frac{0.05}{Z_i} \tag{3.23}$$

These expressions show that the dilution of the fuel plays the most important role for impurity elements of low Z (< 14) - eq. (3.23) - and the effect on β becomes dominant for larger Z - eq. (3.22). In this case the effect on β is dominated by the decrease in plasma temperature due to radiative cooling, therefore showing the strong dependence on Z.

During the last few years the power balance and helium exhaust in a D,T fusion reactor have received special attention [UCK88,RED89,BEH90A,REI90]. A study by Uckan *et al.* [UCK88] using a one and a half dimensional analytical analysis describing the influence of the helium ash on β, studies by Redi *et al.* [RED89, RED90,RED91] using a one dimensional computer simulation (Baldur code) on the effect of helium accumulation on burn, as well as recent [BEH90A,REI90,TAY90] zero-dimensional analyses on burn and ash exhaust, agree on the principle that only a small operating window exists for a D,T fusion reactor. The existence and size of the window depend on the relation between the helium particle confinement time τ_{He} and the energy confinement time τ_E, and the tolerable helium and impurity concentrations in the plasma.

The zero-dimensional analyses are based on the principle that simultaneously with the burn criterion the need must be fulfilled to exhaust the helium fast enough in order not to suffocate the plasma. The last requirement is introduced via the exhaust criterion which is based on the helium particle confinement time τ_{He} as discussed in section 3.2. These analyses allow also the determination of the critical concentrations of a single impurity compatible with both the burn and exhaust criteria.

In this thesis critical impurity concentrations have been recalculated based on the

relations derived in section 3.2, where the effects of the impurities include dilution of the fuel ions, radiation losses and the exhaust of helium from the plasma. This approach yields impurity concentrations representing the highest concentration of an impurity where operation of a fusion reactor is still possible.

The impurity concentrations so obtained are dependent on the ratio (ξ) between the helium particle confinement time τ_{He} and the energy confinement time τ_E, and the helium concentration (f) allowed in the plasma, i.e. suitable values for ξ and f determine the impurity concentration where both burn - and exhaust criteria are fulfilled, as a function of plasma temperature. Alternatively the critical concentrations can be calculated for a specific temperature as a function of helium concentration.

3.3.2 Basic considerations

The model as put forward in section 3.2 is used, but with the more general definition of impurity concentration of Reiter *et al.* [REI90], where the concentration f_i of element i is defined as

$$f_i = \frac{n_i}{n_e} \tag{3.24}$$

Specification of f_i thus defines plasma dilution by both impurities and helium, which turns out to be one of the most critical parameters in sustained burning of a reactor [REI90] where low Z impurities are the dominant impurities in the plasma, and this definition was also used in the analyses [MEA74,JEN77,VER78,CEC80] to obtain critical impurity concentrations. The helium concentration f is defined in the same way as in eq. (3.24).

With this definition, the exhaust condition eq. (3.5) becomes

$$n_e\tau_{He} = \frac{4f}{(1-2f-\sum f_i Z_i)^2\langle\sigma v\rangle_{DT}} \tag{3.25}$$

and the burn condition eq. (3.15):

$$n_e\tau_E = \frac{\frac{3}{2}kT(2-f-\sum f_i(Z_i-1))}{\frac{(1-2f-\sum f_i Z_i)^2}{4}\langle\sigma v\rangle_{DT}E_\alpha - (B+R)} \tag{3.26}$$

with B and R given by (3.11) and (3.14) respectively, being the bremsstrahlung [MEA74] contribution from elements with $Z_i \leq 6$, and total radiation [VER78]

contribution as derived from eq. (3.13) for elements with larger Z_i, with synchrotron and other radiation neglected.

Eq. (3.25) divided by eq. (3.26) yields the equivalent of eq. (3.18):

$$\xi = \frac{\tau_{He}}{\tau_E} = \frac{fE_\alpha - \frac{4f(B+R)}{\langle\sigma v\rangle_{DT}(1-2f-\sum f_i Z_i)^2}}{\frac{3}{2}kT(2-f-\sum f_i(Z_i-1)} \tag{3.27}$$

from which the impurity concentration f_i of one single impurity element with atomic number Z_i can be found depending on ξ, kT and the helium concentration f.

The result is the cubic equation in f_i:

$$\begin{aligned}
& [\frac{3}{2}\xi kT\langle\sigma v\rangle_{DT}(1-Z_i)Z_i^2]\cdot f_i^3 \\
+\ & [\frac{3}{2}\xi kT\langle\sigma v\rangle_{DT}(2-f)Z_i^2 - 3\xi kT\langle\sigma v\rangle_{DT}(1-2f)(1-Z_i)Z_i \\
-\ & fE_\alpha\langle\sigma v\rangle_{DT}Z_i^2]\cdot f_i^2 \\
+\ & [\frac{3}{2}\xi kT\langle\sigma v\rangle_{DT}(1-2f)^2(1-Z_i) - 3\xi kT\langle\sigma v\rangle_{DT}(1-2f)(2-f)Z_i + 4fR_1 \\
+\ & 2(1-2f)Z_i fE_\alpha\langle\sigma v\rangle_{DT}]\cdot f_i \\
+\ & [\frac{3}{2}\xi kT\langle\sigma v\rangle_{DT}(2-f)(1-2f)^2 + 4fB - fE_\alpha\langle\sigma v\rangle_{DT}(1-2f)^2] \\
=\ & 0
\end{aligned} \tag{3.28}$$

with $R_1 = R/f_i$.

3.3.3 Results and discussion

For the case of $\xi = 3$, eq. (3.28) has in general one useful real solution in the temperature area of interest and for values of f tolerable in the plasma. This solution is shown in Fig. 3.4 as a function of temperature, for a helium concentration of 10%, which is projected for ITER [COH90], and for the elements carbon, beryllium, iron, molybdenum and tungsten. The polynomial fit to $\langle\sigma v\rangle_{DT}$ by Miley *et al.* [MIL74], namely

$$\begin{aligned}
\ln\langle\sigma v\rangle_{DT} &= \frac{-21.377692}{(kT)^{0.2935}} - 25.204054 \\
&- 7.1013427\cdot 10^{-2}kT + 1.9375451\cdot 10^{-4}(kT)^2 \\
&+ 4.9246592\cdot 10^{-6}(kT)^3 - 3.9836572\cdot 10^{-8}(kT)^4
\end{aligned} \tag{3.29}$$

was used in the calculations with kT in keV. This results in maximum concentrations for these elements of 10%, 6%, 0.3%, 0.1% and 0.023% at about 23 keV respectively. At lower and higher temperatures the critical concentrations decrease quickly, presenting a window in the temperature domain. Also shown are the critical impurity concentrations from previous analyses [JEN77,VER78] for the same elements, as derived from the the burn criterion alone where the power lost by radiation from the plasma equals the α fusion power.

For the case of $\xi = 3$, eq. (3.28) yields impurity concentrations which are less than impurity concentrations calculated in the normal way for the whole range of plasma temperatures. The values become smaller rapidly for larger values of ξ.

Also shown in Fig. 3.4 are the maximum allowable impurity concentrations as determined by Cecchi [CEC80] based on the lowering of Q and β. The critical impurity concentrations based on these principles are more stringent for the elements included than those obtained from eq. (3.28), but it must be kept in mind that the limits placed on these effects in Q and β were somewhat arbitrarily selected.

For 10 % helium together with a large value of $\xi \approx 7$ (see Fig. 3.5) the largest concentration tolerable for beryllium is about 5 % at 12 keV and decreases dramatically for both higher and lower temperatures such as to converge to zero at about 5 keV and 20 keV. The heavier elements are restricted to much lower critical concentrations in a slightly smaller operational range of temperatures. For carbon, iron, molybdenum and tungsten the highest concentrations tolerable under the conditions mentioned are about 2%, 0.05%, 0.01% and 0.002% respectively. The low value of 2 % for carbon shows the importance of keeping the impurity content very low in order to sustain burn for large values of ξ. This in turn has special requirements for divertor and limiter design and accurate control of the edge plasma conditions.

The impurity concentrations were also calculated from eq. (3.28) as a function of f, for two fixed temperatures of 10 keV and 20 keV. The results are shown in Fig. 3.6 where concentrations of the same elements as before are plotted for $\xi = 3$ and $f \leq 0.2$. The solid lines refer to a plasma temperature of 10 keV and the dashed lines to 20 keV. The results show clearly that for these two plasma temperatures different optimum values of f exist, placing different limitations on the impurity content in the plasma. As expected, the higher fusion rate at the higher temperature leads to higher energy production, which is reflected in the higher tolerable impurity concentration.

The general shape of the curves in Fig. 3.6, with the decrease in allowed impurity concentrations both at lower and at higher f, is due to the standoff between the fact that for lower f the operational range of the burn and exhaust criterion becomes smaller, but for larger f the dilution and poisoning due to helium becomes the dominant factor. For a plasma temperature of 20 keV a helium concentration of

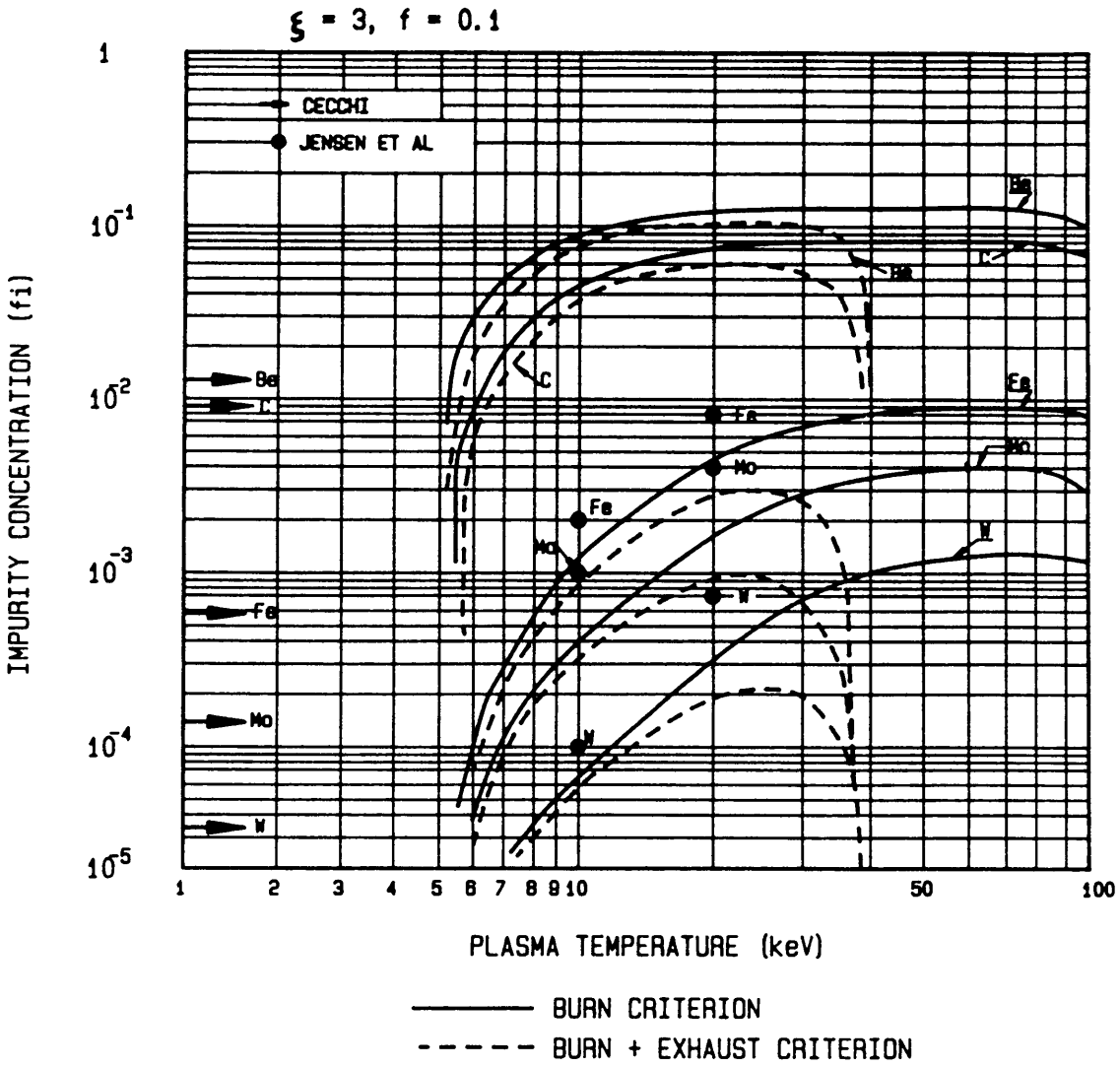

Figure 3.4: Tolerable impurity concentrations, f_i, for different elements in the plasma, calculated from the burn and exhaust criterion (dashed curves) with $f = 0.1$ and $\xi = 3$, compared to critical concentrations calculated with only the burn criterion (dots and solid curves). Also shown are values obtained from [CEC80] (arrows)

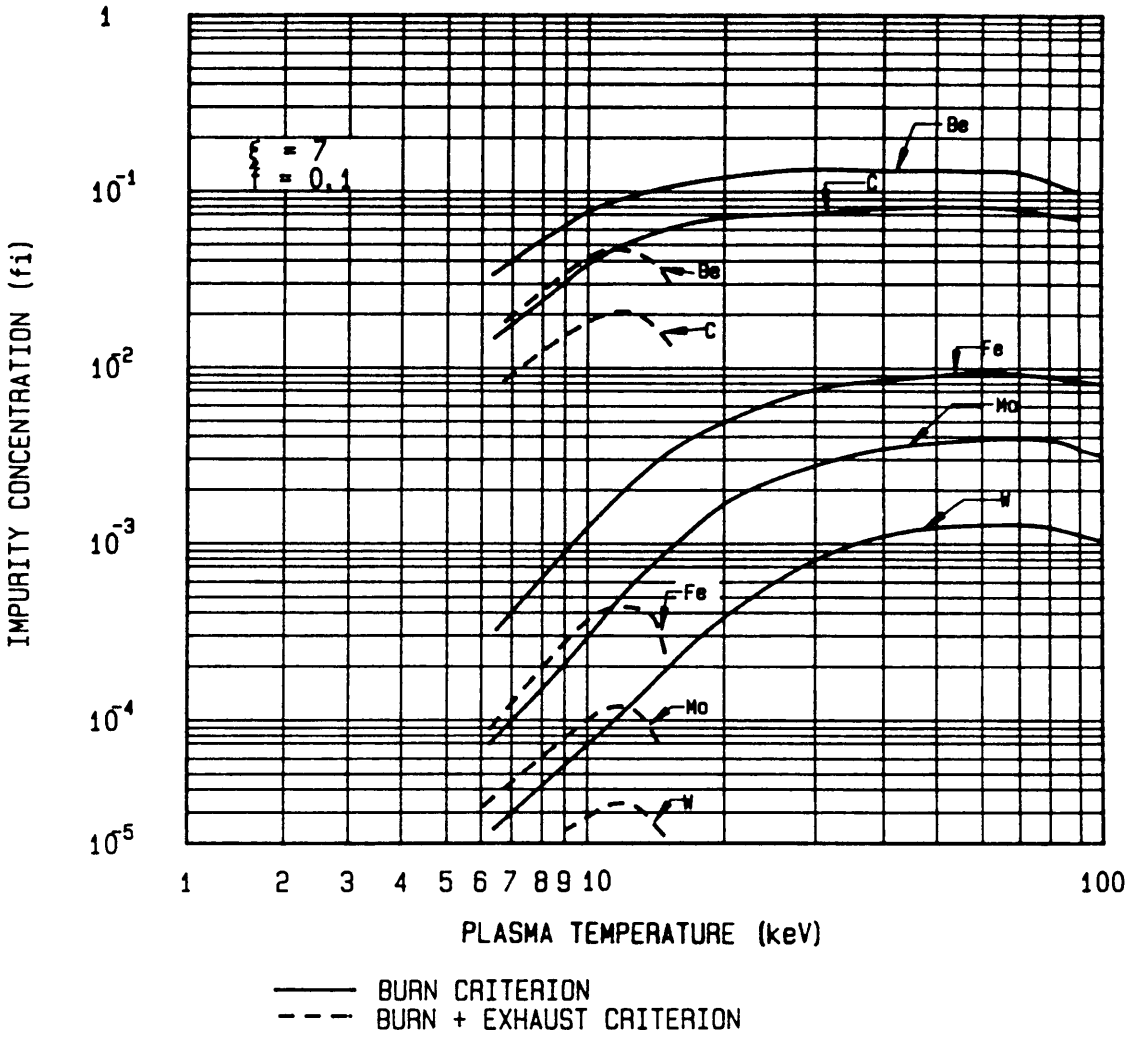

Figure 3.5: **Tolerable impurity concentrations f_i for different elements in the plasma, calculated from the burn and exhaust criterion (dashed curves) with $f = 0.1$ and $\xi = 7$, compared to critical concentrations calculated with only the burn criterion (dots and solid curves).**

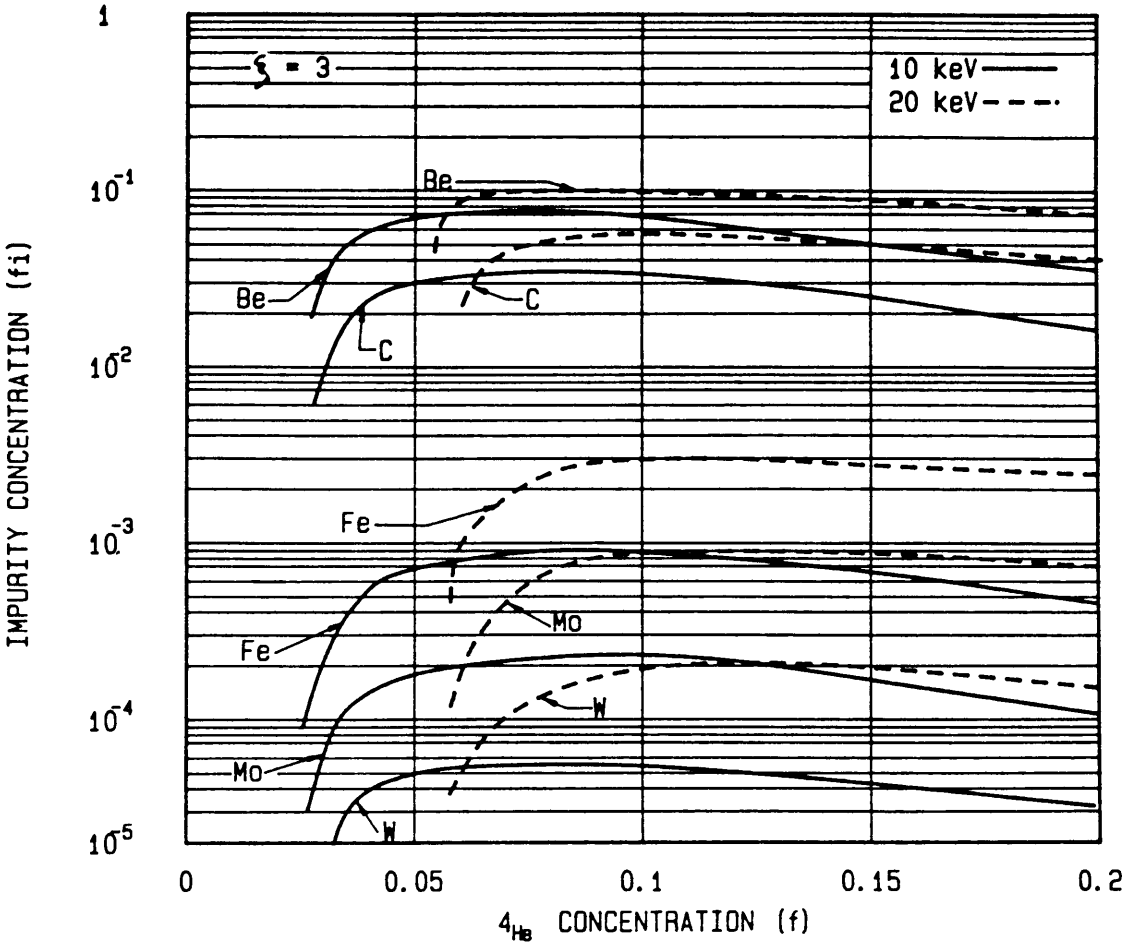

Figure 3.6: **Impurity concentrations f_i in the plasma calculated from the burn and exhaust criterion as a function of the helium concentration (f) for plasma temperatures of 10 keV (solid curves) and 20 keV (dashed curves)**

about 10 % must be tolerated, as the allowed f_i decreases sharply below this value. At 10 keV there is little difference between values of 5 % and 10 % for f, which allows more versatility in operation at this temperature. Significantly higher impurity concentrations are in general allowed in the plasma at the higher temperature of 20 keV, when compared to 10 keV.

Bearing in mind that the indicated impurity concentrations are indeed maximum allowable concentrations for reactor operation, it is realistic to express critical concentrations in this way. One must keep in mind though, that ξ is not reliably known at this stage [BEC88,HIL91].

3.4 Profile effects included in the burn - and exhaust criterion

3.4.1 Introduction

An argument against the zero-dimensional analysis described up to now, is the validity of such an analysis when applied to tokamak geometry, considering the complexities of the fusion process in tokamaks. In particular the plasma parameters like density and temperature are not constant throughout the plasma volume in a tokamak, and this fact is being ignored by the zero-dimensional model.

Typical profiles of density and temperature as a function of the small radius of a tokamak are given in Fig. 3.7. Even though the shape of the profile of the plasma temperature is undesirable with respect to the fusion yield, i.e. the lower temperature towards the edge of the plasma lowers the mean temperatures and the fusion power, it is necessary to minimize the influx of sputtered impurities from materials at the plasma edge. If the temperature is high in the edge of the plasma the energies of the ions leaving the plasma will also be high, and the thermal load on the limiters, divertor plates and walls will be excessive. It is therefore desirable to keep the edge temperature [VOJ90] of a tokamak reactor with a low Z first component material below $\sim$ 150 eV and with a high Z plasma-facing material below $\sim$ 50 eV.

These temperatures represent typical impact energies where the sputtering yields of materials hit by the ions become excessive, and too high a concentration of impurities is permitted into the plasma volume, which influences the fusion process in the plasma through fuel dilution and radiation losses. These temperatures also reflect the fact that a higher concentration of low Z impurities can be tolerated compared to high Z materials due to the lower radiation losses incurred through low Z materials. It is projected that a fusion reactor will have to be operated in a high recycling

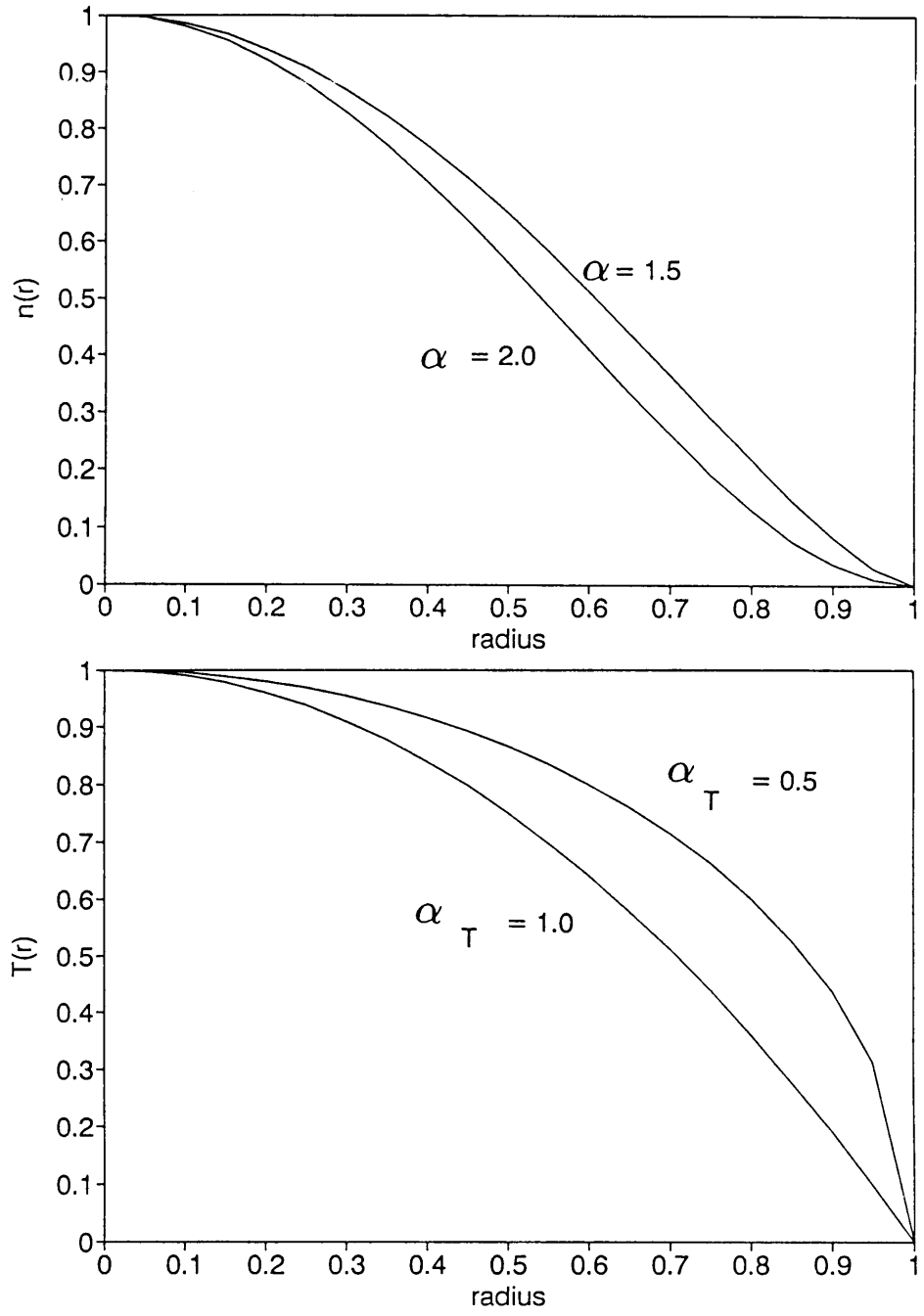

Figure 3.7: **Typical profiles of the form $(1-\frac{r^2}{a^2})^\alpha$ of density and temperature as a function of the small radius of a tokamak. Different values of alpha are indicated**

scenario, with a low edge temperature and high edge density (it is experimentally found today [COH90] that these two quantities behave such that the edge plasma pressure stays approximately constant). In this way the bombardment energies of the ions on the divertor plates are decreased, and the ionisation of impurities moving towards the plasma in the scrape-off layer is enhanced, leading to a reduction of impurities that reach the plasma core.

To establish typical values for the impurity confinement time needed to keep the impurity concentration below critical values, the following global estimate can be made. The flux of ions onto the limiter during a typical discharge in JET is of the order of 10^{22}/s. With a sputtering yield of 0.08 atoms/ion (the sputtering yield for D^+ on Be with an energy of 80 eV [GAU90]) at the limiter, the impurities released would be $8 \cdot 10^{20}$ ions/s, and if a screening factor of 0.3 (the fraction of this flux that reaches the plasma volume) is assumed [MCC90], and a plasma volume of 200 m^3 (JET), the average impurity density in the plasma would increase by $\approx 3 \cdot 10^{18}$ atoms/m^{-3}s. For stationary conditions this increase must be countered by the loss of impurities from the plasma, through the finite confinement time of the impurities. In this case, the outflux (n_i/τ_i) equals the influx. If the impurity concentration f_i must be kept below 6 % (the maximum for carbon in the physics guidelines of ITER [UCK88A]) of the electron density, $n_e = 2 \cdot 10^{20}$ m^{-3}, the impurity confinement time τ_i must be smaller than ~ 4 s.

Profile effects, however, must also affect the zero-dimensional model presented earlier, and the model that follows was an endeavour to establish such influence on and changes to the results of the zero-dimensional model. Profiles of different forms were included in the zero-dimensional model by Reiter *et al.* [REI90A] in an *ad hoc* way and they found the influence on the results of the zero-dimensional model small. In what follows an attempt is made to study the influence of one type of profile more extensively.

3.4.2 Model considerations

For the introduction of profile effects, we have to study volume-averaged quantities of the plasma density and temperature. For this reason we define quantities with respect to the volume of the plasma. We consider a circular tokamak with small radius a and big radius R, the geometry of which is shown in Fig. 3.8. In this case the volume is:

$$V = 2\pi R \cdot \pi a^2 \tag{3.30}$$

For any small radial distance r the volume enclosed is:

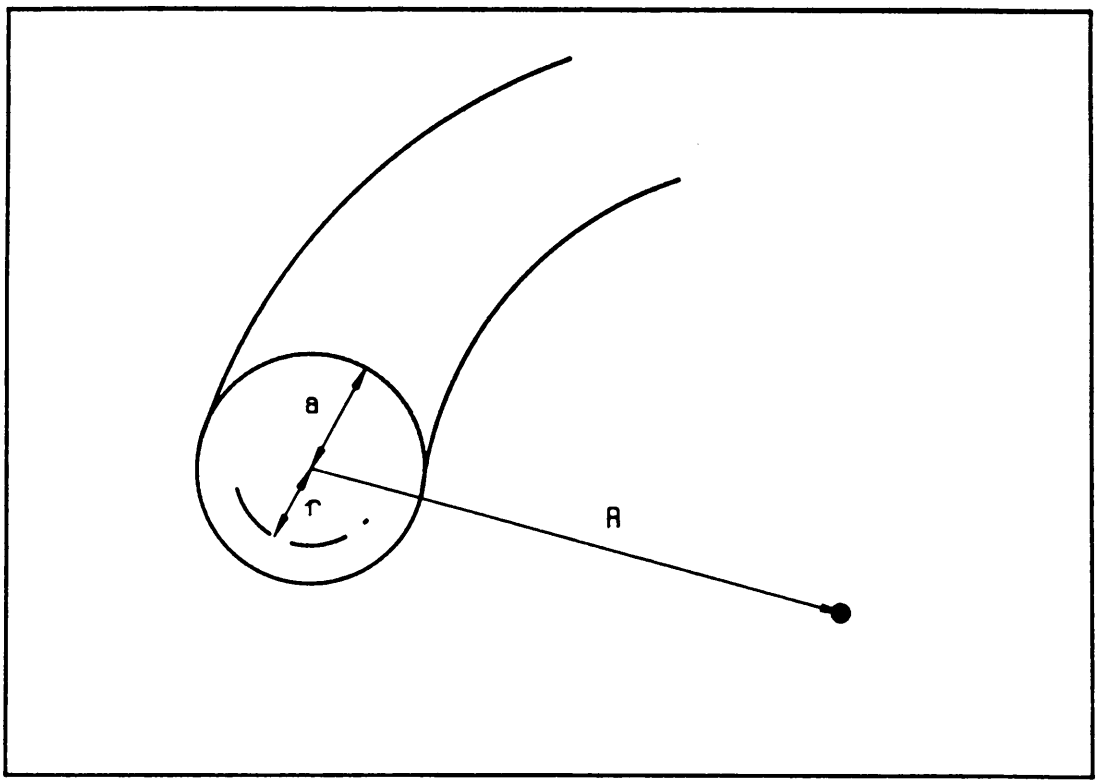

Figure 3.8: **Circular tokamak geometry with small radius a and big radius R**

$$V(r) = 2\pi^2 R r^2 \tag{3.31}$$

and so:

$$dV = 4\pi^2 R r dr \tag{3.32}$$

The form of the profiles assumed is:

$$n(r) = n(0)(1 - \frac{r^2}{a^2})^{(\alpha_n)} \tag{3.33}$$

$$kT(r) = kT(0)(1 - \frac{r^2}{a^2})^{(\alpha_T)} \tag{3.34}$$

where $n(r)$ and $kT(r)$ are defined as particle densities and temperatures respectively with $n(0)$ and $kT(0)$ the central values. Edge values of $n(r)$ and $kT(r)$ were neglected for this study, i.e. it was assumed that the limiters are to a large extent infinite sinks for heat and particles.

The burn criterion

The average α power density deposited is now described by the following equation (3.7):

$$\bar{P}_\alpha = \frac{1}{V} \int_V n_D(r) n_T(r) \langle \sigma v \rangle_{DT} E_\alpha dV \tag{3.35}$$

where $\langle \sigma v \rangle_{DT}$ is a function of the temperature. Using (3.32):

$$\bar{P}_\alpha = \frac{4\pi^2 R E_\alpha}{V} \int_0^a n_D(r) n_T(r) \langle \sigma v \rangle_{DT} r dr \tag{3.36}$$

and with the transformation $x = \frac{r}{a}$ the α power becomes:

$$\bar{P}_\alpha = \frac{4a^2\pi^2 R E_\alpha}{V} \int_0^1 n_D(x) n_T(x) \langle \sigma v \rangle_{DT} x dx \tag{3.37}$$

Next we use the density and temperature profiles (3.34) to find:

$$\bar{P}_\alpha = \frac{4a^2\pi^2 R E_\alpha n_D(0) n_T(0)}{V} \int_0^1 (1-x^2)^{\alpha_D + \alpha_{Tr}} \langle \sigma v \rangle_{DT} x dx \tag{3.38}$$

where α_D and α_{Tr} are the density profile coefficients of deuterium and tritium respectively. With the assumption that $n_D(0) = n_T(0) = n_{DT}(0)/2$, and that $\alpha_D = \alpha_{Tr} = \alpha_{DT}$, therefore assuming that the confinement times of D and T are equal, $\bar{P}_\alpha$ becomes:

$$\bar{P}_\alpha = \frac{a^2\pi^2 R E_\alpha n_{DT}(0)}{V} \int_0^1 (1-x^2)^{2\alpha_{DT}} \langle \sigma v \rangle_{DT} x dx \tag{3.39}$$

The assumption that the confinement times of D and T are equal is valid due to the equal charge ($Z = 1$) of these ions. There is a so-called isotope effect which has been found experimentally, but is of minor importance. From quasi-neutrality of the plasma:

$$\int_V n_e(r) dV = \int_V [n_{D,T}(r) + 2n_{He}(r) + Z n_i(r)] dV \tag{3.40}$$

where $n_{He}(r)$ is the helium concentration in the plasma, $n_i(r)$ is the impurity concentration, and for the purpose of this model we assume that there is only one extra impurity element present in the plasma.

For reasons of simplicity it is now assumed that:

$$\alpha_e = \alpha_{DT} = \alpha_{He} = \alpha_i = \alpha \tag{3.41}$$

where α_e, α_{He} and α_i are the density profile coefficients for the electrons, helium and impurity constituents in the plasma. Again it is assumed implicitly that the diffusion coefficients of these species are approximately equal. This assumption tends to be a lower limit to the confinement time of higher Z (> 2) impurities, as the observation [FUS89] was that the higher Z elements are better confined in the plasma volume than the hydrogen species. The electrons, with a much lower mass, are much more mobile and the confinement time for electrons is normally found to be smaller than the confinement time for D, this assumption therefore placing an upper limit to the confinement time of the electrons.

The following definitions are made with respect to the fuel density:

$$n_{He}(0) = f n_{DT}(0) \tag{3.42}$$

$$n_i(0) = f_i n_{DT}(0) \tag{3.43}$$

assuming that the ratio of the helium concentration and the impurity concentration in the plasma is constant as a function of the small radius of the tokamak as implied by (3.41). The change of definition back to the reference with respect to the fuel density, as opposed to reference with respect to the electron density, see eq. (3.24), was made to directly compare the values for the zero-dimensional analysis with the results obtained in this section.

From (3.40), (3.42) and (3.43) it is found that:

$$\begin{aligned} n_e(0) &= n_{DT}(0) + 2f n_{DT}(0) + Z_i f_i n_{DT}(0) && (3.44) \\ &= n_{DT}(0)[1 + 2f + f_i Z_i] && (3.45) \end{aligned}$$

It is then easy to finally obtain for the α power in terms of $n_e(0)$, f and f_i:

$$\bar{P}_\alpha = \frac{a^2\pi^2 R E_\alpha}{V} \frac{n_e^2(0)}{(1 + 2f + f_i Z_i)^2} I \tag{3.46}$$

with

$$I = \int_0^1 (1 - x^2)^{2\alpha} \langle \sigma v \rangle_{DT} x dx \tag{3.47}$$

Radiated power

For the analysis of the total radiated power lost from the plasma, the following assumptions are made. Bremsstrahlung losses dominate for $Z \leq 6$ impurity elements, and the description of Meade [MEA74] is used. For $Z > 6$ the total radiation approximation description of Vernickel and Bohdansky [VER78] is used.

Bremsstrahlung ($Z \leq 6$)

The volume-averaged description of the total bremsstrahlung following Meade [MEA74] is as follows:

$$\bar{P}_{Brems} = \frac{1}{V} \int_V K n_e(r) \sum_i n_i(r) Z_i^2 \sqrt{kT(r)} dV \tag{3.48}$$

for the values of $\bar{P}_{Brems}$ in J/(s· m^3) $K = 3.842 \cdot 10^{-29}$, with $kT(r)$ in J and densities in m^{-3}. The sum over i is over all ion species in the plasma, which in this model

is limited to the fuel, helium and one extra impurity constituent. Using the same transformation as before we find

$$\bar{P}_{Brems} = \frac{4a^2\pi^2RK}{V}\int_0^1 n_e(x)[n_{DT}(x) + 4n_{He}(x) + \sum_i n_i(r)Z_i^2]\sqrt{kT(x)}xdx \quad (3.49)$$

With the additional requirement of quasi-neutrality (3.40) and one extra impurity element present in the plasma we find:

$$\bar{P}_{Brems} = \frac{4a^2\pi^2RK}{V}n_e^2(0)\sqrt{kT(0)}\frac{(1+4f+Z_i^2f_i)}{(1+2f+Z_if_i)}\int_0^1(1-x^2)^{2\alpha+\alpha_T/2}xdx \quad (3.50)$$

In general the integral

$$\int_0^1(1-x^2)^m xdx = \frac{1}{2(m+1)} \quad (3.51)$$

and with $m = 2\alpha + \alpha_T/2$ we finally find for $\bar{P}_{Brems}$ (i.e. $Z < 6$):

$$\bar{P}_{rad} = \bar{P}_{Brems} = \frac{2a^2\pi^2RK}{V}n_e^2(0)\sqrt{kT(0)}\frac{(1+4f+Z_i^2f_i)}{(1+2f+f_iZ_i)(m+1)} \quad (3.52)$$

Total radiation (Z > 6)

Following the description of [VER78] the average radiation density is given by:

$$\bar{P}_{rad} = \frac{K_2}{V}\int_V n_e(r)\sum_i n_i(r)(1+0.3kT(r))Z_i^{3.7-0.33ln(kT(r))}dV \quad (3.53)$$

with the values of $\bar{P}_{rad}$ in J/(s m^3) $K_2 = 1\cdot10^{-37}$, with $kT(r)$ in keV and densities in m^{-3}. With one extra impurity other than helium, and transformed in the same way as before, we find:

$$\bar{P}_{rad} = \frac{4a^2\pi^2RK_2}{V}\int_0^1 n_e(x)(1+0.3kT(x))f_in_{DT}Z_i^{3.7-0.33ln(kT(x))}xdx \quad (3.54)$$

and with eqs. (3.34) and (3.40), follows for $Z \geq 6$:

$$\bar{P}_{rad} = \frac{4a^2\pi^2}{V} R \frac{n_e^2(0) f_i K_2}{(1+2f+Z_i f_i)} \qquad \int_0^1 (1-x^2)^{2\alpha}(1+0.3kT(0)(1-x^2)^{\alpha_T}) Z_i^{3.7-0.33ln[kT(x)]} x dx \tag{3.55}$$

It must be emphasised that the two expressions for the total radiation and bremsstrahlung must be used separately to obtain the total radiation losses from the plasma. P_{rad} is used exclusively for $Z > 6$, and for $Z \leq 6$ we only consider bremsstrahlung (P_{Brems}). The bremsstrahlung due to the fuel and helium present must always be added to the contribution from the impurity in the plasma. In summary, it follows that:

$$\bar{P}_{totrad} = \bar{P}_{Brems} \qquad Z \leq 6 \tag{3.56}$$

$$= \bar{P}_{Brems0} + \bar{P}_{rad} \qquad Z > 6 \tag{3.57}$$

where for $Z > 6$, $\bar{P}_{Brems0}$ is the contribution of only the fuel and helium to the radiation losses through bremsstrahlung:

$$\bar{P}_{Brems0} = \frac{2a^2\pi^2 RK}{V} n_e^2(0)\sqrt{kT(0)} \frac{(1+4f)}{(1+2f)(m+1)} \tag{3.58}$$

The combined expression for the total radiation thus is:

$$\bar{P}_{totrad} = \frac{n_e^2(0)}{(1+2f+Z_i f_i)} \begin{cases} K\sqrt{kT(0)} \frac{(1+4f+Z_i^2 f_i)}{(1+2\alpha+\frac{\alpha_T}{2})} & \text{for } Z_i \leq 6 \\ K\sqrt{kT(0)} \frac{(1+4f)}{(1+2\alpha+\frac{\alpha_T}{2})} + 2f_i K_2 I_2 & \text{for } Z_i > 6 \end{cases} \tag{3.59}$$

$$= \frac{n_e^2(0)}{(1+2f+Z_i f_i)} R_0 \tag{3.60}$$

with

$$I_2 = \int_0^1 (1-x^2)^{2\alpha}(1+0.3kT(0)(1-x^2)^{\alpha_T}) Z_i^{3.7-0.33ln[(kT(0))+\alpha_T ln(1+x^2)]} x dx \tag{3.61}$$

Conductive and convective power

The average power density conducted and convected from the plasma is likewise given by the following equation:

$$\bar{P}_C = \frac{1}{V}\int_V \frac{\frac{3}{2}n_{tot}(r)kT(r)}{\tau_E}dV \tag{3.62}$$

with τ_E assumed to be a constant over r, and

$$\begin{aligned} n_{tot}(r) &= n_e(r) + n_{DT}(r) + n_{He}(r) + n_i(r) && (3.63)\\ &= n_e(0)[\frac{2+3f+(Z_i+1)f_i}{1+2f+Z_if_i}](1-\frac{r^2}{a^2})^\alpha && (3.64)\end{aligned}$$

Using the same transformation as before and (3.51), we find:

$$\bar{P}_C = \frac{3\pi^2a^2Rn_e(0)kT(0)}{V\tau_E}\frac{2+3f+(Z_i+1)f_i}{(1+2f+Z_if_i)(1+\alpha+\alpha_T)} \tag{3.65}$$

The burn criterion is given by the expression (3.7):

$$\bar{P}_\alpha - \bar{P}_{totrad} = \bar{P}_C \tag{3.66}$$

and with the reduction of (3.46), (3.52), (3.57) and (3.65), this leads to the result for the burn criterion volume-averaged over the small radius:

$$n_e(0)\tau_E = \frac{1}{(1+\alpha+\alpha_T)}\frac{6kT(0)[2+3f+(Z_i+1)f_i]}{\frac{2E_\alpha I}{(1+2f+Z_if_i)}-4R_0} \tag{3.67}$$

In the volume-averaged considerations of profiles, however, it is of practical use to express the criteria in terms of average values for the density and temperature. In this case the averaged values are:

$$\bar{n} = \frac{n(0)}{1+\alpha} \tag{3.68}$$

$$\bar{kT} = \frac{kT(0)(1+\alpha)}{1+\alpha+\alpha_T} \tag{3.69}$$

Finally the burn criterion may be presented by the expression:

$$\bar{n_e}\tau_E = \frac{1}{(1+\alpha)^2}\left\{\frac{3\bar{kT}[2+3f+(Z_i+1)f_i]}{\frac{E_\alpha I}{(1+2f+Z_if_i)}-2R_0}\right\} \tag{3.70}$$

3.4.3 The exhaust criterion

With the consideration of the radial profiles the particle balance equation (3.2) now becomes:

$$\frac{d\bar{n}_{He}}{dt} = \frac{1}{V}\int_V n_D(r)n_T(r)\langle\sigma v\rangle_{DT}dV - \frac{\bar{n}_{He}}{\tau_{He}} \tag{3.71}$$

where $\bar{n}_{He}$ denotes the volume-averaged helium concentration in the plasma. In steady state $\frac{d\bar{n}_{He}}{dt} = 0$, and the exhaust criterion becomes:

$$\frac{1}{V}\int_V n_D(r)n_T(r)\langle\sigma v\rangle_{DT}dV = \frac{\bar{n}_{He}}{\tau_{He}} \tag{3.72}$$

With eqs. (3.32), (3.33), (3.34), (3.40), (3.41) and (3.47), this reduces to

$$n_e(0)\tau_{He} = \frac{2f(1+2f+f_iZ_i)}{I(\alpha+1)} \tag{3.73}$$

and with the averaged quantities inserted into eq. (3.73)

$$\bar{n}_e\tau_{He} = \frac{2f(1+2f+f_iZ_i)}{I(\alpha+1)^2} \tag{3.74}$$

3.4.4 Results

In Fig. 3.9 a similar plot to Fig. 3.2 is shown for the operational space for a D,T fusion reactor operating in steady state for confinement parameters vs plasma temperature for $\frac{\tau_{He}}{\tau_E} = 3$. Here, however, only the burn criterion for no helium and no impurities, with 10 % helium included, with 10 % helium and 0.05 % molybdenum is shown, together with the exhaust criterion for the same parameters. Here it can be seen that profiles corrections are small, and that the difference between these results and the zero-dimensional model is negligible for the model used.

The relations (3.70) and (3.74) can now be combined for a fixed value of the ratio (ξ) of the helium particle confinement time and the energy confinement time.Division of (3.70) with (3.74) yields:

$$\frac{\tau_{He}}{\tau_E} = \frac{2f[E_\alpha - 2\frac{(1+2f+f_iZ_i)R_0}{I}]}{3\bar{kT}[2+3f+(Z_i+1)f_i]} = \xi \tag{3.75}$$

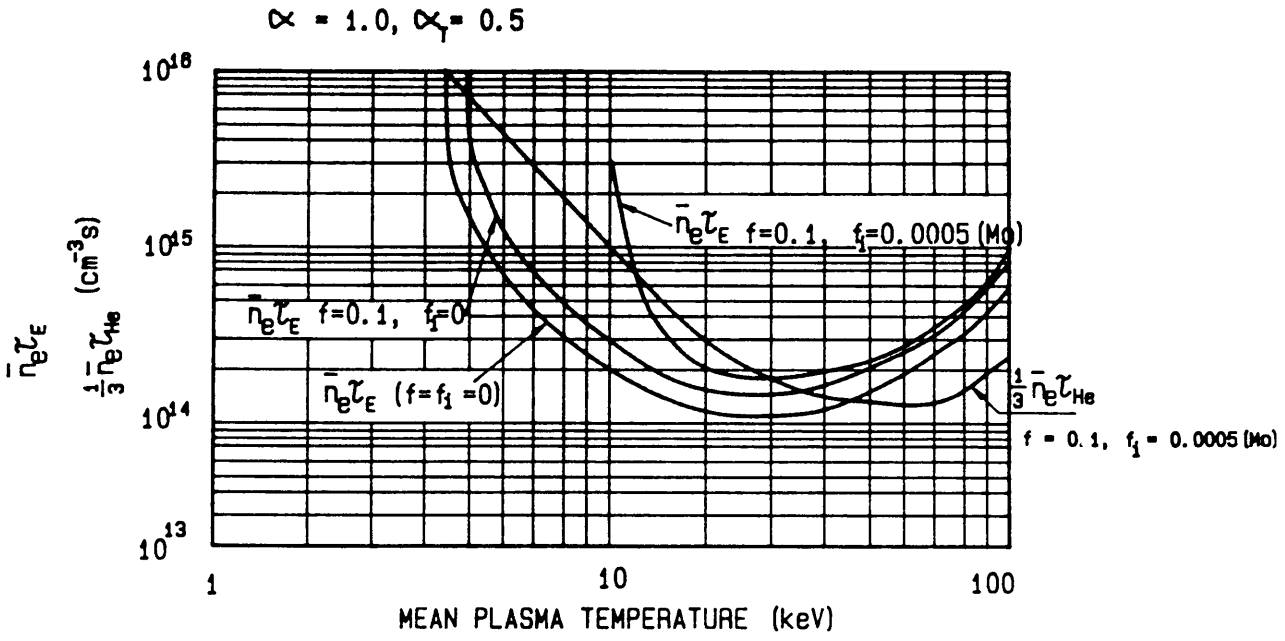

Figure 3.9: The operational space ($n_e\tau_E$ vs kT) for a D,T fusion reactor operating in steady state with $\frac{\tau_{He}}{\tau_E} = 3$. The burn criterion for no helium and no impurities ($f = f_i = 0$), with 10 % helium included ($f = 0.1$, $f_i = 0$), and with 10 % helium plus 0.05 % molybdenum ($f = 0.1$, $f_i = 0.005$) and the exhaust criterion for the same parameters ($f = 0.1$, $f_i = 0.005$) is shown.

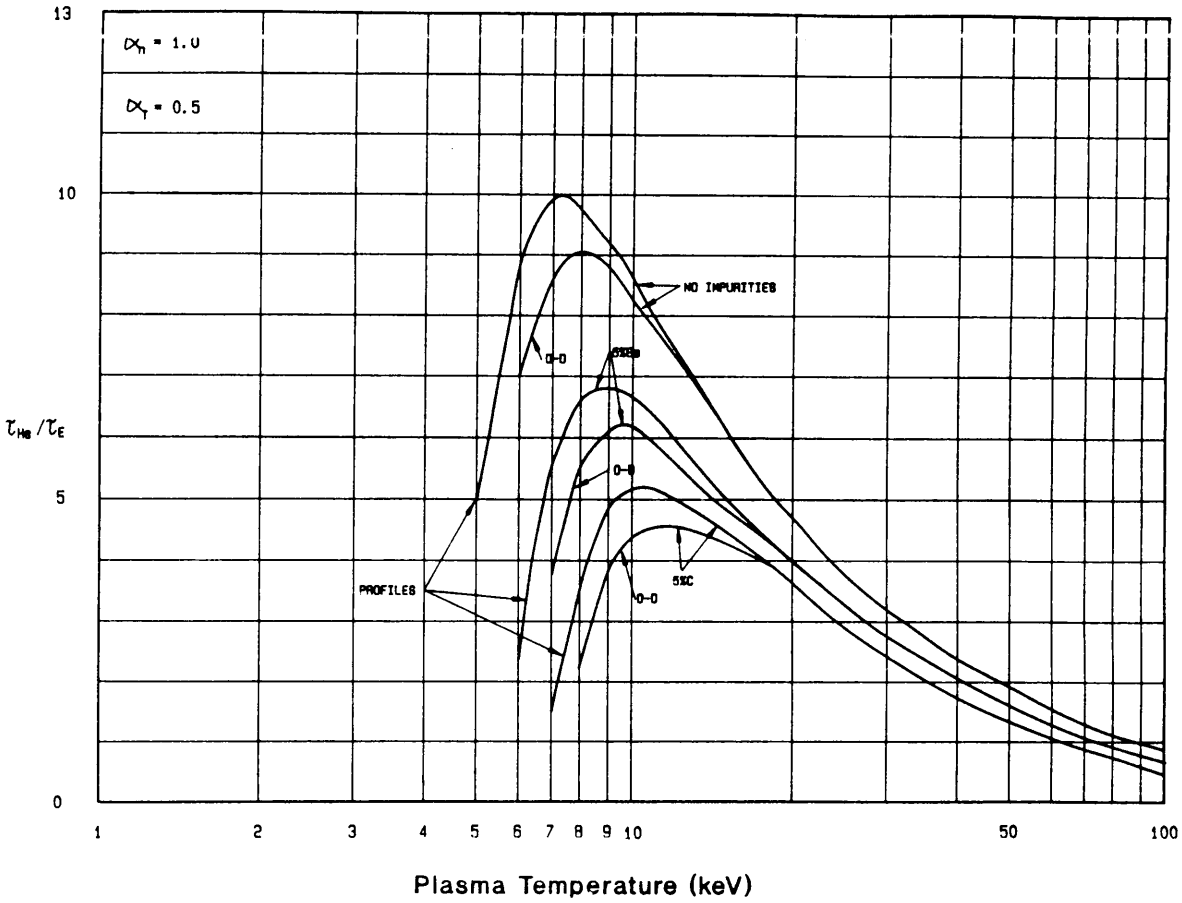

Figure 3.10: ξ **plotted against plasma temperature. The volume-averaged results are shown, together with the results from the zero-dimensional model for comparison for 10 % helium in the plasma, for the cases of no impurities, 5 % Be and 5 % C.**

Now $\xi = \xi(\bar{T}, f, f_i, Z_i)$ can be studied for different values of the dependent plasma parameters.

Fig. 3.10 shows ξ plotted against the plasma temperature for the same plasma parameters as in Fig. 3.1, with the plasma temperature in the zero-dimensional model corresponding to the mean temperature in the volume-averaged model. The volume-averaged results are shown, together with the results from the zero - dimensional model for 10 % helium in the plasma and for the cases of no impurities, 5 % Be and 5 % C. It is clear from these results that, although the addition of profiles to the zero - dimensional model changes the allowable ratio of helium particle confinement time to energy confinement time, the effect is very small. The profiles make the requirement a little less stringent than predicted by the zero-dimensional model.

The profile corrected model showed little dependence on the profile coefficients α over a range $0.5 \leq \alpha_n \leq 2$ and $0.5 \leq \alpha_T \leq 2$ which is a realistic class of profiles expected for reactor conditions [UCK88]. The results of different profile coefficients

on the model is shown in Fig. 3.11. The figure shows the ratio of the multiplcation term affected by the profile addition in the expression for ξ in eq. (3.18) of the zero-dimensional model, $E_\alpha - \frac{4(1+2f+f_i Z_i)(B+R)}{\langle\sigma v\rangle_{DT}}$, to the corresponding term in the volume-averaged case of eq. (3.75), $E_\alpha - 2\frac{(1+2f+f_i Z_i)R_0}{I}$ as a function of α_T for different values of α. The values represented are $kT(0) = 20$ keV, $f = 0.1$ and $f_i = 0$. From the figure it is clear that the different coefficients do not alter the ratio significantly from 1, indicating the small influence of the profiles. For increasing α_T in Fig. 3.11, the volume-averaged model indicates larger values of ξ, and the zero - dimensional model results in larger values of ξ for increasing α. This indicates that the limitation on ξ is relaxed for more peaked temperature profiles, and for less peaked density profiles.

3.5 Thermal stability of a D,T fusion reactor

3.5.1 Introduction

The thermal stability of fusion reactors operating with D,T plasmas has been under study for a long time, and has recently been reviewed [BOR87,SAG89]. Different methods, both active and passive, of control for this inherent instability exist.

In principle, for steady-state operation of a D,T fusion reactor, stable equilibrium points are needed in the operational parameter space. In effect this means that:

$$P_+ = P_- \tag{3.76}$$

where P_+ is the power produced from fusion reactions in the plasma volume, as well as other input power from external sources, like ohmic power, neutral beam injection, ICRH heating, etc. P_- is the power losses (P_{Conv}, P_{Rad}, P_{CX}, etc.) from the plasma, as already discussed in the previous sections. We have already shown zero-dimensional predictions of such operational areas in the $n_e\tau_E$, kT space given certain simplifying approximations. This requirement (eq. (3.76)) ensures that the temperature of the plasma does not increase due to excess power available in the plasma, or that the plasma temperature decreases due to excess losses.

Although implying a steady-state operational point, eq. (3.76) does not, however, guarantee the stability of such a point, and a further constraint must be fulfilled at such an operational point. The additional requirement may be expressed as:

$$\frac{dP_+}{dT} \leq \frac{dP_-}{dT} \tag{3.77}$$

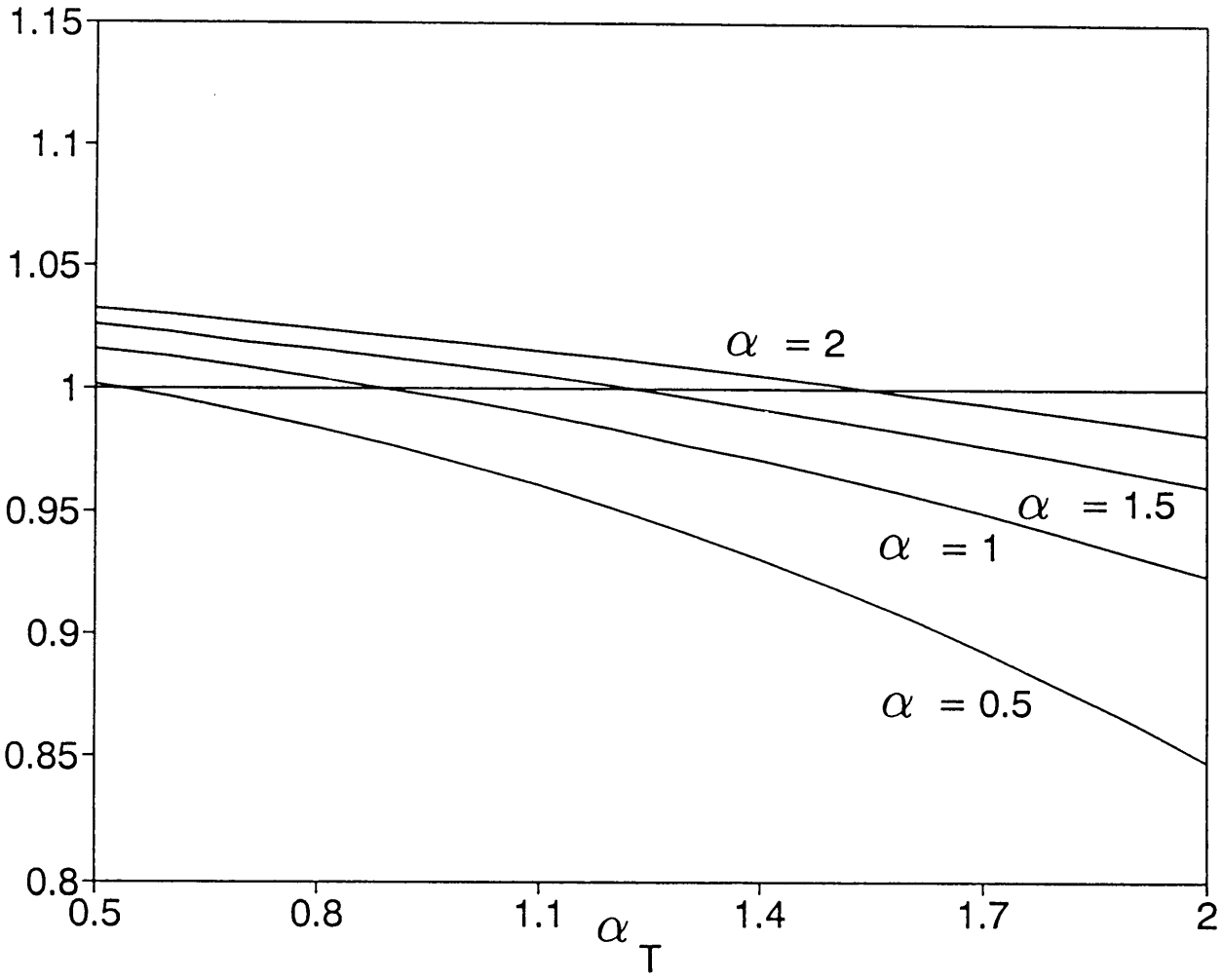

Figure 3.11: **The ratio of the multiplication term affected by the profile addition in the expression for ξ in the zero - dimensional model to the corresponding term in the volume-averaged case, as a function of α_T, for different values of α. The values represented are $kT(0) = 20$ keV, $f = 0.1$ and $f_i = 0$.**

This requirement describes the thermal behaviour of the plasma at the point when a perturbation of one or more of the plasma parameters occurs, i.e. the stability of the point. If this criterion is not satisfied, the plasma temperature will tend to decrease or increase naturally to a stable point or out of control, depending on the position in the parameter space. When eq. (3.77) is violated, for example, if the power produced increases by a small amount, the temperature will increase slightly, increasing the difference between the power produced and the power lost from the plasma. This will tend to let the temperature rise uncontrollably. On the other hand, if the power produced decreases slightly (or the power losses increase by a small amount) the temperature will decrease a fraction, making the nett losses even more, and the temperature will tend to decrease.

In general the solution to eq. (3.76) as a function of temperature has two solutions (at T_1 and T_2). This is indicated in Fig. 3.12 [RAE81] where the power produced by a typical steady-state reactor plasma due to fusion is indicated by the thick solid line. The losses are described by the dotted line (the sum of P_C and P_{Brems}), and the two points of intersection are where steady-state operation may be possible. From Fig. 3.12 it is, however, also clear that eq. (3.77) is only satisfied at point T_2. This temperature is normally also higher than T_1.

Even though the plasma temperature must be high enough to yield sufficient fusion reactions to maintain burn, there are certain limitations to the temperature range where reactor operation is viable. The plasma temperature is limited by the heat load transferred to the divertor plates, an engineering problem rather than a fundamental plasma limitation. The temperature must also be kept low enough to prevent the onset of magnetohydrodynamic (MHD) instabilities. This instability is expressed through the maximum plasma pressure ratio (β) allowed during operation. The limiting quantity β is expressed as the ratio of the hydrodynamic pressure due to the plasma density and temperature, to the magnetic pressure exercised by the magnetic field confining the plasma ions. It is desirable to operate at the highest possible β to maintain the highest possible rate for fusion, and to keep it constant during operation. When β exceeds a certain limit the plasma develop MHD instabilities and loss of confinement is experienced. The upper limit on β for stable operation is called the Troyon limit. This is taken to be 6 % [UCK88] and is the maximum value that the volume-averaged β can reach before the onset of ideal MHD instabilities.

For constant β, see also eq. (3.21), [GLA64] we have:

$$\beta = \frac{n_{tot} kT}{\frac{B^2}{2\mu_0}} \equiv \text{constant} \tag{3.78}$$

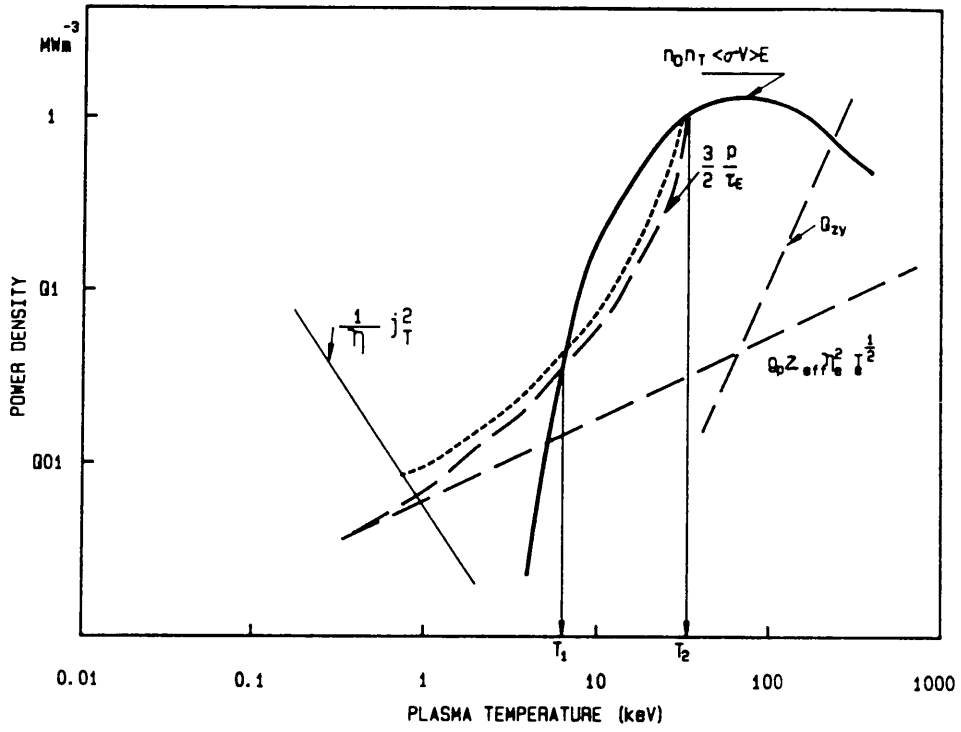

Figure 3.12: **The power produced by a typical steady-state reactor plasma due to fusion as indicated by the thick solid line. The losses are described by the dotted line (the sum of P_C and P_{Brems}), and the two points of intersection are where steady-state operation may be possible.**

For a clean D,T plasma $n_{DT} = n_{tot}/2$:

$$n_{DT} = \frac{\beta B^2}{4\mu_0 kT} \tag{3.79}$$

but from (3.46)

$$P_\alpha = \frac{n_{DT}^2}{4}\langle\sigma v\rangle E_\alpha \tag{3.80}$$

$$= \frac{\beta^2 B^4 E_\alpha}{64\mu_0^2}\frac{\langle\sigma v\rangle}{kT^2} \tag{3.81}$$

This dependence on $\frac{\langle\sigma v\rangle}{kT^2}$ of the fusion power shows a maximum value at a plasma temperature of $kT \approx 14$ keV [GLA64]. At higher temperatures than 14 keV the fusion power decreases rather quickly. This is the reason why the plasma temperature must be kept as close to 14 keV as possible for constant β. Another reason [MAN91] is that the stable points for D,T operation is situated in the high-temperature, low-density region of the operational space. Operating in this region will have serious implications for good divertor conditions, where a high-recycling (high density) low-temperature (low sputtering, less impurities) condition at the edge will be necessary to reduce thermal loads on the divertor plates. There is also the increasing risk of disruptions at higher temperatures, and increased ablation of pellets for pellet fuelling, making deep-penetration fuelling difficult.

A further factor limiting the plasma temperature is the scaling of τ_E with the temperature. Here the scaling of Uckan [UCK88] has been adopted and only the temperature influence was taken into account, assuming that $\tau_E = 2$ s at $kT = 20$ keV. This scaling has the form:

$$\tau_E \propto kT^{-1.38} \tag{3.82}$$

indicating that the energy confinement time decreases strongly with increasing plasma temperature.

The maximum operational temperature is also limited by the corresponding edge temperature. As mentioned in section 3.5.5 the edge temperature is limited to 150 eV and 50 eV for low Z and high Z plasma-facing components respectively. When this restriction is violated, excess impurity radiation and/or fuel dilution will prohibit steady-state operation.

A further restriction placed on the operational temperature is the power flux onto the divertor plates. The maximum power density that can be handled by the plates

is $\approx$ 10 to 15 MW/m^2 [IGI90]. For a plasma vessel with a 10 m^2 area of irradiation, and a plasma volume of 1 000 m^3, the maximum volume-averaged power density convected and conducted to the plates is $\approx 1.5 \cdot 10^5$ W/m^3. This places a strict limitation on the operation of a D,T reactor, where these power fluxes are readily attainable. A solution to this problem is the creation of a radiating layer with relatively low temperature at the edge of the plasma, thereby radiating a fraction of this energy away before it is concentrated onto the plates. This condition is also compatible with the high recycling regime already discussed.

In what follows, simulations are presented that enable the steady-state stable operational points to be found subject to the above-mentioned criteria. The solution to the intrinsic stability problem is either to decrease T_2 or to make T_1 stable. There are several static and dynamic ways to affect the stability of an operational point.

Active ways [MAN91] are inter alia auxiliary power modulation, modification of fuel injection rate and/or mixture, and injection of impurities.

Auxilliary power modulation is the modification of the amount of external power applied to the plasma in direct response to the plasma temperature, or some other plasma parameter. Through this mechanism the fusion rate is controlled, and stability therefore maintained.

The amount of fuel present directly affects the fusion reaction rate (which depends on the square of the fuel density), therefore modification of the fuelling rate can also be used to control the temperature of a reactor. The ratio of deuterium to tritium density can also be varied to create a similar effect [BOR87]. Injection of high Z impurities leads to higher radiation losses, which in turn have a damping effect on the nett power, and therefore the plasma temperature.

Some examples of passive control mechanisms are:

When the temperature increases the losses from cyclotron radiation increases, and this tends to limit the increase. The scaling of the energy confinement time (τ_E) with temperature [CHR90,UCK88] is such that τ_E decreases with increasing temperatures, and therefore an increase in temperature will be opposed by the higher conductive and convective losses from the plasma. In what follows some of these passive mechanisms discussed will be applied to a burning plasma. When the plasma temperature increases the reaction rate of the D,T plasma increases, producing more helium, which leads to higher fuel dilution and radiation losses from the plasma. The second mechanism concerns impurities allowed into the plasma. When the temperature increases the power convected from the plasma increases. This tends to increase the edge temperature, and therefore the mean energy of the ions leaving the plasma that hit the limiter/divertor. In general this leads to higher sputtering yields of the limiter material, resulting in higher impurity concentrations in the plasma. This

results in radiative losses and fuel dilution, tending to keep the temperature low.

The study undertaken in this section is an endeavour to establish simple criteria for the existence of stable operating points through the study of the mechanisms mentioned above.

3.5.2 General definitions

In what follows we assume that :

$$kT_e(0) = kT_D(0) = kT_T(0) = kT_\alpha(0) = kT_i(0) = kT(0) \tag{3.83}$$

i.e. the temperatures of all species are equal at the centre of the plasma volume. Similarly we set:

$$kT_e(a) = kT_D(a) = kT_T(a) = kT_\alpha(a) = kT_i(a) = kT(a) \tag{3.84}$$

i.e. the temperatures of all the relevant ion species at the last closed flux surface ($r = a$) are equal. We also assume the same peakedness for the different density profiles, viz:

$$n_{ea} = \frac{n_e(a)}{n_e(0)} = \frac{n_D(a)}{n_D(0)} = \frac{n_T(a)}{n_T(0)} = \frac{n_i(a)}{n_i(0)} = \frac{n_{He}(a)}{n_{He}(0)} \tag{3.85}$$

A further assumption is that $n_e(r)$ stays constant with time through refuelling or another control method.

The ratio of the helium confinement time with respect to the energy confinement time is chosen as a constant, i.e.:

$$\tau_{He} = \xi \tau_E \tag{3.86}$$

The profiles considered are similar to those discussed in (3.33) and (3.34), except for the additional constraint that the densities of species are not necessarily 0 at $r = a$. The densities and temperature are then described by the following expression:

$$g(r) = g_0(1 - \frac{r^2}{a^2})^\alpha + g(a) \tag{3.87}$$

with $g(0) = g_0 + g(a)$ where g(r) indicates density or temperature of the plasma species. We also assume that $g(0) \gg g(a)$, resulting in $g(0) \approx g_0$, and $g(0)^2 \approx g_0^2$. Quasi-neutrality also requires that:

$$n_e(0) = n_{DT}(0) - 2n_{He}(0) - n_i(0)Z_i \tag{3.88}$$

Averages of quantities are found in the way described by (3.68) and (3.69).

3.5.3 Helium exhaust

The helium time-dependent particle balance is given by (3.71), and consistent with the previous assumptions we have:

$$n_{DT}^2 = [n_{DT0}(1 - \frac{r^2}{a^2})^\alpha + n_{DT}(a)]^2 \tag{3.89}$$

$$\approx n_{DT0}^2(1 - \frac{r^2}{a^2})^{2\alpha} \tag{3.90}$$

Definitions (3.71) and (3.86) thus leads to the expression

$$\frac{d\bar{n}_{He}}{dt} = \frac{n_{DT0}^2}{2} I(kT) - \frac{\bar{n}_{He}}{\xi\tau_E} \tag{3.91}$$

with

$$I(kT) = \int_0^1 (1 - x^2)^{2\alpha} \langle\sigma v\rangle x dx \tag{3.92}$$

Differentiation of the left-hand side after substitution of the definition of f (eq. (3.43)) yields:

$$(1 + f_i Z_i)\frac{df}{dt} - f Z_i \frac{df_i}{dt} = \frac{n_e(0)(1+\alpha)I(kT)}{2} - \frac{(1 + 2f + Z_i f_i)f}{\xi\tau_E} \tag{3.93}$$

and finally this can be written as:

$$\frac{df}{dt} = \frac{1}{(1 + Z_i f_i)}[\frac{n_e(0)(1+\alpha)I(kT)}{2} - \frac{(1 + 2f + Z_i f_i)f}{\xi\tau_E} + f Z_i \frac{df_i}{dt}] \tag{3.94}$$

3.5.4 Energy balance considerations

The global energy balance is given by the balance of the gains and losses in the power terms:

$$\frac{3}{2}\frac{d}{dt}\overline{n_{tot}kT} = \bar{P}_{\alpha} - \bar{P}_{Brems} - \bar{P}_{Rad} - \bar{P}_{C} \tag{3.95}$$

with n_{tot} the total particle density of the plasma, and $\bar{P}_{\alpha}$, $\bar{P}_{Brems}$, $\bar{P}_{Rad}$ and $\bar{P}_{C}$ the α power, bremsstrahlung, radiation and convective power losses in the burning plasma, as defined in section 3.3 with resulting eqs. (3.46), (3.52), (3.55) and (3.65).

Now it is easy to obtain that:

$$\overline{n_{tot}kT} = \frac{(2+3f+(Z_i+1)f_i)}{(1+2f+f_iZ_i)}\frac{n_e(0)kT(0)}{(1+\alpha+\alpha_T)} \tag{3.96}$$

Thus the left-hand side of eq. (3.95) becomes:

$$\frac{3}{2}\frac{d}{dt}\overline{n_{tot}kT} = \frac{\frac{3}{2}\bar{n}_e}{(1+2f+f_iZ_i)}\{\overline{kT}G + (2+3f+(Z_i+1)f_i)\frac{d\overline{kT}}{dt}\} \tag{3.97}$$

with

$$G = \frac{[(Z_i-2)f_i-1]\frac{df}{dt} + [(1-Z_i)+(2-Z_i)f]\frac{df_i}{dt}}{[1+2f+f_iZ_i]} \tag{3.98}$$

Using eqs. (3.95), (3.97) and (3.98) we find:

$$\begin{aligned}\frac{d\overline{kT}}{dt} &= \frac{2(1+\alpha)^2}{3[2+3f+(Z_i+1)f_i]}\{\frac{E_{\alpha}\bar{n}_eI(kT)}{2(1+2f+f_iZ_i)} - \frac{K\bar{n}_e\sqrt{kT(0)}[1+4f+f_iZ_i^2]}{1+2\alpha+0.5\alpha_T} \\ &- 2\bar{n}_ef_iK_2I_2 - \frac{3\overline{kT}[2+3f+(Z_i+1)f_i]}{2(1+\alpha)^2\tau_E} - \frac{3}{2(1+\alpha)^2}\overline{kT}G\}\end{aligned} \tag{3.99}$$

on condition that if $Z \leq 6$ then $K_2 = 0$, and if $Z > 6$, then $f_i = 0$ in the bremsstrahlung term.

3.5.5 Impurities

The model as described by McCracken *et al.* [MCC87A,MCC90] is used to take account of the generation and influence of impurities on the plasma. The average power density convected to the limiters, or divertor plates, is given by $\bar{P}_C$ described by eq. (3.65). The total power convected to the limiters/divertors ($V\bar{P}_C$), as contributed by all the particle species in the plasma, is given by:

$$\begin{aligned} V\bar{P}_C &= P_D + P_T + P_\alpha + P_i + P_e \\ &= e\lambda_n L_{Lim}[\gamma_D \Gamma_D(a) kT_D(a) + \gamma_T \Gamma_T(a) kT_T(a) + \gamma_\alpha \Gamma_\alpha(a) kT_\alpha(a) \\ &+ \gamma_i \Gamma_i(a) kT_i(a) + \gamma_e \Gamma_e(a) kT_e(a)] \end{aligned} \tag{3.100}$$

where V is the volume of the plasma column, P_i is the power deposited by the different plasma species onto the divertor plates, γ_i are the sheath transmission factors of the different species, λ_n is the e-folding length of the plasma outside the last closed flux surface, and $L_{Lim} = 2L$ is the limiter arc length. $\Gamma_i(a)$ and $kT_i(a)$ are the edge particle flux and edge temperature of particle i respectively. We assume $\gamma_D = \gamma_T = \gamma_\alpha = \gamma_i = \gamma_e = \gamma$. From simple plasma sheath considerations and the Bohm criterion [CHE74] we have:

$$\Gamma_i(a) = n_i(a) c_s \tag{3.101}$$

where the acoustic speed c_s is described by eq. (2.12), i representing all the ion species in the plasma. For the electrons we assume a Boltzmann distribution at the last closed flux surface, yielding:

$$\Gamma_e(a) = \frac{1}{4} n_e(a) \bar{c}_e (1 - \delta) e^{\frac{e\phi}{kT}} \tag{3.102}$$

where δ is the secondary electron emission coefficient, and $\bar{c}_e = \sqrt{\frac{8kT(a)}{\pi m_e}}$. ϕ is the sheath potential between the plasma and material, and kT the edge temperature.

From these relations it is easy to obtain the edge temperature as a function of the convected power, assuming a fixed value for $\frac{e\phi}{kT} \approx -3$ [STA90] in a hydrogen isotope plasma:

$$T(a) = \{\frac{V\bar{P}_C(1 + 2f + f_i Z_i)}{e^{1.5}\gamma\lambda_n L_{Lim} n_e(a)}\}^{\frac{2}{3}} \{\sqrt{\frac{1}{2m_D}} + \sqrt{\frac{1}{2m_T}} + f\sqrt{\frac{3}{m_\alpha}}$$

$$+ \quad f_i\sqrt{\frac{Z_i+1}{m_i}} + \frac{1}{4}(1-\delta)(1+2f+f_iZ_i)e^{\frac{e\phi}{kT}}\sqrt{\frac{8}{\pi m_e}}\}^{-\frac{2}{3}} \qquad (3.103)$$

We also assume that the edge electron density has a linear dependency on the central electron density, i.e. $n_e(a) = n_{ea}n_e(0)$ [STA90].

The energy of impact of an ion falling through the sheath is dependent on the edge temperature, and is given by [CHE74]:

$$E_i = 2kT_i(a) - Z_ie\phi \qquad (3.104)$$

and for $e\phi \approx -3kT$, with the electron and ion temperatures at the edge equal, it is found that:

$$E_i = kT(a)(2+3Z_i) \qquad (3.105)$$

For each species we now assume a mono - energetic flux of ions to the limiters or divertors, with the energy given by eq. (3.105). The fluxes of ions to the material will cause sputtering of the limiter/divertor material, and some of this material will enter the plasma as impurities. The sputtering yield of ions has been measured extensively before [ROT90], and we have used the semi-analytical fit to the sputtering yield by Bohdansky [LAN84] to model the yield of impurity atoms eroded from the material surface. The sputtering yields are represented by $Y_D(E_D)$, $Y_T(E_T)$, $Y_\alpha(E_\alpha)$ and $Y_i(E_i)$ for deuterium, tritium, helium and impurities respectively. From eq. (3.105) we have $E_D = 5kT(a) = E_T$, $E_\alpha = 8kT(a)$, $E_i = (2+3Z_i)kT(a)$.

A fraction of the sputtered atoms is ionised in the edge region and they are returned to the divertor face. The total flux of particles into the plasma, with a screening factor q (the ratio of the impurity flux that reaches the plasma volume, to the total sputtered flux) is given by:

$$\Gamma_{in} = \gamma q\lambda_n L_{Lim}[\Gamma_D Y_D(E_D) + \Gamma_T Y_T(E_T) + \Gamma_\alpha Y_\alpha(E_\alpha) + \Gamma_i Y_i(E_i)] \qquad (3.106)$$

Mandrekas [MAN91] fitted the screening factor to model the impurity concentrations in ITER to obtain compatibility with the ITER physics guideline [UCK88A]. Here, however, the term can be used to assess the effect of the magnitude of the screening factor on the operation of a reactor.

The impurity balance is then given in the same context as before by:

$$\frac{d\bar{n}_i}{dt} = \frac{\Gamma_{in}}{V} - \frac{\bar{n}_i}{\tau_i} \qquad (3.107)$$

and doing the full calculation, the impurity balance is given by:

$$\frac{df_i}{dt} = 2f_i[\frac{\bar{n}_e(1+\alpha)^2 I(kT)}{2(1+2f+f_iZ_i)} - \frac{f}{\tau_{He}}] + (1+f_iZ_i) \tag{3.108}$$

$$\cdot\ [\frac{\gamma q n_{ea}\lambda_n L_{Lim}\sqrt{kT(a)}(1+\alpha)}{V}\Gamma_{eff} - \frac{f_i}{\xi\tau_E}] \tag{3.109}$$

with

$$\Gamma_{eff} = 0.5\sqrt{\frac{2}{m_D}}Y_D(E_D) + 0.5\sqrt{\frac{2}{m_T}}Y_T(E_T) + f\sqrt{\frac{3}{m_\alpha}}Y_\alpha(E_\alpha) + f_i\sqrt{\frac{Z_i+1}{m_i}}Y_i(E_i) \tag{3.110}$$

Eqs. (3.94), (3.99) and (3.109) can now be solved simultaneously to give the time-dependent evolution of a burning plasma, actively involving the creation of helium through fusion and of impurities from the plasma-facing components. The equations were numerically solved and the results for a typical D,T plasma are shown in Figs. 3.13, 3.14, 3.15 and 3.16.

In Fig. 3.13 and 3.14 a stable operational condition is shown for carbon plasma-facing material, that is, the sputtering yields applicable to carbon sputtering were used in eq. (3.110). The starting values assumed were $\overline{kT} = 20$ keV, $\bar{n}_e = 1 \cdot 10^{20}$ m^{-3}, $f = 0.03$, $f_i = 0$, $\frac{\tau_i}{\tau_E} = 3$ and $\frac{\tau_{He}}{\tau_E} = 1$. It can be clearly seen that the starting point is unstable, and the plasma adjusts itself to obtain stability. In Fig. 3.13 the plasma temperature ($\overline{kT}$), helium concentration (f) and the carbon impurity concentration (f_i) are shown as a function of time.

The way in which the operational point is reached illustrates the mechanism of obtaining stable operating points within the restricting conditions. In Fig. 3.14 the edge temperature, α power and convected power density are shown. The values for the limiting quantities are: $\bar{P}_C = 4 \cdot 10^5$ W, $kT_{edge} = 105$ eV and $\beta = 3.8$ %. In this case 62 % of $\bar{P}_C$ must be radiated away to maintain divertor integrity.

In Fig. 3.15 and 3.16 the same quantities are shown, with the same starting conditions, except for $\frac{\tau_{He}}{\tau_E} = 3$. It can be seen that this quantity leads not only to unstable operation, but the plasma is extinguished, due to the larger confinement time of the helium in the plasma.

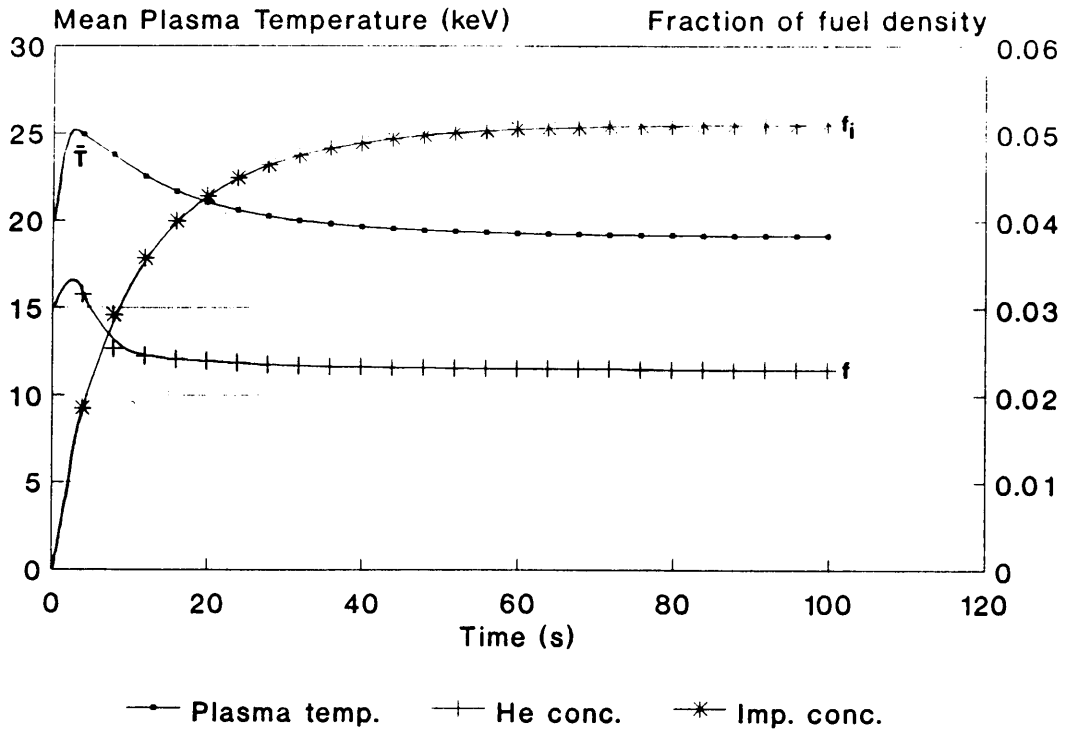

Figure 3.13: **Time-dependent operation of a D,T reactor leading to stable operational conditions. The traces indicated are mean plasma temperature, mean helium concentration and impurity concentration.**

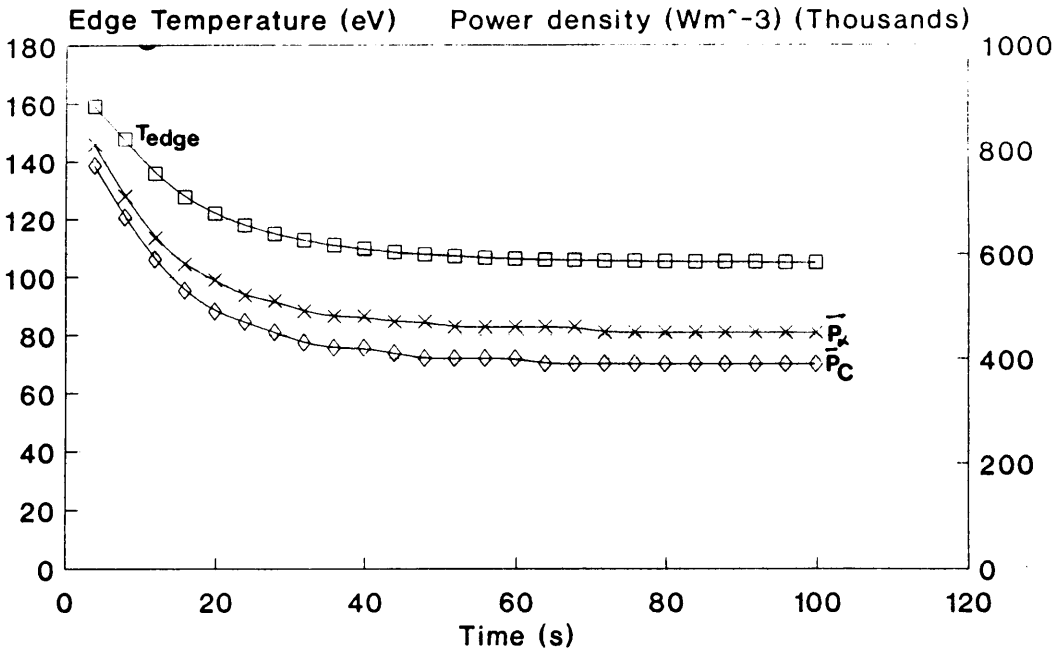

Figure 3.14: **Time-dependent operation of a D,T reactor leading to stable operational conditions. The traces indicated are edge temperature and power densities $\bar{P}_\alpha$ and $\bar{P}_C$.**

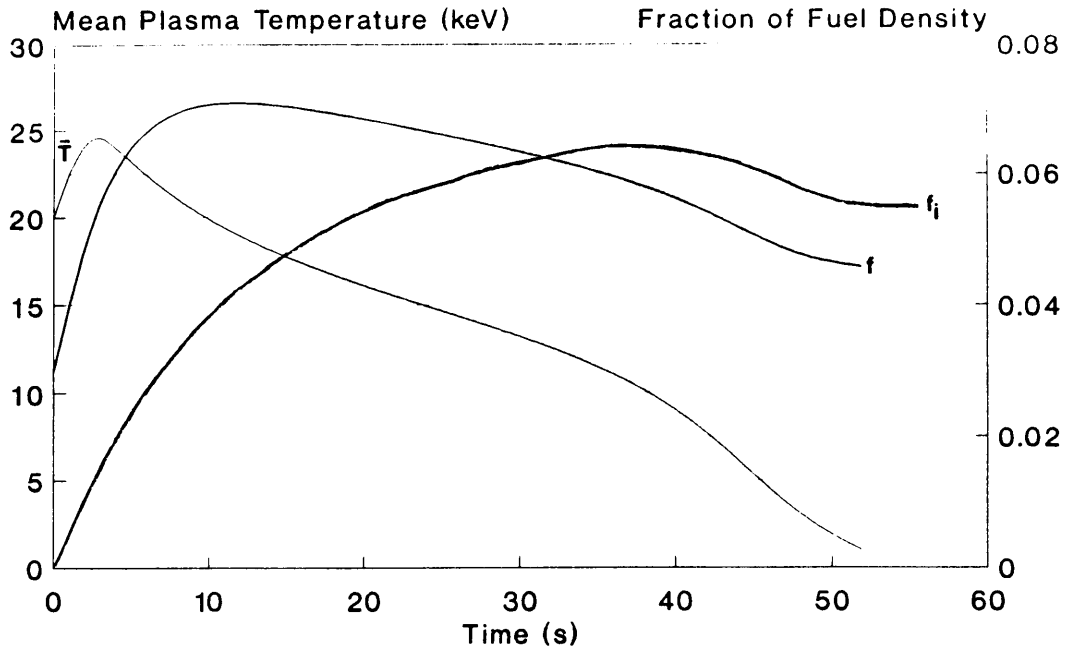

Figure 3.15: **Time-dependent operation of a D,T reactor with starting conditions leading to poisoning of the plasma due to the impurities and helium accumulation. The traces indicated are mean plasma temperature, mean helium concentration and impurity concentration.**

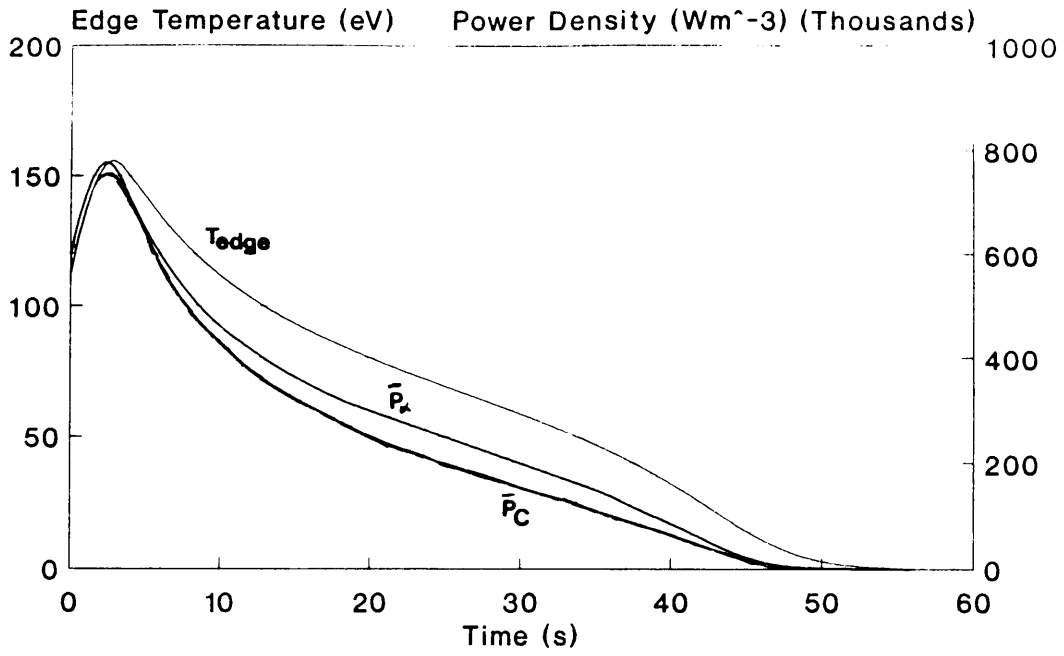

Figure 3.16: **Time-dependent operation of a D,T reactor with starting conditions leading to poisoning of the plasma due to the impurities and helium accumulation. The traces indicated are edge temperature and power densities $\bar{P}_\alpha$ and $\bar{P}_C$.**

3.5.6 Steady-state solutions

From eqs. (3.94) and (3.99) we obtain the helium particle balance and energy balance for steady-state operation. These can be expressed as:

$$f_i = \frac{1}{Z_i}[\frac{n_e(0)(1+\alpha)I(kT)\xi\tau_E}{2f} - 1 - 2f] \tag{3.111}$$

and:

$$\frac{E_\alpha \bar{n}_e I(kT)}{2(1+2f+f_i Z_i)} - \frac{K\bar{n}_e\sqrt{kT(0)}(1+4f+f_i Z_i^2)}{(1+2\alpha+0.5\alpha_T)} \tag{3.112}$$

$$- \quad 2\bar{n}_e f_i K_2 I_2 - \frac{3\overline{kT}[2+3f+(Z_i+1)f_i]}{2(1+\alpha)^2\tau_E} = 0 \tag{3.113}$$

respectively. The impurity balance for the steady-state, however, can be found [MCC90] through the dependence of the central impurity concentration on the flux of impurities (Γ_{in}) into the plasma, as found in the Engelhardt solution [ENG78]. This solution was obtained by solving the steady-state, one-dimensional diffusion equation for the impurities. A direct relation between the central impurity concentration $n_i(0)$ and the flux of impurities into the plasma was found, being described by:

$$n_i(0) = \frac{\Gamma_{in}(\lambda_i + \lambda_n)}{A_p D_\perp} \tag{3.114}$$

with A_p the plasma surface and λ_i the impurity ionisation length. If it is also assumed that $D_\perp \approx a^2/\tau_i = a^2/\xi_i\tau_E$, and using eqs. (3.106) and (3.114) the steady-state impurity concentration is found to be:

$$f_i = \frac{\Gamma_{in}(\lambda_i+\lambda_n)\xi_i\tau_E(1+2f+f_i Z_i)}{4\pi^2 a^3 R n_e(0)} \tag{3.115}$$

An estimate of the impurity enrichment at the edge for steady-state operation can also be obtained [STA90] from such a description, namely:

$$\frac{n_i(a)}{n_e(a)} \approx Y_{eff}\frac{D_\perp^{DT}}{D_\perp^i}\frac{\lambda_i}{\lambda_n} \tag{3.116}$$

and with the assumptions that $D_\perp^{DT} \approx D_\perp^i$ and $\lambda_i \approx \lambda_n$:

$$\frac{n_i(a)}{n_e(a)} \approx Y_{eff} \tag{3.117}$$

with Y_{eff} described by:

$$Y_{eff} = \frac{Y_D + Y_T + Y_\alpha}{1 - Y_i} \tag{3.118}$$

the effective sputtering yield. No edge enrichment for helium was assumed.

From the relations (3.111), (3.113), (3.115) and (3.118) the steady-state helium concentration, plasma temperature and impurity concentration in the plasma can be obtained for specific plasma conditions.

3.5.7 Results

Fig. 3.17 denotes the operational lines in $\bar{n}_e$, kT space (the analogy of Fig. 3.2) for $\frac{\tau_{He}}{\tau_E}$ equals 3, 2 and 1 (solid lines) and $\frac{\tau_i}{\tau_E}$ equal to 3. It was therefore assumed that the α and energy transport are coupled, but a fixed ratio was assumed between the impurity confinement time and the energy confinement time. Also shown is the burn criterion curve (broken lines) in the absence of helium and impurities. The maxima of the limiting quantities $\bar{P}_C$, T_{edge} and β are also indicated on the curves, and show the critical dependence of the power load limit on the divertor plates.

For calculational purposes the screening factor was held constant, with the value of $q \sim 0.05$ as suggested by Langer and Singer [LAN85] in their steady-state analysis.

Comparison between the time-dependent simulations and the steady-state results was achieved with $q = 0.0012$ in the time dependent case, with q about 40 times bigger ($q = 0.05$) for the steady-state case. This difference is understandable as a direct comparison of the two models leads to the expression $\frac{\lambda_i + \lambda_n}{a} \approx 1$, differing by approximately a factor of 50 from realistic values for λ_i, λ_n and a. This factor shows the time-dependent model to have a very strong effect with respect to the impurity generation on maintaining steady-state burning conditions in the plasma.

The two operational simulations discussed in the previous section are also indicated. The starting points for both simulations were at point A, they moved along the curve to point B determined by the scaling of τ_E. From here the stable simulation moved to point C, a stable operating point. For the unstable simulation, however, the helium was confined for such a time that the temperature decreased, and the plasma was extinguished (D).

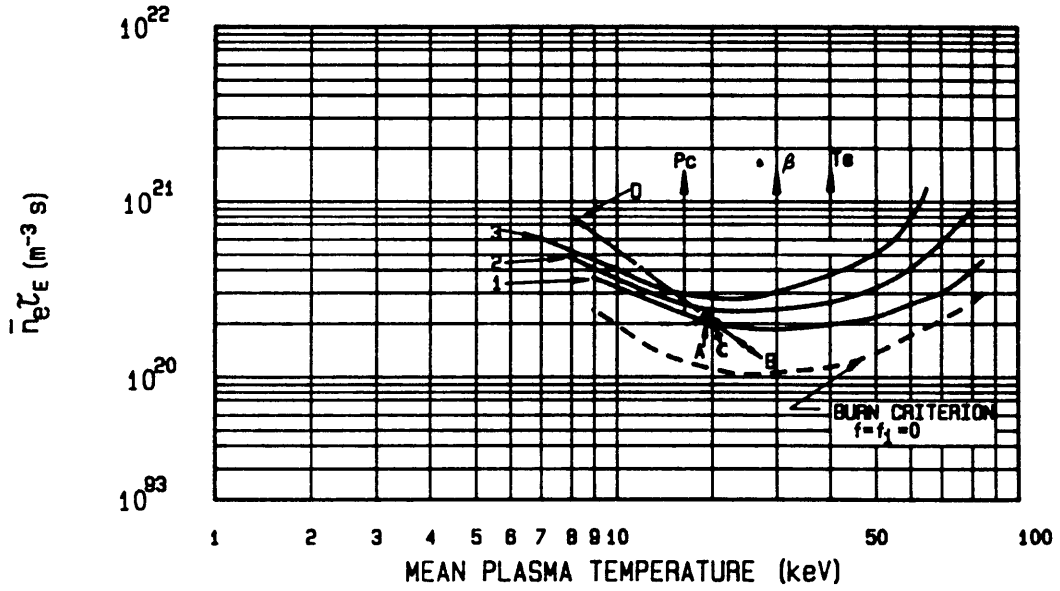

Figure 3.17: **The operational lines for $\frac{\tau_{He}}{\tau_E}$ equals 3, 2 and 1. $\frac{\tau_i}{\tau_E}$ was kept equal to 3. Also shown is the burn criterion curve (- - -) for no helium or impurities. The maxima of the limiting quantities $\bar{P}_C$, T_{edge} and β are also indicated.**

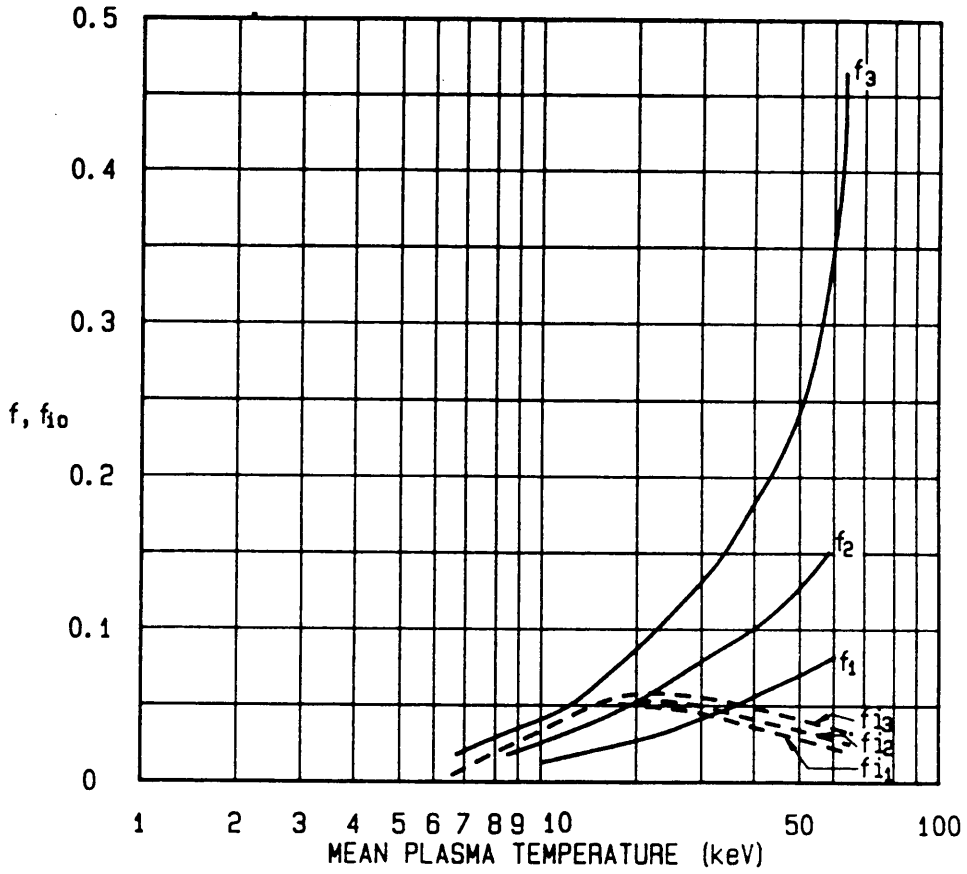

Figure 3.18: **The stable operational values of f and f_i as a function of mean plasma temperature for $\frac{\tau_{He}}{\tau_E}$ equals 3, 2 and 1. The ratio of impurity confinement time to energy confinement time was kept constant at 3.**

The stable operational values of f and f_i are shown in Fig. 3.18, for the same conditions as in Fig. 3.17. The different values of ξ has only a small influence on the impurity content of the plasma, mainly because the ratio of impurity confinement time to energy confinement time was kept constant at 3. The decrease in impurity concentration above 30 keV was due to the decrease in the effective sputtering yield at the higher edge temperature.

There is a marked difference in the helium concentration present in the plasma, e.g. at 20 keV values of 2.5 %, 5 % and 8 % for $\frac{\tau_{He}}{\tau_E} = 1$, 2 and 3 must be tolerated. This difference has great impact on the operation of a reactor, as it has been shown [POS91] that if the helium concentration for ITER, nominally taken as 10 %, can be reduced to 5 %, then the plasma current will be reduced by 5 MA, the H mode enhancement factor from 2 to 1.6 and the tritium inventory will be decreased by 50 %. The lifetime of the divertor plates will also be extended by 25 %, and in the technology phase, the pulse length will be increased by 70 %.

Fig. 3.19 shows the corresponding α power curves for three values of ξ. The α

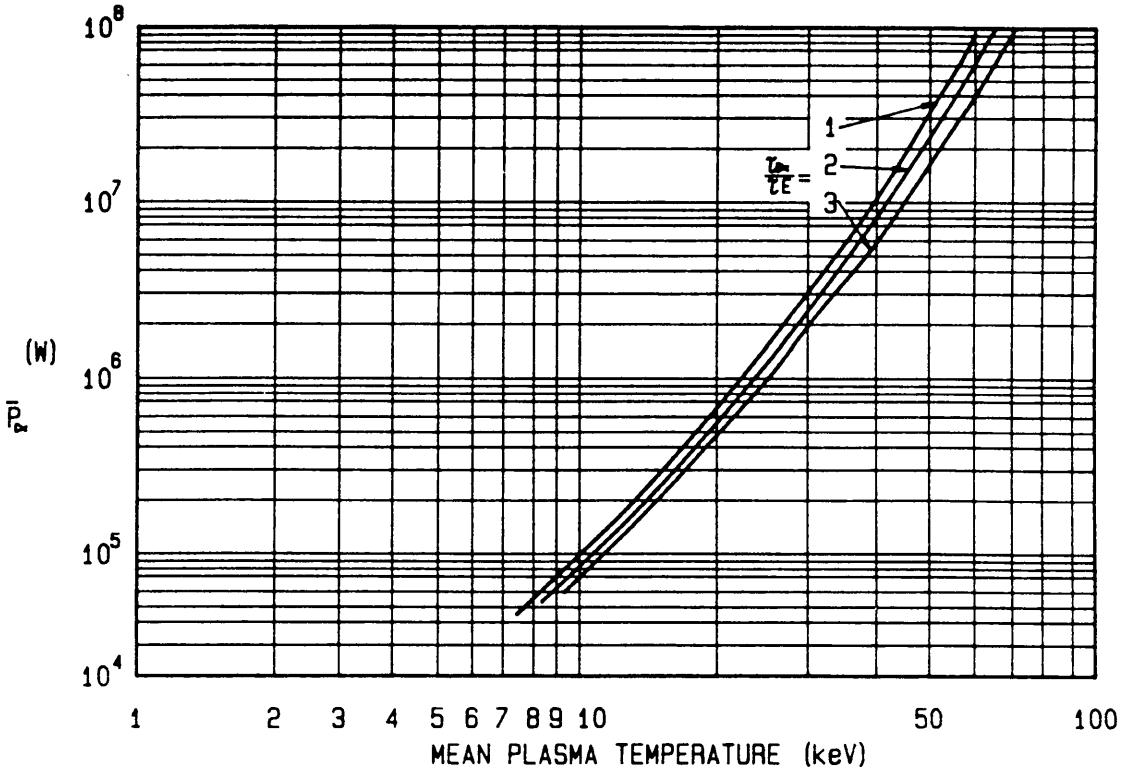

Figure 3.19: **The α power curves for the three ratios of ξ versus mean plasma temperature for $\frac{\tau_{He}}{\tau_E}$ equals 3, 2 and 1. $\frac{\tau_i}{\tau_E}$ was kept equal to 3.**

power densities are not very different, being determined by the dilution of the fuel by helium. The steep slope, similar to P_C, indicate the influence of increasing temperature on the plasma-facing components.

3.6 One-dimensional analysis of helium and energy confinement in a steady-state D,T fusion reactor.

3.6.1 Introduction

The zero-dimensional and the volume averaged analyses described earlier in section 3.2 and 3.4, and the other similar analyses mentioned [REI90,TAY90,REI90A], have the advantage that the analyses are simple enough to obtain direct physical insight from the results obtained. This is naturally also a drawback of such an analysis,

as the validity of the results may be in question. This is also the case for the analyses presented so far, as they are based on global estimates of very complex three-dimensional problems. The next step from these zero-dimensional models is to use computer codes solving the transport equations in one-dimensional space [RED89,RED90,RED91]. Even in these codes the direct physical insight is largely lost due to the complexity of the physics, and hence the complexity of the codes.

The validity, although somewhat qualitatively, of the zero-dimensional model is now established. The inclusion of profiles effects in the analysis, however, does pose a consistency problem. In the extensions to the models in section 3.3 and [REI90A] profiles effects are added in an *ad hoc* way, with the form of the profiles those experimentally obtained in tokamaks, e.g. [UCK88]. At the same time the ratio of helium to energy confinement time is arbitrarily selected. Although the results have shown that the ratios (ξ) obtained are not a strong function of the profile shape used, the profile types and the ratio of helium to energy confinement are closely coupled, and cannot be selected arbitrarily.

It is clear that the helium diffusion coefficient D will determine directly the helium profile, and the same is true for the effect of χ on the temperature profile. What follows is an attempt to study the effect of the transport coefficients on the profile shapes. The assumptions made are at least comparable to those made in the zero-dimensional model, and the results of the two approaches are also compared.

3.6.2 Transport of helium and energy

Consider a one-dimensional analysis of a burning tokamak reactor operating with a D,T plasma, including one impurity element in addition to the helium ash in the plasma. The plasma is assumed to be cylindrical, and all quantities are assumed to be a function of the small radius only.

In this analysis the plasma is divided into a central ($0 \leq r \leq r_0$) region, where the transport of helium originating from the fusion process is considered, and an edge region ($r_0 \leq r \leq a$), where the fusion rate is assumed to be negligible.

In the inner region the helium and impurity constituent are assumed to be fully ionised. For an impurity like carbon, this limits the choice for the inner region to a radial position where the plasma temperature is $> 100 - 200$ eV, approximately the energy where both carbon and helium are fully ionised. The choice of r_0 plays no further role, and no recycling is assumed.

The profiles of the electron density and the temperature (assumed equal for all species) are described by the following equations (see (3.33) and (3.34)):

$$n_e(r) = n_{e0}(1 - \frac{r^2}{a^2})^{\alpha_e} \tag{3.119}$$

$$kT(r) = kT_0(1 - \frac{r^2}{a^2})^{\alpha_T} \tag{3.120}$$

The helium density in the region $0 \leq r \leq r_0$ is given by:

$$n_{He}(r) = n_{\alpha 0}(1 - \frac{r^2}{a^2})^{\alpha_{He}} \tag{3.121}$$

The fusion reaction rate is given by the approximation:

$$\langle \sigma v \rangle_{DT}(r) = C_0 kT(r)^2 \tag{3.122}$$

with the reaction rate assumed to be zero outside the radius r_0.

The continuity equations, ignoring the inward pinch velocity, governing the helium with different charge states (n_{HeIII}, being the density of doubly ionised helium, n_{HeII} the singly ionised helium, and n_{HeI} neutral helium) over the entire region are:

$$\vec{\nabla} \cdot n_{HeIII}\vec{v}_{HeIII} = n^2\langle \sigma v \rangle_{DT} - n_{HeIII}n_e R_{III,II} + n_{HeII}n_e S_{II,III} \tag{3.123}$$

$$\begin{aligned} \vec{\nabla} \cdot n_{HeII}\vec{v}_{HeII} &= n_{HeIII}n_e R_{III,II} + n_{HeI}n_e S_{I,II} \\ &- n_{HeII}n_e S_{II,III} - n_{HeII}n_e R_{II,I} \end{aligned} \tag{3.124}$$

$$\vec{\nabla} \cdot n_{HeI}\vec{v}_{HeI} = n_{HeII}n_e R_{II,I} - n_{HeI}n_e S_{I,II} \tag{3.125}$$

where R and S are the recombination and ionisation rates respectively. Combining equations (3.123), (3.124) and (3.125):

$$\vec{\nabla} \cdot [n_{HeIII}\vec{v}_{HeIII} + n_{HeII}\vec{v}_{HeII} + n_{HeI}\vec{v}_{HeI}] = n^2\langle \sigma v \rangle_{DT} \tag{3.126}$$

where $n = n_D = n_T$, the densities of the deuterium and tritium fuel.

3.6.3 The helium density

The electron density is:

$$n_e(r) = 2n + 2n_{HeIII} + n_i Z_i$$

Z_i represent the fully ionised state of the impurity element in the inner region. This can be rewritten as:

$$n = \frac{n_e}{2} - n_{He} - \frac{n_i Z_i}{2} \tag{3.127}$$

with the notation HeIII now written as α for simplicity. Now for $0 \leq r \leq r_0$ eq. (3.126) reduces to:

$$\vec{\nabla} \cdot n_{He}\vec{v}_\alpha = n^2 \langle \sigma v \rangle_{DT} \tag{3.128}$$

Using Fick's law, in cylindrical coordinates, and assuming that n_{He} and n_i are relatively small compared to n_e and making use of eq. (3.127) we find:

$$\frac{\partial}{\partial r} r(-D n'_{He}) \approx (\frac{n_e^2}{4} - n_e n_{He} - \frac{n_e n_i Z_i}{2}) \langle \sigma v \rangle_{DT} r \tag{3.129}$$

where n'_{He} refers to the partial derivative with respect to r. This equation is directly integrable and integration over r with the use of eqs. (3.119), (3.120), (3.121) and (3.122) leads to:

$$\begin{aligned} -r n'_{He} \approx & \frac{n_{e0} C_0 k T_0^2}{2D} \{ \frac{n_{e0} a^2}{4(2\alpha_e + 2\alpha_T + 1)} [1 - (1 - \frac{r^2}{a^2})^{2\alpha_e + 2\alpha_T + 1}] \\ & - \frac{n_{\alpha 0} a^2}{(\alpha_e + \alpha_{He} + 2\alpha_T + 1)} [1 - (1 - \frac{r^2}{a^2})^{\alpha_e + \alpha_{He} + 2\alpha_T + 1}] \\ & - \frac{n_{i0} Z_i a^2}{2(\alpha_e + \alpha_{i0} + 2\alpha_T + 1)} [1 - (1 - \frac{r^2}{a^2})^{\alpha_e + \alpha_{i0} + 2\alpha_T + 1}] \} \end{aligned} \tag{3.130}$$

From eq. (3.121) the left-hand side of this equation can be differentiated, to give:

$$n'_{He} = -\frac{2 r n_{\alpha 0} \alpha_{He}}{a^2} (1 - \frac{r^2}{a^2})^{\alpha_{He} - 1} \tag{3.131}$$

and after binomial series expansion of both sides, and keeping only terms of the lowest power of r (r^2), we find:

$$\alpha_{He} = \frac{n_{e0} a^2 C_0 k T_0^2}{4D} [\frac{1 - 2f_0 - f_i Z_i}{4 f_0}] \tag{3.132}$$

with $f_0 = \frac{n_{\alpha 0}}{n_{DT}}$ ($n_{DT} = 2n$) the central helium concentration and $f_i = \frac{n_{i0}}{n_{DT}}$ the central impurity concentration.

Here only the particle transport using Fick's law was considered. In reality the heat and particle transport are coupled and this problem will be addressed in section 3.6.6.

3.6.4 Heat-flow equations

In the same manner the heat-diffusion equation can be written:

$$\begin{aligned} \frac{3}{2}\frac{1}{r}\frac{\partial}{\partial r}(-r\chi\frac{\partial n_{tot}kT(r)}{\partial r}) &= n^2\langle\sigma v\rangle_{DT}E_\alpha - P_{Brems} - P_{Rad} - P_{Recombination} \\ &- P_{Cyclotron} - P_{CXneutrals} \end{aligned} \tag{3.133}$$

We simplify the problem by considering only bremsstrahlung, and neglect the contributions from the other energy loss terms. This makes the analysis only applicable to low Z impurities (line radiation becomes important for higher Z ($Z > 6$) impurities), with a view to carbon being the choice of plasma-facing material for ITER [COH90]), and we also limit the plasma temperature to < 30 keV due to the limitation set by neglecting cyclotron radiation. In the central regions of the plasma the contributions from recombination and charge exchange losses are generally small for low Z impurities.

The bremsstrahlung power loss is expressed by eq. (3.9) and this expression is substituted into eq. (3.133) to yield:

$$\frac{\partial}{\partial r}(-r\frac{\partial n_{tot}kT(r)}{\partial r}) = \frac{2r}{3\chi}\{E_\alpha[\frac{n_e^2}{4} - n_e n_{He} - \frac{n_e n_i Z_i}{2}]\langle\sigma v\rangle_{DT} - P_{Brems}\} \tag{3.134}$$

The impurity density is assumed constant inside r_0 [ENG78], and integration over r with substitutions from eqs. (3.119), (3.120) and (3.121) gives:

$$\begin{aligned} -r\frac{\partial n_{tot}kT(r)}{\partial r} &= \frac{2}{3\chi}\{E_\alpha n_{e0}C_0kT_0^2[\frac{n_{e0}a^2}{8(2\alpha_e + 2\alpha_T + 1)}[1 - (1 - \frac{r^2}{a^2})^{2\alpha_e+2\alpha_T+1}] \\ &- \frac{n_{\alpha 0}a^2}{2(\alpha_e + \alpha_{He} + 2\alpha_T + 1)}[1 - (1 - \frac{r^2}{a^2})^{\alpha_e+\alpha_{He}+2\alpha_T+1}] \end{aligned}$$

$$
\begin{aligned}
&- \frac{n_{i0}Z_i a^2}{4(\alpha_e + 2\alpha_T + 1)}[1 - (1 - \frac{r^2}{a^2})^{\alpha_e + +2\alpha_T + 1}]] \\
&- \frac{K_1\sqrt{kT_0}n_{eo}}{2}[\frac{n_{e0}a^2}{2\alpha_e + \frac{\alpha_T}{2} + 1}[1 - (1 - \frac{r^2}{a^2})^{2\alpha_e + \frac{\alpha_T}{2} + 1}] \\
&+ \frac{2n_{\alpha 0}a^2}{\alpha_e + \alpha_{He} + \frac{\alpha_T}{2} + 1}[1 - (1 - \frac{r^2}{a^2})^{\alpha_e + \alpha_{He} + \frac{\alpha_T}{2} + 1}] \\
&+ \frac{n_{i0}Z_i(Z_i - 1)a^2}{(\alpha_e + \frac{\alpha_T}{2} + 1)}[1 - (1 - \frac{r^2}{a^2})^{\alpha_e + + \frac{\alpha_T}{2} + 1}]]\}
\end{aligned} \tag{3.135}
$$

where $K_1 = 3.842 \cdot 10^{-29}\ \sqrt{\text{J}}\ \text{m}^3$. From L-mode results it is known that the electrons transport most of the energy away from the plasma [COP80A], leading to:

$$n_{tot} \approx n_e$$

We can now differentiate $n_{tot}T(r)$ to find

$$
-r\frac{\partial n_{tot}kT(r)}{\partial r} = \frac{r^2 kT_0}{a^2}\{2n_{e0}(\alpha_e + \alpha_T)(1 - \frac{r^2}{a^2})^{\alpha_e + \alpha_T - 1}\} \tag{3.136}
$$

After series expansions of both sides of eq. (3.134), using eq. (3.136) and equating the lowest order terms in r on both sides, we find:

$$
\begin{aligned}
\alpha_T \approx\ & \frac{a^2 n_{e0}}{3\chi}\{\frac{E_\alpha C kT_0}{8}(1 - \frac{4f_0}{fpre} - \frac{2f_{i0}Z_i}{fpre}) \\
&- \frac{K_1}{2\sqrt{kT_0}}[1 + \frac{2f_0}{f_{pre}} + \frac{f_{i0}Z_i(Z_i - 1)}{fpre}]\} - \alpha_e\}
\end{aligned} \tag{3.137}
$$

with $f_{pre} = 1 + 2f_0 + f_{i0}Z_i$.

We assume that the electron density profile (i.e. n_{e0} and α_e) is controllable by external methods, and therefore fixed.

We now have two equations (3.132), (3.137) linking the parameters α_{He} and α_T. These two equations were used to study the profile coefficients of helium density and temperature as a function of plasma temperature, and the results are indicated in Fig. 3.20. It is clear that for this set of plasma parameters the temperature profile peakedness has a maximum for an operating temperature of about 25 keV, and it also shows the broadening of the profile, for higher plasma temperatures. The two sets of curves are for $\chi = 0.4\ \text{m}^2/\text{s}$ and $\chi = 0.8\ \text{m}^2/\text{s}$. The profile coefficients

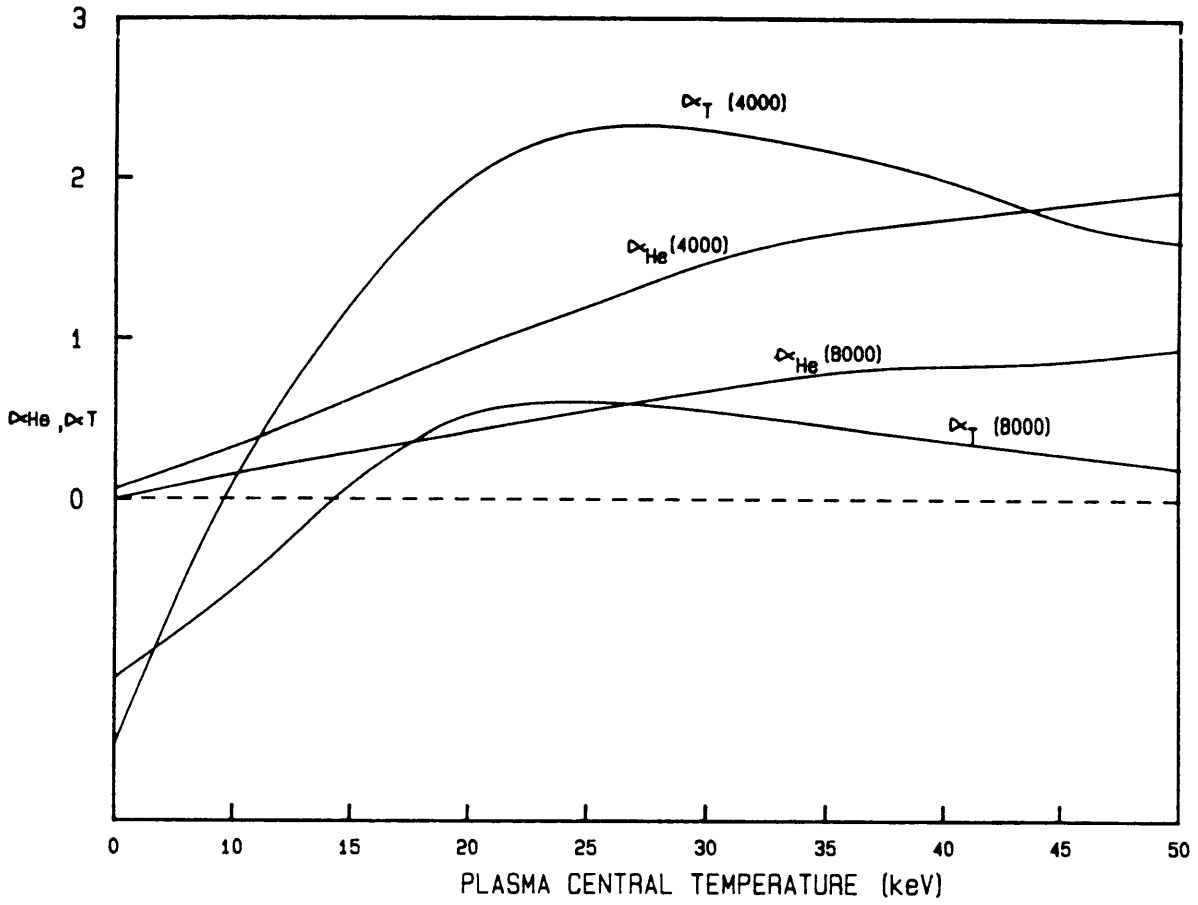

Figure 3.20: **Profile coefficients of helium and temperature as a function of plasma temperature. The two sets of curves are for $\chi = 0.4$ m^2/s and $\chi = 0.8$ m^2/s.**

are also correspondingly lower for the larger energy diffusivity, i.e. the temperature profile is less peaked, which is to be expected. The effect of a change in χ on the temperature profile coefficient is also stronger than for the helium density profile coefficient. A fixed ratio of $\frac{\chi}{D} = 2$ was assumed for these calculations. The omission of cyclotron radiation limits the validity of the results to ≤ 30 keV.

3.6.5 Burn and exhaust criterion

An alternative interpretation of the previous analysis can be made by looking at the form of eqs. (3.132) and (3.137). The expressions are similar to the global expressions derived for the burn and exhaust criterion by [BEH90A] and [REI90], and from these equations one can get an expression for the ratio $\frac{\chi}{D}$. This result can be compared for chosen values of α_T and α_{He}, for the zero-dimensional analysis, the addition of profiles to the model, and this, the one-dimensional analysis. The latter analysis predicts:

$$\frac{\tau_{He}}{\tau_E} \approx \tag{3.138}$$

$$\frac{\chi}{D} = \frac{16 f_0 \alpha_{He}}{3 C_0 k T_0^2 (1 - 2f_0 - f_{i0} Z_i} \cdot \frac{\frac{E_\alpha C_0 k T_0}{8}(1 - \frac{4 f_0}{f pre} - \frac{2 f_{i0} Z_i}{f pre}) - \frac{K_1}{2\sqrt{k T_0}}[1 + \frac{2 f_0}{f pre} + \frac{f_{i0} Z_i (Z_i - 1)}{f pre}]}{(\alpha_T + \alpha_e)} \tag{3.139}$$

Results for this expression as a function of plasma temperature are indicated in Fig. 3.21 for different plasma parameters. In this figure the values obtained for the cases of no impurity and with 2 % carbon in the plasma are shown and compared to the same parameters for the zero-dimensional model, and the zero-dimensional model with profile effects included. It is clear from the ratios of χ/D found with the three models that they compare very well, especially for the case of no impurities. For the case of carbon present, the one-dimensional model is the most stringent with a maximum of ~ 4, compared to the ~ 7 and ~ 6.5 for the volume averaged and the global zero-dimensional model.

The comparison between the models shows that it is at least useful to use the one-dimensional approach, be it with many assumptions, to obtain the profile behaviour of helium density and temperature, yielding results similar to a global zero-dimensional analysis. In the one-dimensional approach the advantage is situated in the coupling of the profile coefficients and the diffusion coefficients of energy and helium.

The results of this approximation are compared to the exact solutions in the next section, obtained by solving the one-dimensional diffusion equations for helium and energy transport.

3.6.6 Exact solution

The one-dimensional energy diffusion equations can be written in the form:

$$\frac{1}{r}\frac{\partial}{\partial r}[-r n_e \chi \frac{\partial k T}{\partial r}] = S_T(r) \tag{3.140}$$

where $S_T(r)$ is the source term for energy and is written as:

$$S_T(r) = E_\alpha [\frac{n_e^2}{4} - n_e n_{He} - \frac{n_e n_i Z_i}{2}] \langle \sigma v \rangle_{DT} - P_{Brems} \tag{3.141}$$

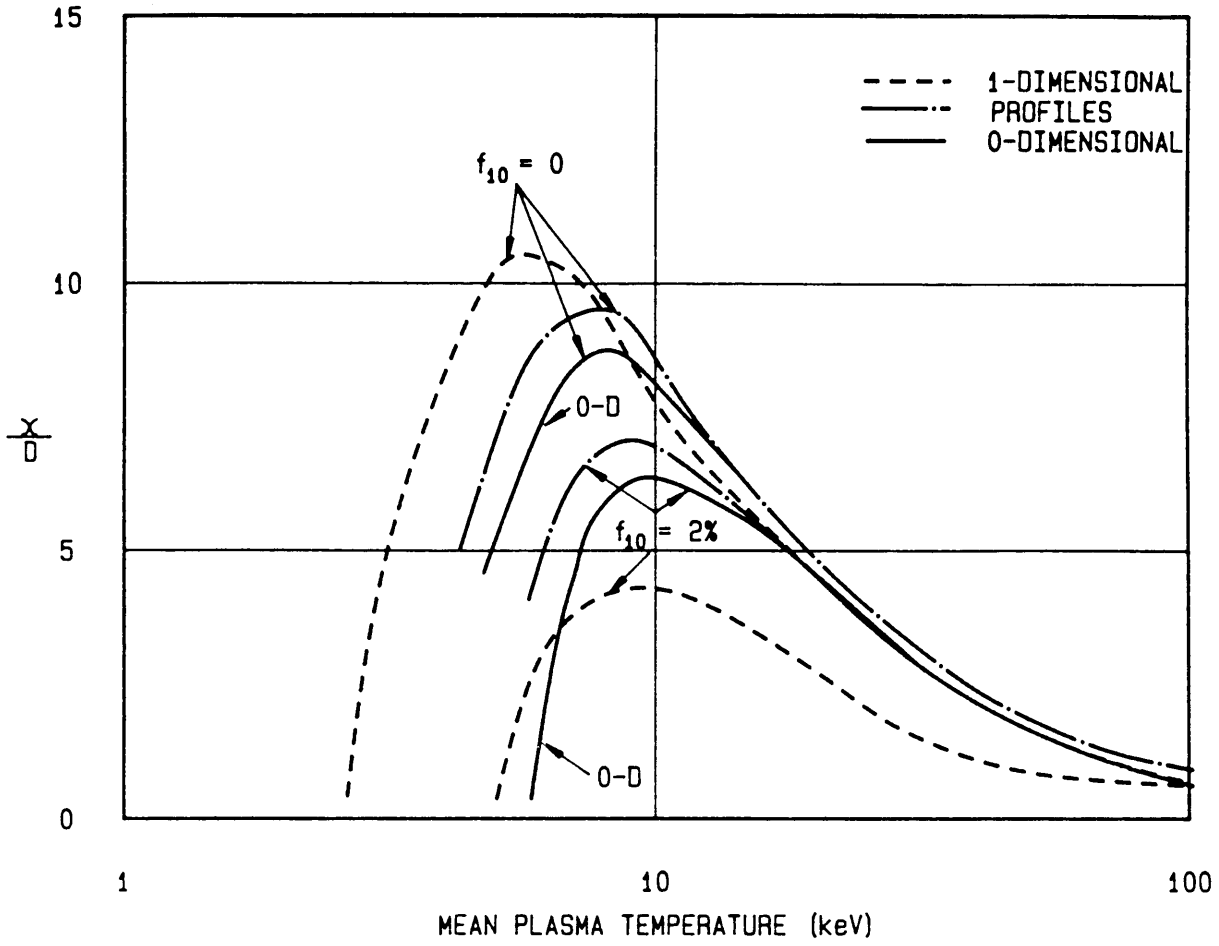

Figure 3.21: **Ratio of helium to energy confinement time for different plasma parameters. The values obtained for the cases of no impurity and with 2 % carbon in the plasma are shown and compared for the same parameters for the zero-dimensional model, and the the zero-dimensional model with profile effects included.**

The neo-classical energy diffusivity χ, which is the most reliable quantification for the diffusivity for reactor conditions, can be expressed as the following function of the small radius r [RED89]:

$$\chi = \chi_{e0}(3 + \frac{5r}{a}) \tag{3.142}$$

and together with the usual assumption with respect to the profile for the electron density (see eq. (3.119)), we can write the second order diffusion equation as follows:

$$\frac{\partial^2 kT}{\partial r^2} = \frac{1}{rn_e\chi}\{-\frac{\partial kT}{\partial r}[n_e\chi - \frac{2n_{e0}\chi\alpha_e r^2}{a^2}(1 - \frac{r^2}{a^2})^{(\alpha_e-1)} + \frac{5rn_e\chi_{e0}}{a}] - rS_T(r) \tag{3.143}$$

In the same way the diffusion equation (see also eq. (3.129)) for helium, including the inward pinch term $v_\perp$(r), can be written in one dimension, as follows:

$$\frac{1}{r}\frac{\partial}{\partial r}r[-D\frac{\partial n_{He}}{\partial r} + v_\perp(r)n_{He}] = S_N(r) \tag{3.144}$$

where $S_N(r)$ is the source term for the helium and is written as:

$$S_N(r) = [\frac{n_e^2}{4} - n_e n_{He} - \frac{n_e n_i Z_i}{2}]\langle\sigma v\rangle_{DT} \tag{3.145}$$

This equation can be written in the form:

$$\frac{\partial^2 n_{He}}{\partial r^2} = \frac{1}{rD}\{-\frac{\partial n_{He}}{\partial r}[D + \frac{5\chi_{e0}r}{2a} + \frac{0.2Dr^2}{a^2}] \tag{3.146}$$

$$+ n_{He}[\frac{0.1\chi_{e0}}{a^2}(\frac{10r}{a} + 3) - v_\perp] - rS_N(r) \tag{3.147}$$

with the particle diffusion coefficient D linked to the energy diffusivity χ by [RED89]:

$$D = \frac{\chi_{e0}}{\xi}(3 + \frac{5r}{a}) \tag{3.148}$$

and the pinch velocity described by [STA90]:

$$v_\perp = -0.2\frac{Dr}{a^2} \tag{3.149}$$

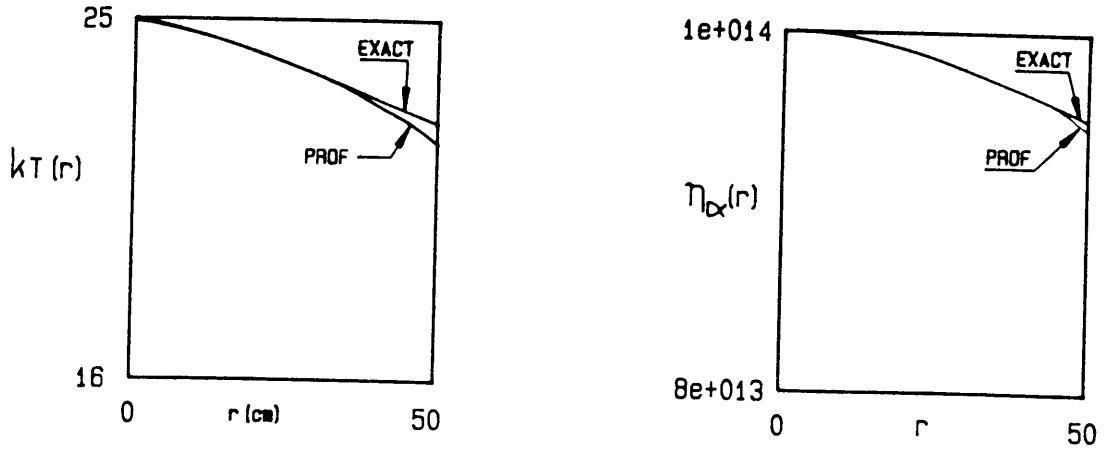

Figure 3.22: **The resulting functions for $n_{He}(r)$ and $kT(r)$ compared with the approximate solutions obtained**

These two expressions (3.143) and (3.147), which are two coupled second-order differential equations were solved numerically using the Runge - Kutta method. The equations were solved with boundary conditions set at the plasma centre ($r = 0$), i.e. $\frac{\partial n_{He}(0)}{\partial r} = \frac{\partial kT(r)}{\partial r} = 0$ and different central values of n_{He} and kT.

The resulting functions for $n_{He}(r)$ and $kT(r)$ were then compared with the approximate solutions obtained with the method described earlier. To compare the resulting profiles with the profiles obtained with the approximate method, the exact solutions obtained were fitted to profiles like those described by eqs. (3.119) and (3.120). Typical results are shown in Fig. 3.22. It is clear that these types of fits are only valid at the central parts of the plasma volume, i.e. approximately to $\frac{r}{a} \approx 0.5$. It is in this volume where the fusion process is concentrated, and the fit was used to assign profile parameters α_T and α_{He} to the temperature and helium functions. These parameters were compared to the profile parameters obtained with the approximate model in Fig. 3.23 (a) and (b).

From this figure it is clear that the qualitative behaviour of the exact and the approximate solutions are similar, with limited quantitative interpretation. The

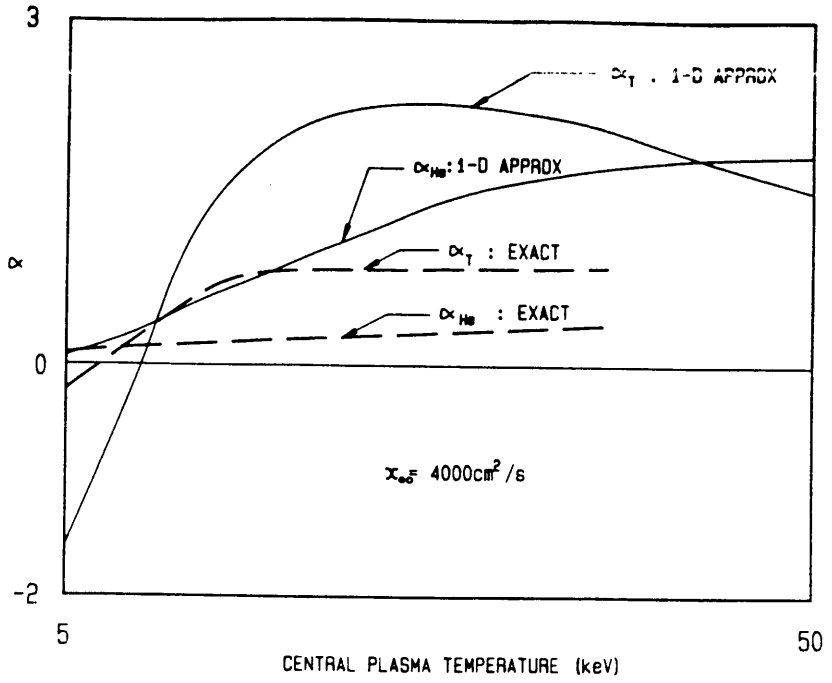

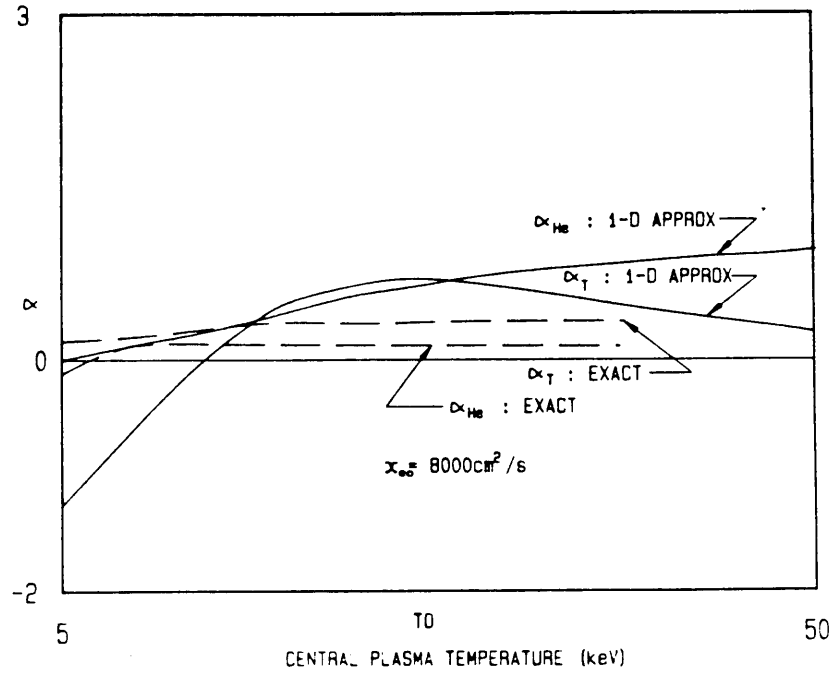

Figure 3.23: **The profile parameters for temperature and helium compared to the profile parameters obtained with the approximate model. In (a) the value of χ= 0.8 m^2/s was used and in (b) the value of χ= 0.4 m^2/s was used to obtain the results.**

calculations were made for the two values of $\chi_{e0} = 0.4$ and $0.8\ m^2s^{-1}$. A value for $\xi = 2$ was assumed in both these cases.

With the answers qualitatively corresponding to a more rigorous analysis, the approximate method does describe a quick way of determining dependencies of the profiles of density and temperature on the various plasma parameters, especially D and χ.

Chapter 4

Time-resolved measurements of erosion and deposition in the scrape off layer (SOL) of JET

The processes of erosion and deposition at the limiters in tokamaks during different phases of a discharge are very dependent on not only the edge plasma processes, but also the central plasma parameters, rendering the process very complicated. These processes furthermore contribute to a large extent to the impurity content in the plasma as limiter material and deposits on the limiter are sputtered away, and the impurities have a probability to enter the plasma and contribute to radiative cooling or dilution of the plasma. During the discharge these impurities can also be deposited at different places in the torus, leading to a nett erosion or deposition profile at the walls and limiter face.

Several models exist, e.g. [MCC87,MCC89,STA88,BRO83,PIT88], to explain and simulate these processes, all with some success. The general considerations of models to explain the erosion and deposition processes in a tokamak are generally capable of explaining these profiles as measured on samples exposed for long times or on limiter tiles. These targets have, however, been subjected to a large amount of very different discharges, disruptions and conditionings, which limits the interpretation of results.

One model [MCC87,MCC89] predicts the erosion and deposition profile and compares well to the erosion and deposition measured for the campaign of JET where discrete carbon limiters were used in the machine. This campaign led to high nett erosion of the limiters close to the last closed flux surface (LCFS), corresponding with the assumption of the model that the plasma density at the edge was low, leading to insignificant ionisation of eroded particles in the SOL.

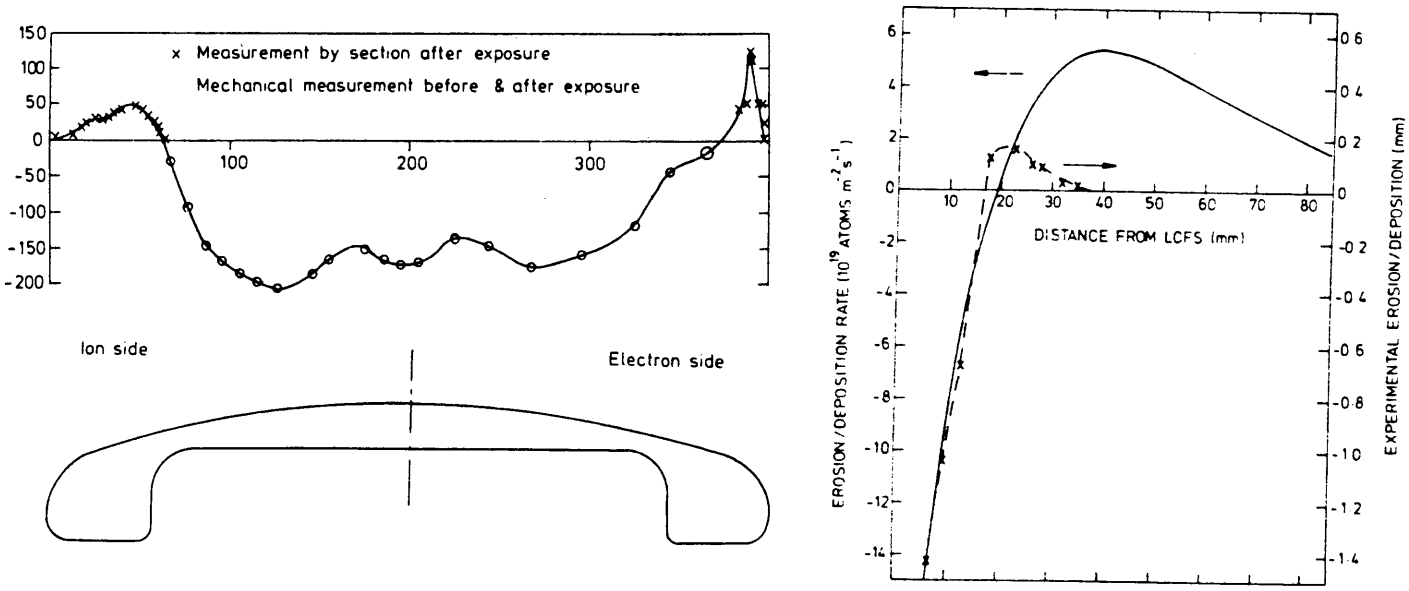

Figure 4.1: **Results of the model with negligible ionisation in the SOL**

The bulk of the particles therefore enter the plasma before they are ionised, and leave the plasma by diffusion across magnetic field lines. The general profile is then one of large nett erosion at the points closest to the plasma, which changes to nett deposition at points further than the e - folding length from the plasma where there is little erosion due to the low density and temperatures, and there is a source of particles sputtered from other areas of higher erosion in the SOL. The result of the model and the measured profiles are indicated in Fig. 4.1 [MCC87].

A second model [STA88], a Monte Carlo simulation, simulates the various processes influencing the transport of eroded particles in the SOL. This model incorporates the probability that particles may be ionised in the SOL with the result that in high density dischargs, the probability of ionisation is very high close to the last closed flux surface, and therfore particles eroded from the points closest to the plasma (the tangential point with high local density) are ionised quickly, and redeposited close to the position of erosion. This leads to nett deposition at the latter positions, followed by nett erosion at positions further out. At the positions furthest from the plasma the situation is not very different from the considerations of the first model, and at these positions there is nett deposition. The results of this model and measurements obtained from the belt limiter tiles used in operation of JET are shown in Fig. 4.2.

A lot of experimental work have previously been done [BEH89A,MCC87,MCC89] on limiters and limiter-like probes in JET to get positional deposition and erosion

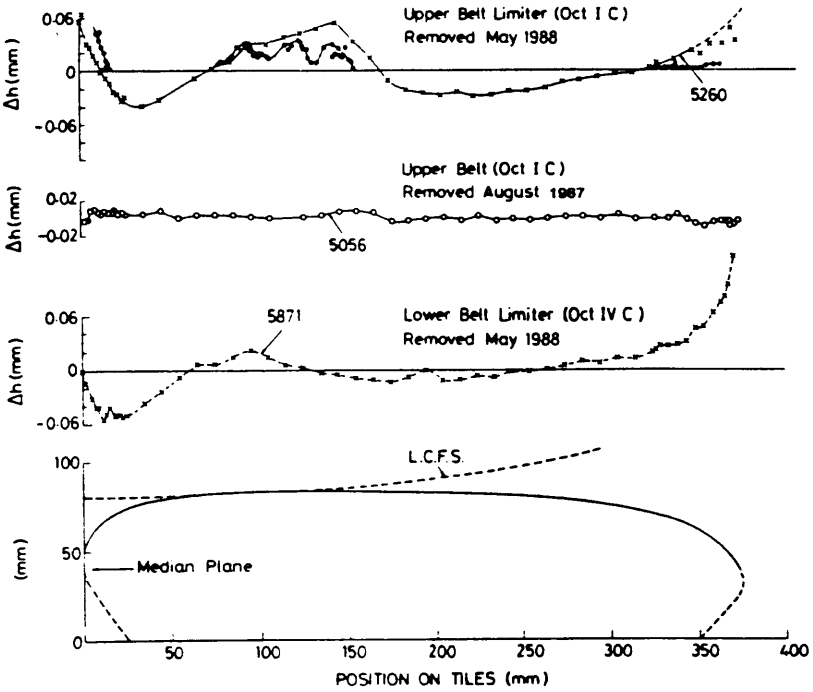

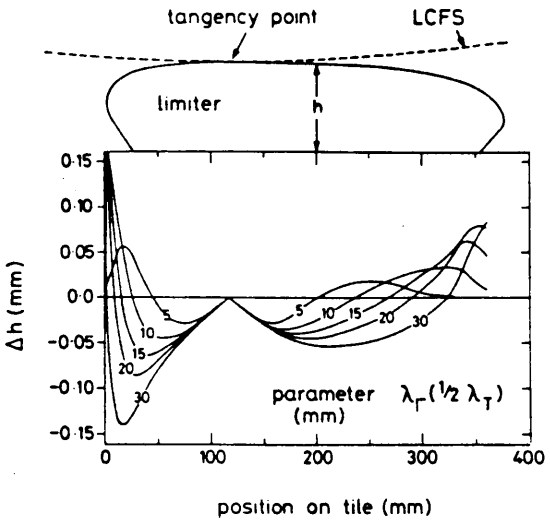

Figure 4.2: **Results of a model with significant ionisation in the SOL**

profiles of deuterium and metal impurities.

Up till now, however, there has been no detailed study on the time-resolved process of erosion and deposition at the limiters, especially during a single discharge. These measurements endeavoured to broaden the knowledge of these processes for the JET tokamak, which is of particular importance as this tokamak is the machine that lends itself to extrapolation of results into the NET and ITER regimes, although still with considerable uncertainties.

The well-known method of studying these processes is to insert probes into the SOL of JET for discharges with different parameters. The probes are then exposed to deposition and erosion mechanisms in the SOL, and is subsequently analysed by ion beam techniques. During a previous analysis [BEH89A] it became apparent that the different phases of the discharge (i.e. the current ramp-up, flat top and current ramp-down) contribute to different erosion and deposition phenomena. It was deduced from these measurements that the current ramp-up phase should be responsible for nett erosion, especially close to the plasma, and that deposition dominated through the flat top/current ramp-down phase of the discharge.

These phenomena were deduced from the disappearence of a pre-implanted ^{13}C marker at a well-defined depth used to define the original surface. This marker was eroded away close to the plasma during the discharge, although the end result was nett deposition on the probe. Another possibility was that the temperature of the probes, which was not measured, became high enough for the ^{13}C to diffuse from the probes.

Results indicated that in general there was nett deposition in the region close to the last closed magnetic surface, which changed to nett erosion of the surface further away from the plasma. The region furthest from the plasma in general suffered nett deposition again.

4.1 Experimental considerations

In the current study probes were exposed to different phases of the same discharge to study the time dependence of erosion and deposition in a single discharge as well as its radial dependence outside the plasma. The probes were mounted on the fast transfer system in JET. This system allowed the short exposure of samples during a discharge with a quick target-moving facility, by means of which different samples could be introduced into the plasma during the course of the discharge.

These measurements were therefore undertaken to resolve the uncertainties attached to the erosion and deposition phenomena. This is of interest to the designers of

future machines, as knowledge of erosion and deposition processes during different stages of a discharge may well influence operating parameters. Five carbon samples were prepared to be exposed to a high-density, high-current exposure with auxiliary heating.

To study erosion phenomena the targets were implanted with 20 keV molybdenum implants, amounting to $5 \cdot 10^{16}$ atoms per cm^2. The implantation was done at the Technical University in Munich, and the implants were checked with Rutherford backscattering (RBS) measurements, where the expected depth of the molybdenum of 150 angstrom was confirmed. The sputtering yield due to implantation at this energy is of the order of 1, and the reflection is < 0.01 [LAN84].

Molybdenum was chosen in favour of the commonly used ^{13}C as a marker in erosion studies, and was based on evidence [SOD88] that ^{13}C tends to drift in samples which are heated to high temperatures ($> 1\ 000\ ^0C$). These temperatures are locally attainable [BER90] during exposure to the discharge close to the plasma column. In the same measurements it was shown that molybdenum was much more stable under the same circumstances. Another disadvantage of the use of ^{13}C is the analysis of the marker, which in this case is made using of secondary ion mass spectroscopy (SIMS), where it has been shown that the sputtering process is not homogeneous with depth. This was verified by studying SIMS sputtering craters with an electron microscope, where the irregular features of the sputtered surface could easily be seen [BEH90], which degraded the obtainable depth resolution.

A bonus was found in that there was sulphur contamination of the targets introduced during the polishing of the targets. This contamination was therefore situated at the original surface of the sample. The depth of the molybdenum implants was not adequate, as deeper erosion was expected at some positions on the probe than the depth of the implant. However, at this time this was the highest energy available for the implants to be made. For future studies target implants of > 200 keV should be made with a projected range of about 900 angstroms. At this energy, however, straggling (> 150 angstroms) during the implantation process will start to play a role, and will limit the depth information that can be gained from these experiments.

The analysis of the molybdenum was made with RBS, which is ideally suited for analysis of a heavy marker in a light substrate, and information on the depth of the implant could easily be extracted. The correct energy calibration of multichannel spectral data in such a case is extremely important to obtain precision results, and as aid a pure molybdenum foil was always simultaneously analysed, as well as a pure alluminium foil on the target mounting. A third point in the calibration data was taken from the carbon edge in the RBS spectrum of the probes.

4.2 Results of pre-exposure experiments

In addition to the erosion and deposition of carbon during the discharge, the deposition of other elements was also studied. The heavy impurities from the plasma, eg. the wall material: iron, nickel and chromium were measured with particle induced X - ray emission (PIXE), and the deposition of beryllium, the result of beryllium evaporation [THO90] in the plasma chamber of JET, was studied with proton enhanced scattering (PES) at a proton energy of 350 keV, which was shown [REI89] to be a sensitive method to measure beryllium on carbon. The deposition of beryllium as a function of radial position was measured.

PIXE is a standard technique for materials analysis by detecting the element-specific X-rays from the different constituents in a sample. The yields for the different heavy elements analysed were compared to calibration measurements performed with standard targets to obtain the areal density.

The PIXE measurements were made with a 1.5 MeV proton beam which has a range of about 10 μm in carbon, indicating the depths reachable in probe analyses. The deposits, however, only occupied the top $\sim$ 1 μm of the probe, allowing the use of thin target assumptions for the PIXE analyses.

The analysis of the deuterium content after exposure was made with nuclear reaction analysis (NRA) measurements using the ^{3}He(d,p)^{4}He reaction. The high energy release of the reaction allows the measurement of either the resulting protons or ^{4}He. The protons ($\sim$ 14 MeV) were measured after passing through a thick absorber foil which stopped all other particles, giving a clean spectrum of the reaction protons. This removed the possibility of doing depth profiling of deuterium, which was not needed for this study.

The ^{3}He beam energy used for this reaction was 790 keV due to the resonance character of the cross section at this energy. This means that these samples were analysed to a total depth of $\sim$ 2 μm. Checks were made to ensure that the full deuterium layer was measured by control measurements with the D(d,p)T reaction where the impinging deuterons have a deeper ($\sim$ 5 μm) penetration. With the ^{3}He measurements care had to be taken to avoid bombardment induced emission of the deuterium, and although relatively high fluxes ($\sim 10^{14}$ ions) were necessary to obtain sufficient yield using this reaction, control measurements showed no decrease in the measured amount of deuterium.

Hydrogen was measured with elastic recoil detection (ERD) with ^{4}He, the reaction being H(^{4}He,H)^{4}He. The analysis was done at a glancing angle of 30°, with an incoming ^{4}He energy of 2.6 MeV. The pre-exposed hydrogen content at the surface of the sample was of the order of 10^{17} atoms/cm^2, which is normal for polished

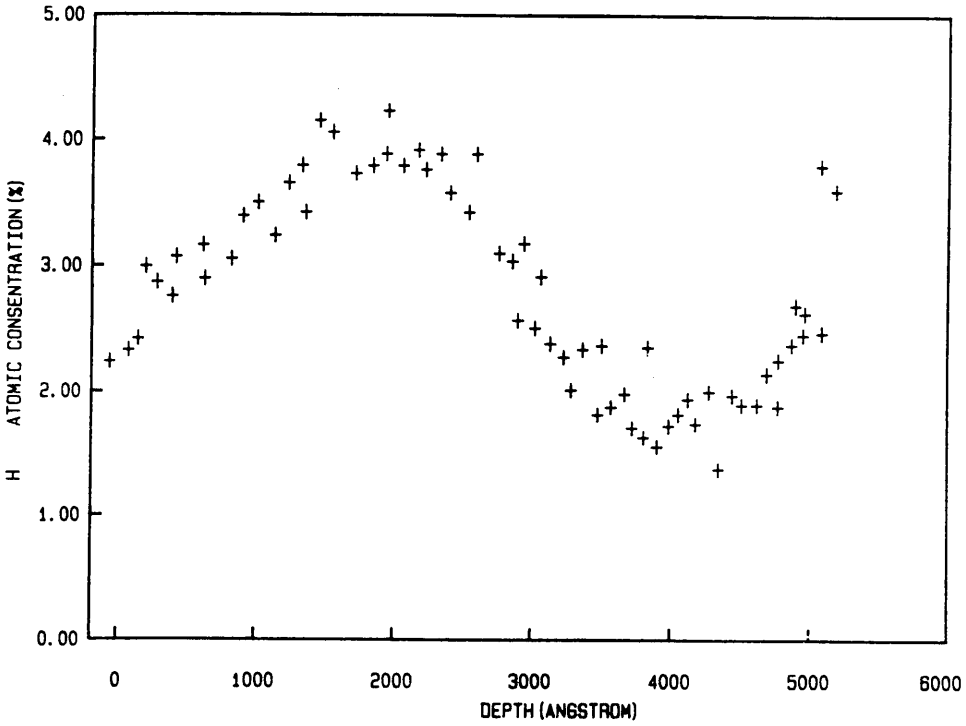

Figure 4.3: **The hydrogen depth profile in a pre - exposed sample implanted with molybdenum**

carbon (see section 5), although the depth profile shown in Fig. 4.3 showed some irregularities, probably caused during the molybdenum implantation.

The results of the RBS measurements of pre-exposed samples are shown in Fig. 4.4 and indicate the presence of molybdenum and sulphur. The depth profile of the molybdenum implant is shown in Fig. 4.5, showing the peak depth of 150 $\mathring{A}$. The sulphur contamination was found to be situated at the surface, which was considered ideal to check for initial erosion at all positions.

4.3 Experimental results

The main constraint in mounting and demounting the samples was the fact that there was some beryllium on the probes due to the exposure in the beryllium evaporated JET vessel. For safety purposes probe mounting had thus to be made in a controlled atmosphere.

The targets were subsequently exposed in the plasma of JET and analysed in the ion beam analysis laboratory at Garching.

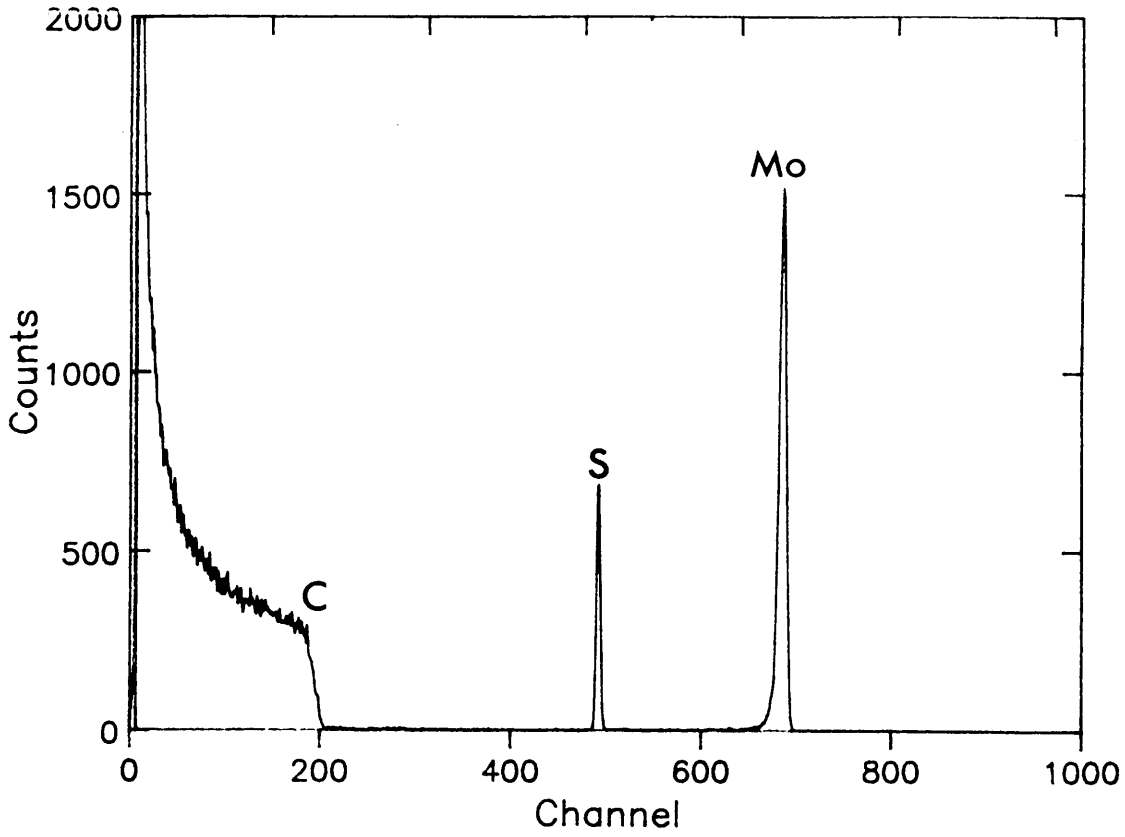

Figure 4.4: **RBS spectrum of pre-exposed samples with molybdenum implant**

Four of the five targets were exposed to the different phases of discharge #20 924 at JET. During the flat-top phase neutral beam injection was added for heating purposes. The tips of the probes were 10 cm from the last closed flux surface during the discharge.

The fifth probe was exposed to a similar discharge (# 20 925) for the whole duration of the discharge, to study the overall nett effect of the different phases of the discharge, with the discharge ending in a disruption.

The results of the metal content analysis from PIXE measurements did not show any significant behaviour, and the small changes across the probe face probably indicate pre-exposure contamination.

The only significant trend is for the iron, where the separate time intervals of the discharge show a slight decrease as a function of increasing radius, whereas the target exposed to the full discharge shows an inverse effect, even though the addition of the amounts deposited during each individual phase of the discharge compares well with the amount deposited on the full discharge probe.

The peak depth of the marker shows deposition over the whole exposed surface of the probes, as indicated in Fig. 4.6. The results for smaller radial distances, i.e.

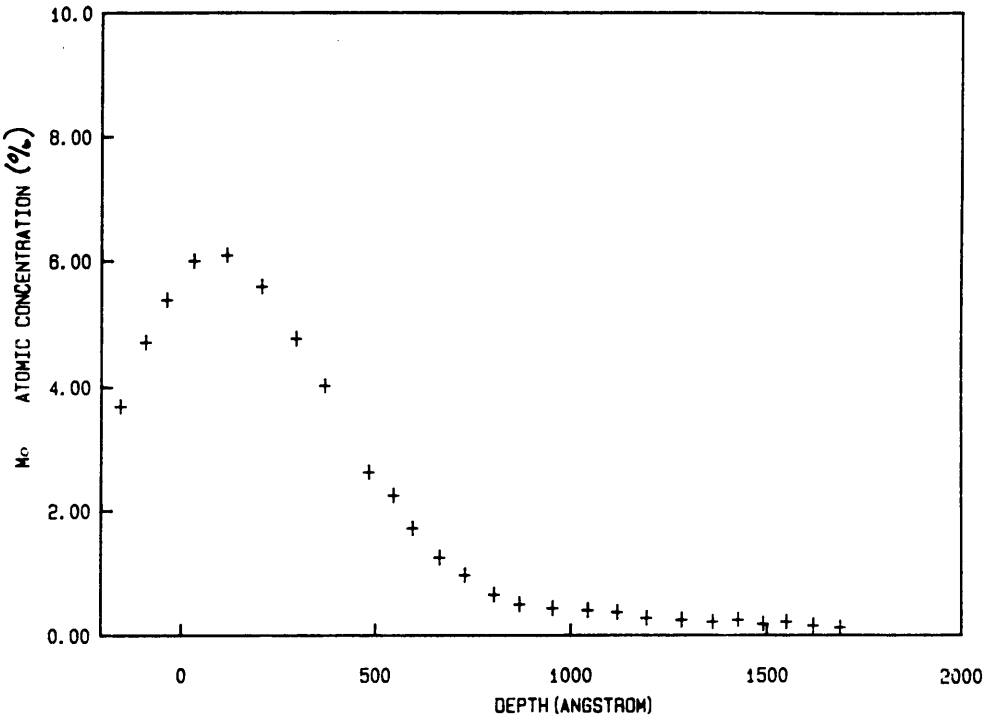

Figure 4.5: **Depth profile of molybdenum implant as obtained from the RBS measurement**

closer to the LCFS, could not be obtained, as the (visible) deposition exceeded the thickness for analysis with the ^{4}He beam used in the RBS analysis. It is, however, clear that the flat-top phase contributes the most significantly to the final deposition, especially just outside the LCFS, where it is at least an order of magnitude larger than for the other intervals studied. The sum of the contributions does not add up to the total deposition of the probe exposed to the whole discharge, and may be attributed to the disruptive ending of discharge # 20 925. The probe exposed to the full discharge generally had $\sim$ 5 times thicker deposition on the probe compared to the sum of the other probes exposed to the previous discharge.

The e-folding lengths deduced from the deposited fluxes are; ramp - up: $\sim$ 25 cm, flat top: $\sim$ 10 cm, ramp down: $>$ 40 cm and the full shot: $\sim$ 12 cm. The ramp-down value probably does not represent a true e-folding length as it contains information regarding the density profile being destroyed at the disruptive ending of the discharge. The sulphur contamination could not be detected after exposure, and was probably desorbed due to the heat load on the probe surfaces.

The beryllium deposition profile is shown in Fig. 4.7. The deposition shows no conclusive trend with increasing radius, except in the case of the full shot. In this case the same trend is seen as for the deposition profile during the ramp-down

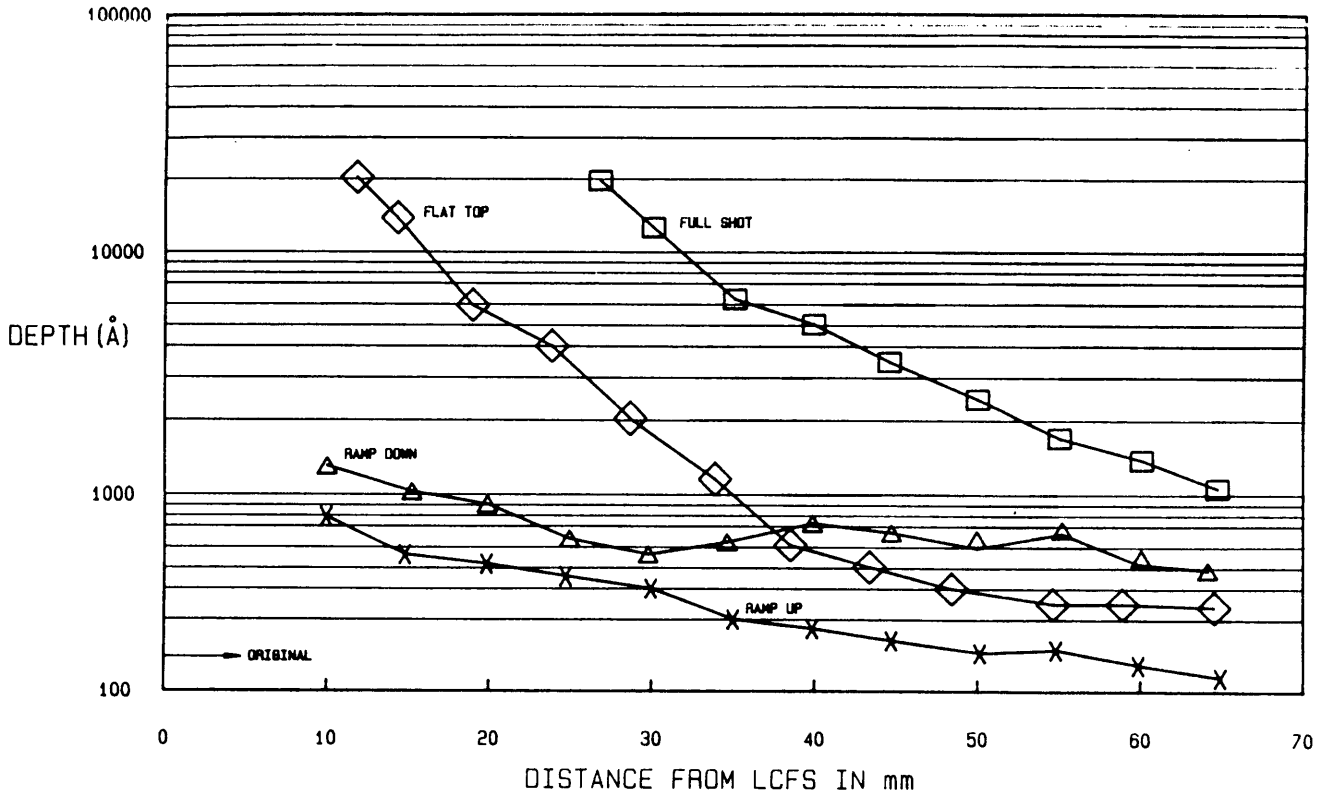

Figure 4.6: **The thickness of the deposition on the probes as measured from the movement of the molybdenum marker**

phase of the discharge. This may relate to the disruption, the loss of confinement and subsequent release and redeposition of beryllium from all over the tokamak surface. The e - folding length of the beryllium flux, as deduced from the full shot is estimated as $\sim$ 25 cm.

The deuterium deposition shown in Fig. 4.8 has a similar behaviour as found in an earlier study [BEH89A]. The deuterium deposition is closely coupled to the carbon redeposition, and is in this instance also in the range $\sim$ D/C : 0.1/1. The strong reduction in the deuterium deposition close to the LCFS was probably due to the desorption of deuterium from the probe after excessive heating, as well as the saturation properties of deuterium in carbon (see also section 5). The deduced e - folding lengths were found to be similar to the carbon deposition fluxes and are $\sim$ 20 cm, $\sim$ 14 cm and $\sim$ 20 cm for the ramp-up, flat-top and full-shot data respectively. The absence of data in the graph is at points where no deuterium was found on the probe surfaces.

Using the element abundances in the deposit at any position on the probe, e.g. r = r(LCFS) + 30 cm, we can estimate the flux composition at this radius. The result is shown in Table 4.1.

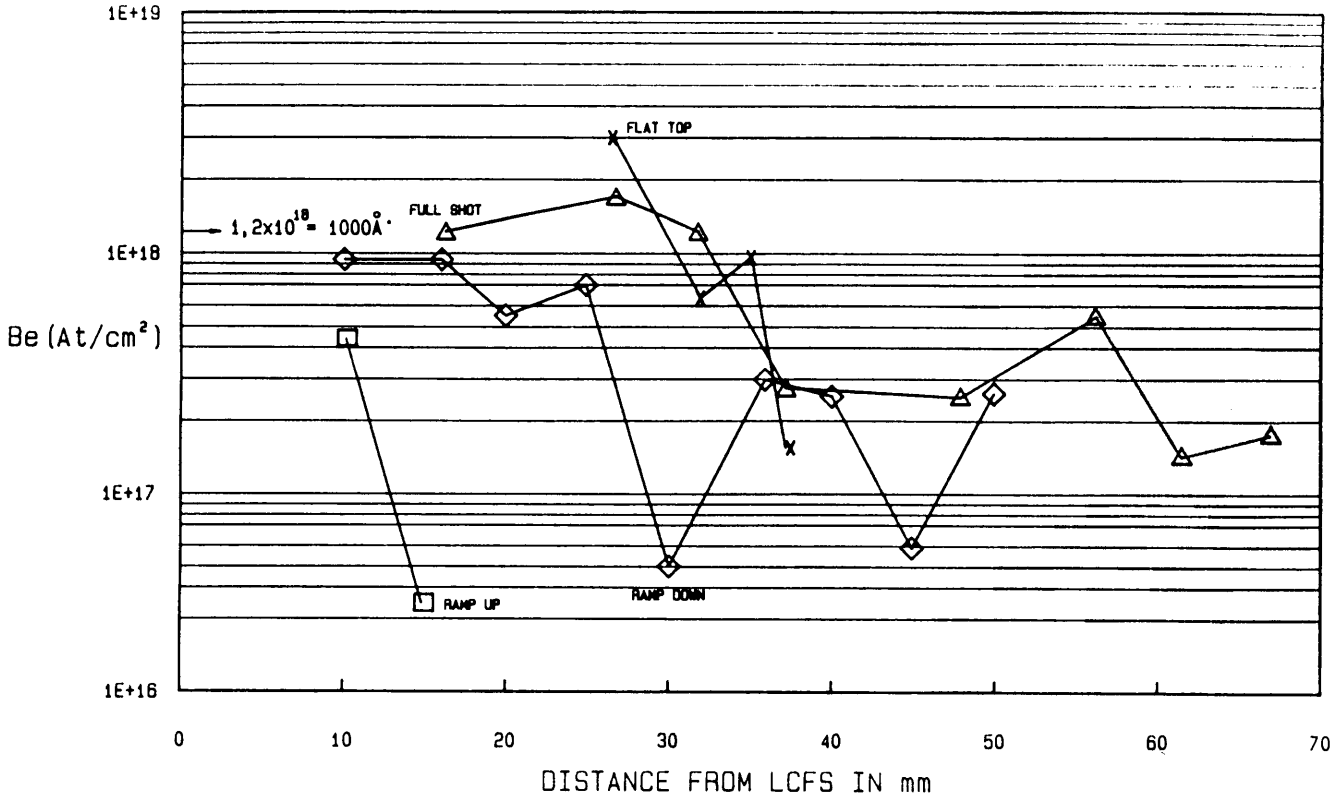

Figure 4.7: **Beryllium deposition on the probes as a function of increasing radius**

	Ramp-up	Flat-top	Ramp-down	Full-shot
Fe:Be:D:C	0.002:-:0.1:1	0.0005:1:0.3:1	0.001:0.1:0.1:1	0.0001:0.15:0.01:1

Table 4.1: **The flux composition at a distance of 30 cm outward from the LCFS**

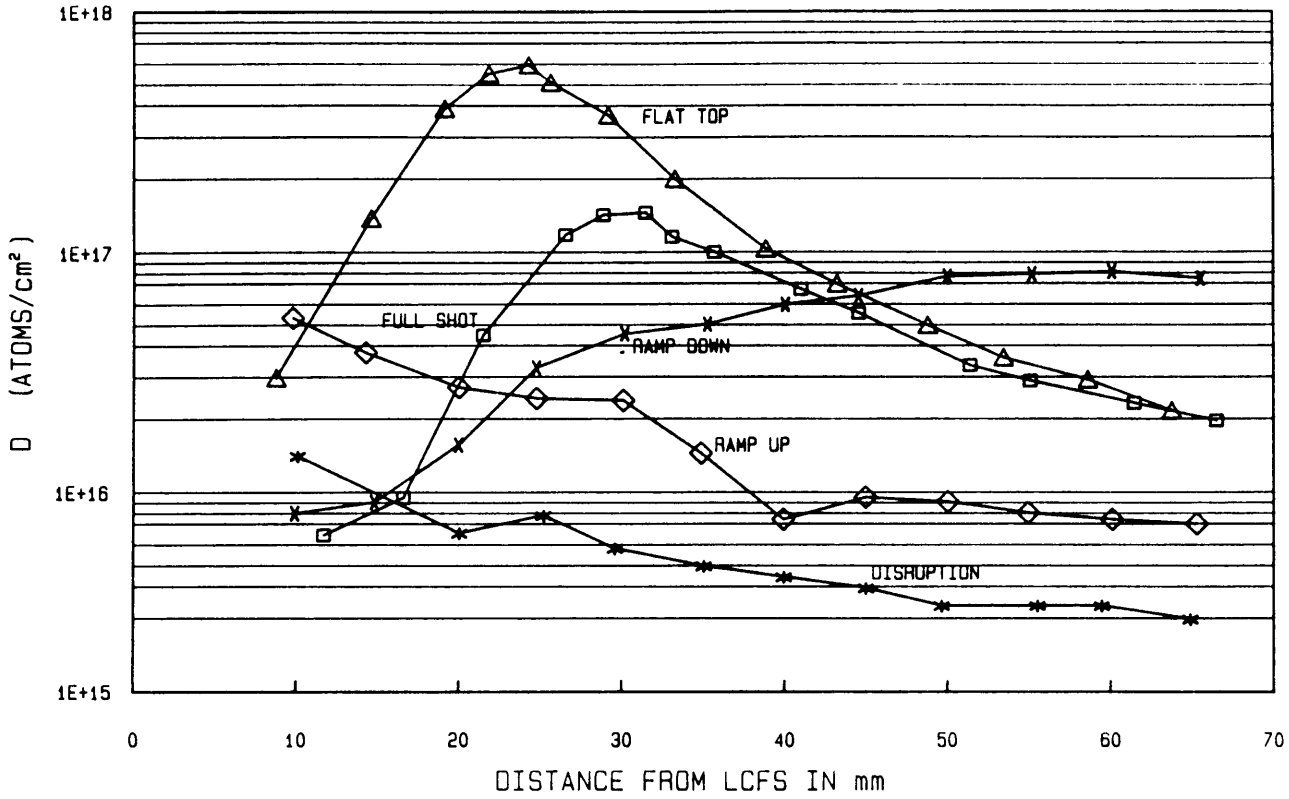

Figure 4.8: **Deuterium deposition on the probes as a function of increasing radius**

4.4 Summary

Results showed that deposition of the order of 2 μm was the dominant process, especially close to the plasma, with relatively large amounts of deuterium, beryllium and heavier metals deposited, with the deposition in general becoming less with larger radial distance. Close to the plasma sample temperatures apparently became high enough to allow deuterium and/or beryllium loss by desorption. Depth-profiling of the beryllium showed the beryllium to be distributed along the entire depth of the deposited layer.

No area of nett erosion was found and the comparison with the target exposed to the full discharge showed the flat top stage to be the most significant during the discharge with respect to deposition, which has implications for the aim of running a reactor in semi steady-state, i.e. the other stages of the discharge are short compared to the flat top stage.

The results from these measurements were not expected on the basis of the above discussion of the models of the SOL in a tokamak. The results do not show nett erosion as predicted by current SOL transport models.

Chapter 5

Measurement of fast particles in front of the ICRH antenna of ASDEX

5.1 Introduction

Ion cyclotron wave heating [STI75,CAT77] is generally achieved by launching a fast magnetosonic wave in the frequency range 10 - 200 MHz into the plasma. This is a compressional wave, and it involves mainly compression of the plasma transverse to the magnetic field. A drawback of the fast wave is that it is predominantly right-handed elliptically polarised, i.e. opposite to the direction of gyration of positively charged ions and therefore it cannot directly heat a single ion species effectively by means of fundamental ion cyclotron resonance, although kinetic effects do cause some degree of heating. The fundamental ion cyclotron frequency is given by:

$$\omega_c = \frac{|q|\,B}{m} \tag{5.1}$$

By adding a second minority ion species to the plasma an efficient heating scheme can be utilised [BRA85]. In this scheme the wave is launched at the fundamental frequency of the minority species which has a low ($\sim$ 1 %) concentration. The two species then interact to produce an ion-ion hybrid resonance at a frequency between the cyclotron frequencies of the two species, but such that the resonance layer is close to the minority cyclotron resonance layer, resulting in a strong left polarised component of the wave near this layer, which results in direct heating of the minority species. The energy of the minority species is then redistributed to the bulk of the

ions and the electrons by Coulomb collisions.

Heating of single species plasmas [WEY74,CHI83] is also possible, albeit with lower efficiency than in the two-ion regime, by means of the second harmonic of the ion cyclotron frequency ($2\omega_c$). Resonant heating of the ions near the plasma centre can be achieved with this wave heating having an appreciable left-hand polarised component.

If an ion cyclotron wave antenna is placed at the plasma edge it may generate shear waves which would cause undesirable edge heating of the plasma. It is therefore important to ensure that antenna currents which would excite shear waves are suppressed. This is accomplished by covering the antenna loop with a Faraday shield [NOT86], which has the additional advantage of protecting the antenna from the plasma. However, the Faraday screen can itself be a source of impurities which causes enhanced radiation losses from and dilution of the plasma. Even major disruptions have been found for shields not properly coated or with antenna placement or phasing not adequately considered.

During auxiliary heating in a tokamak, it is observed that the impurity concentrations in the plasma are high, and at least as high during ICRH heating [BEH86A, STE89,ONO86,MAN86] as with other auxiliary heating methods such as neutral beam injection (NBI), where impurity generation is always much higher ($\approx$ 10 times) than during ohmic heating. This is partly explained by the degradation of the energy confinement of auxiliary heated plasmas, the corresponding higher particle outflux, and the consequent higher impurity influx. In the ICRH case in particular, the impurity content is well in excess of that expected from the degradation of the energy confinement. Several studies [BEH86A,STE89,ONO86,MAN86,PER89] have tried to find causes and solutions for this problem, and one candidate is the acceleration of ions near the Faraday shield [PER89] leading to sputtering of the shield material. It has been found that the Faraday screens themselves have a large contribution towards the impurity content in the plasma with screen material introduced into the plasma during ICRH operation, although the screens are situated behind the LCFS.

A schematic of an ICRH antenna is shown in Fig. 5.1.

The three Faraday shields on JET are made from nickel, one of which is plated with chromium. The shields are all protected by surrounding carbon tiles. The vessel walls, made of Inconel, were not covered by low Z material during the early years of operation. The use of the chromium-plated (shield) antenna led to much higher chromium impurity content in the plasma, and pointed therefore directly to the Farady screen itself. The same phenomenon was found with the operation of the nickel (shield) antennae. The source of these higher impurity concentrations was confirmed by direct spectroscopy [BEH86A] of the shield during operation of the

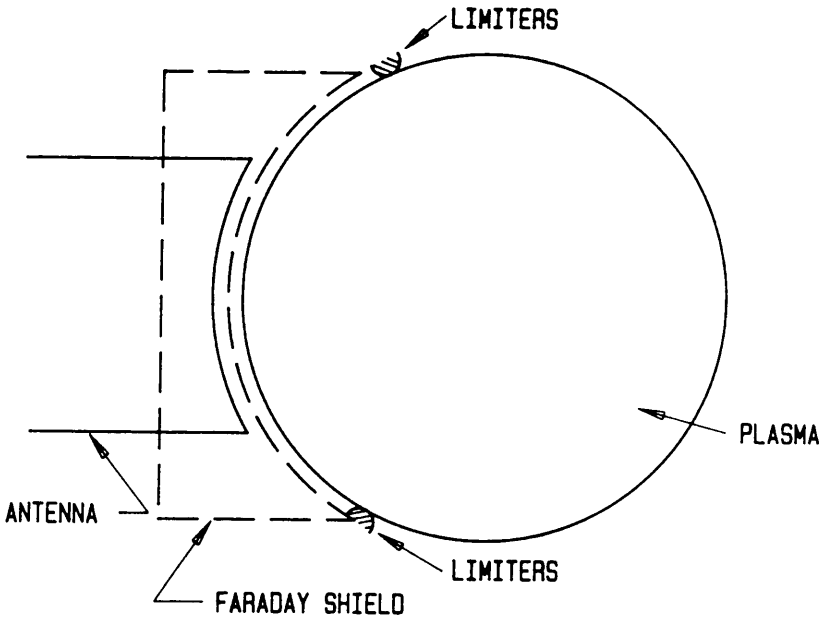

Figure 5.1: **Schematic of the ICRH antenna in a tokamak**

chromium antenna, revealing a large impurity influx from the shield as measured from the Cr I line intensity.

The three possible causes for this phenomenon are sputtering, arcing and evaporation. Evaporation seems unlikely as there are normally no melting effects on these shields, thus making high evaporation rates improbable. There are also very little signs of arcing on these shields.

The most probable possibility is sputtering, and as the only particles which are primarilly heated during ICRH heating are the fuel ions, they should be responsible for the high impurity yield. The antenna and wall components have been analised before [BEH87] and in spite of limiters and other protectors, deuterium is found all over the walls and antenna screens of the tokamak. The occurence of impurities on the measured Faraday plates also indicated the possibility of sputtering on the surface by energetic particles, as shown in Fig. 5.2 [BEH87].

5.2 Experimental

The question whether deuterium heated during ICRH operation was accelerated towards the shields causing excessive sputtering was experimentally studied by in-

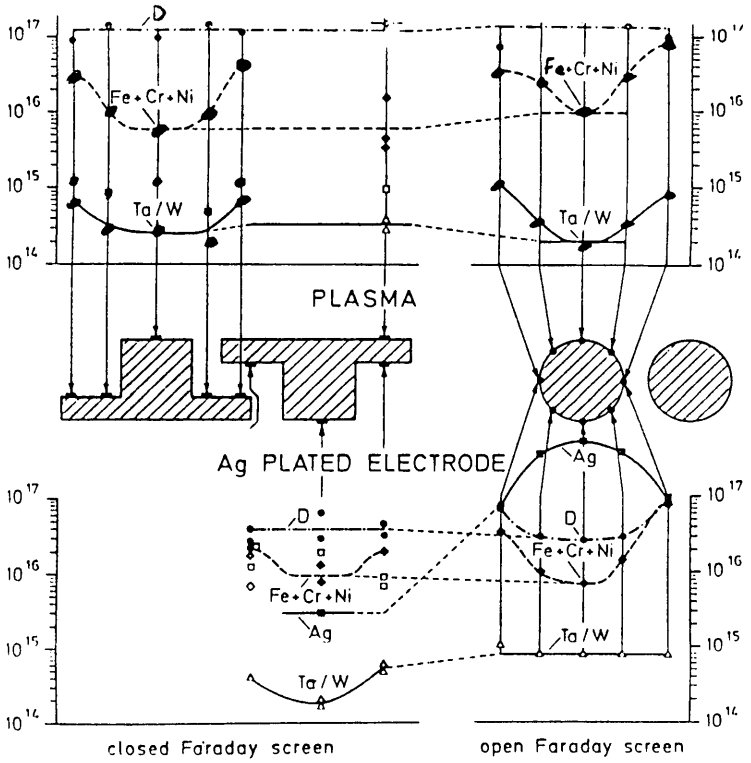

Figure 5.2: **Results of measurements of the Faraday shields, indicating sputtering of the surface [BEH87]**

serting a probe into a tiny hole in the ICRH antenna-shield unit of ASDEX. The setup is indicated in Fig. 5.3 with (1) Faraday screen; (2) centre conductor; (3) return conductor; (4) short circuit; (5) vacuum vessel and flange; (6) stainless steel pipe; (7) flexible teflon rod; (8) bellows (9) flange connection; (10) vacuum valve; (11) to vacuum pumps and (12) carbon probe.

The carbon probe could be pushed in and out of position between discharges and therefore it was possible to be extended into the plasma for only selected conditions. It was soon established that even one discharge gave sufficient yield for analysis of the probe surface by ion beam techniques. This was to good advantage, as this eliminated the uncertainties of trying to maintain the same parameters during different discharges for a single probe. The first analyses were initiated to measure any deuterium excess on the ICRH carbon sample. This was indeed shown to be the case, indicating that deuterium is at least partly responsible for the higher impurity influx.

The deuterium was measured using the $D(^3\mathrm{He},\alpha)\mathrm{p}$ resonance reaction with an ϵ-value of 18.341 MeV.

With the resonance behaviour of this reaction at $E_d = 760$ keV, it was therefore also possible to do depth profiling although the depth resolution was not good, with the

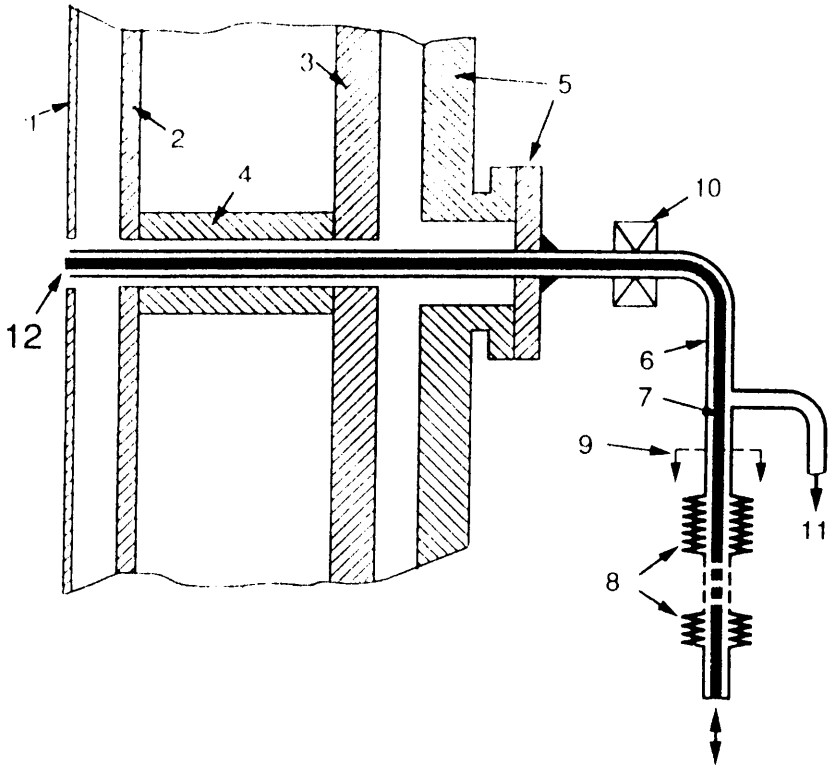

Figure 5.3: **Hole in ICRH antenna where a probe can be installed for diagnostic purposes**

resonance width being > 100 keV. The importance of getting the deuterium content as a function of depth for identifying the mean energy of the incident plasma ions, was soon realised.

Further methods for detection of deuterium and other contaminants were therefore studied to establish the optimum analytical method for this purpose. These methods included elastic recoil detection (ERD), PIXE and NRA measurements. Initial results of probe analyses were obtained from all these methods.

It was soon realised that not only the deuterium content, but also the hydrogen content in the exposed probes was important due to hydrogen in the plasmas and water remnants on the probes, because carbon shows saturation properties for hydrogen and its isotopes. It was therefore established that ERD with helium ions was the best available way of analysing both deuterium and hydrogen. The ERD measurements identify the hydrogen and deuterium content with peaks that did not overlap. This gives a relatively easy method to obtain depth profiles of these two elements in a substrate like carbon, as stopping of the helium ions in the sample is high, and the cross section of the reaction is smooth as a function of bombarding energies. The cross sections for forward scattering is also fairly high, resulting in high sensitivity for the detection of hydrogen and deuterium. ^{4}He ions were accel-

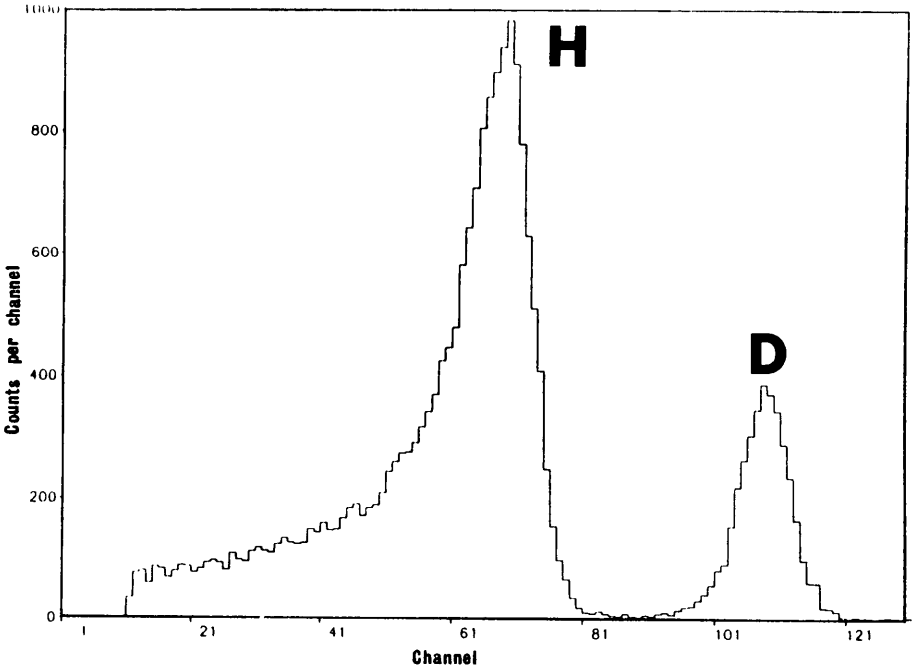

Figure 5.4: **Spectrum of hydrogen and deuterium in a carbon sample obtained with ERD**

erated to 2.6 MeV, analysed and directed onto the samples in the Ruckstreutopf target chamber at Garching. The target was bombarded at an angle of 75° from the normal to the surface of the target. The forward recoiling ions were measured with a surface barrier detector placed at 30° with respect to the incident beam. The signals from the detector were fed to a pre-amplifier followed by an amplifier. The amplifier signals were analysed by an analog-to-digital converter (ADC) and displayed and stored in a multichannel analyser (MCA).

A spectrum obtained from the analysis of a probe that had been exposed to 5 discharges with ICRH heating is shown in Fig. 5.4.

A problem encountered was that the hydrogen content of samples prior to exposure was so high that it was impossible to obtain significant data after exposure. This problem was solved by baking the targets at $1600 - 1700$ ° C for approximately one hour, resulting in a reduction in the hydrogen content to less than 10^{15} atoms/cm^2.

The biggest difficulty of absolute energy calibration of the energy spectrum of the ERD measurements was overcome by using a thin carbon target in the analysis chamber. This target was bombarded with a $^3He^+$ beam of energy 2.0 MeV. The protons (ground state, first and second excited state of ^{14}N from the $^{12}C(^3He,p)^{14}N$ reaction) were detected in exactly the same configuration and used as energy ref-

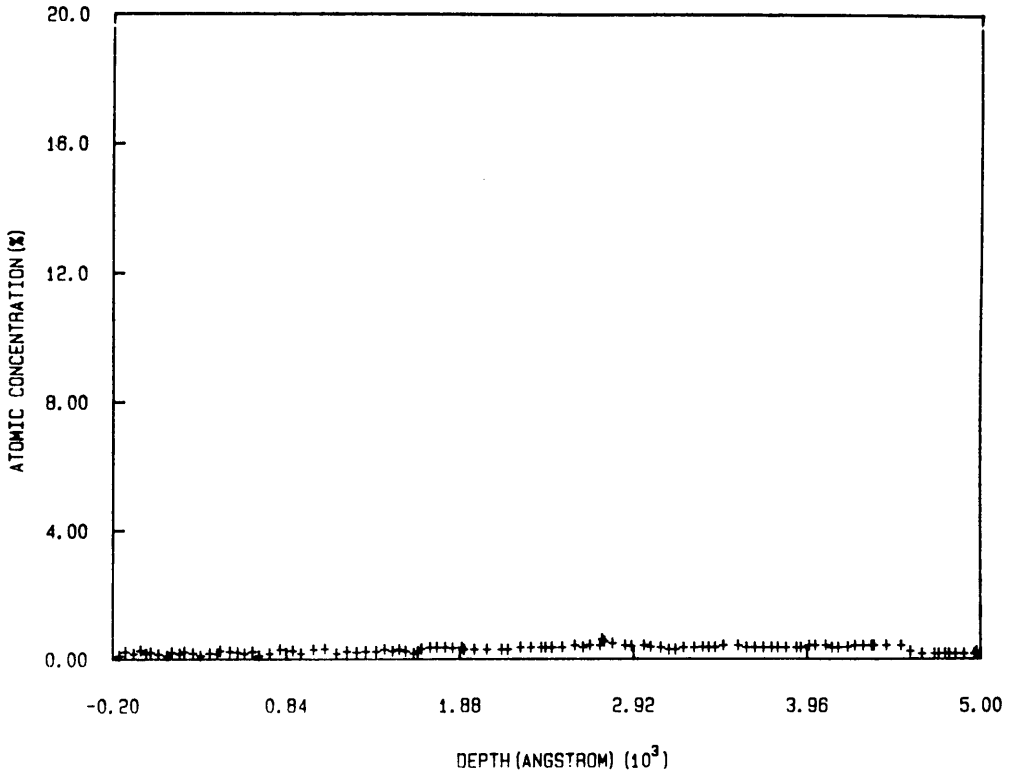

Figure 5.5: **Reduction of the initial hydrogen content by baking**

erence. This reaction was particularly suited for this purpose with the elastically scattered ions stopped in an iron foil (5 μm) in front of the detector, which is a permanent feature of glancing ERD configurations where a thin foil is the standard way of stopping the vast number of the elastic scattered ions from reaching the detector. This foil was used under these conditions to stop the elastically scattered ^{3}He ions from penetrating the detector during actual measurements, preventing pile-up, and excessive dead-time losses in the detector.

The energies of the protons detected also cover a large range, and are equally spaced in energy, making it ideal for the energy calibration of the detector. The different stopping powers for the protons of different energies make the energy calibration non-linear with respect to channel number.

The different contributions from hydrogen and deuterium from ERD measurements are clearly distinguished. The depth profiles of these two isotopes are shown in Figs. 5.6 and 5.7 respectively.

The ERD measurements were regularly complemented by NRA measurements, using the ^{3}He(d,p)^{4}He reaction at 790 keV energy for the incident ^{3}He ions. These measurements for the deuterium yielded no new information on the distribution of deuterium in the samples, and the main emphasis stayed with the ERD measurements with the NRA measurements used as cross reference for the total amount of

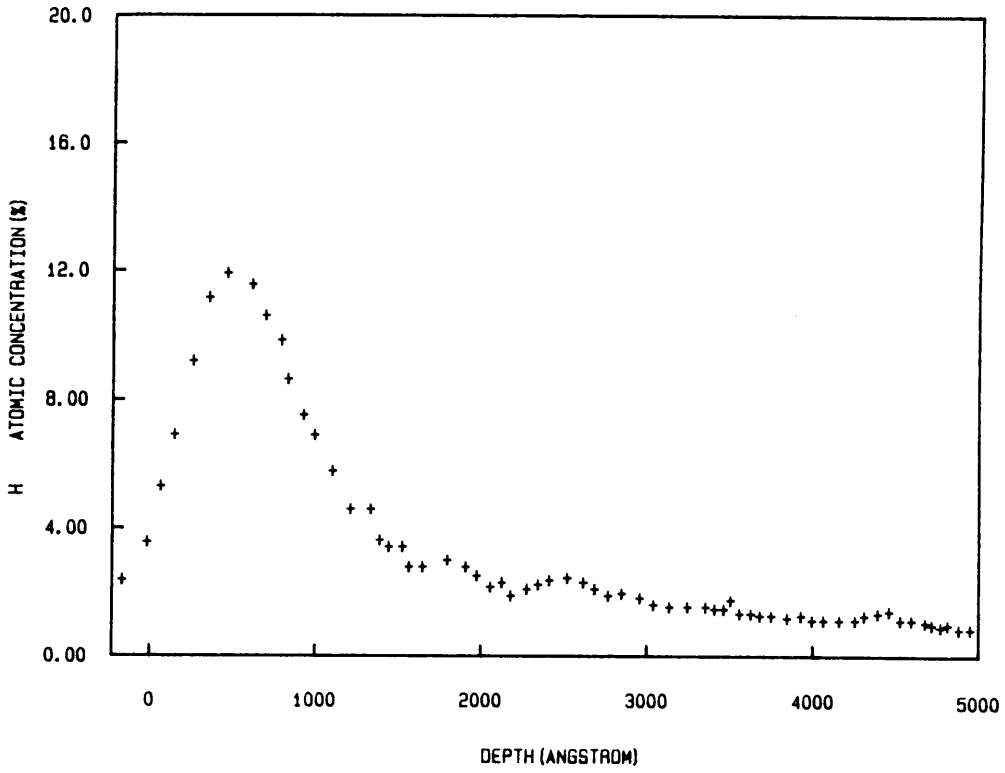

Figure 5.6: **Hydrogen depth profile from ERD**

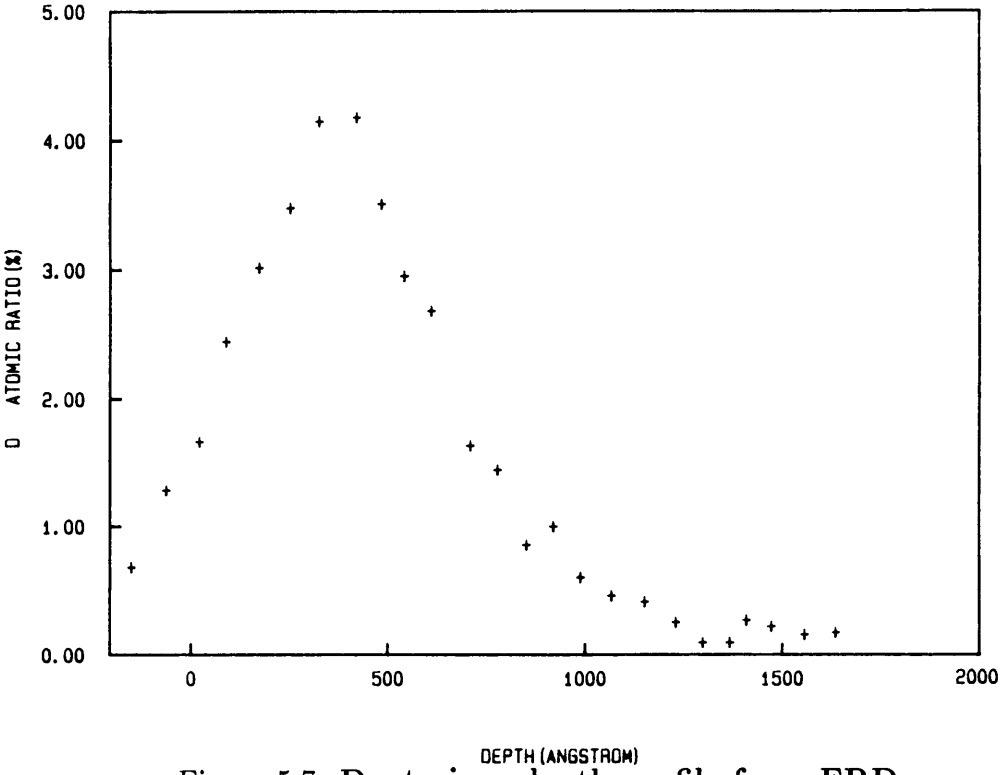

Figure 5.7: **Deuterium depth profile from ERD**

deuterium in the samples.

It was also found that repetitive bombardment of a sample with the relatively high energy of the analysing beam, led to induced emission of hydrogen and deuterium from the targets. As a result a target could only be analysed $\sim$ 3 times before a significant amount was lost from the target, although the losses after one analysis were insignificant.

To study the impurity content of the heavier elements in the samples, PIXE measurements were made with protons at an energy of 1.5 MeV. The characteristic X-rays from the elements present in the samples were analysed with a Si(Li) detector attached to the normal amplification electronics and ADC/MCA. A spectrum obtained from an unexposed sample is shown in Fig. 5.8, showing small quantities of the polish components used.

The PIXE results obtained for unexposed and exposed samples showed no clear indication of specific processes during discharges, as impurities expected from the plasma were present in measurable quantities as contaminants before exposure to the plasma. The problem was addressed by exposing the samples to more discharges to get higher yields in the exposed probes, but the only real information obtained from the PIXE measurements was that the polishing process for the samples beforehand (the surfaces must be very smooth to be able to do the ERD measurements due to the glancing angle of incidence of the ion beam) contaminated the targets with a large amount of calcium, and that the copper impurity content was raised by approximately a factor of five. The copper implanted from the plasma during discharges can be important as the only source of copper is the divertor plates in the divertor chamber of ASDEX.

Initial pre-baked targets were exposed to the plasma with the ICRH heating coupled to the plasma and compared with probes exposed to only ohmic-heated discharges with similar plasma parameters.

Results of ERD measurements made on these probes indicated that there was a definite dependency of the amount of hydrogen and deuterium deposited, as well as the energy of deposition on the plasma parameters. These energies peaked at about 2 keV and 1 keV for hydrogen and deuterium respectively, with ICRH heating applied. The energies were determined from the stopping powers of these particles in carbon [ZIE77A]. These energies are high compared with typical edge temperatures ($<$ 100 eV), and indicates that there is some acceleration mechanism during the heating phase, whereby hydrogen and deuterium are implanted in the sample at energies in excess of 1 keV. The implantation energy is also dependent on the application of second harmonic or minority modes of heating, where the $\sim$ 5 % hydrogen in the deuterium discharge is primarily heated.

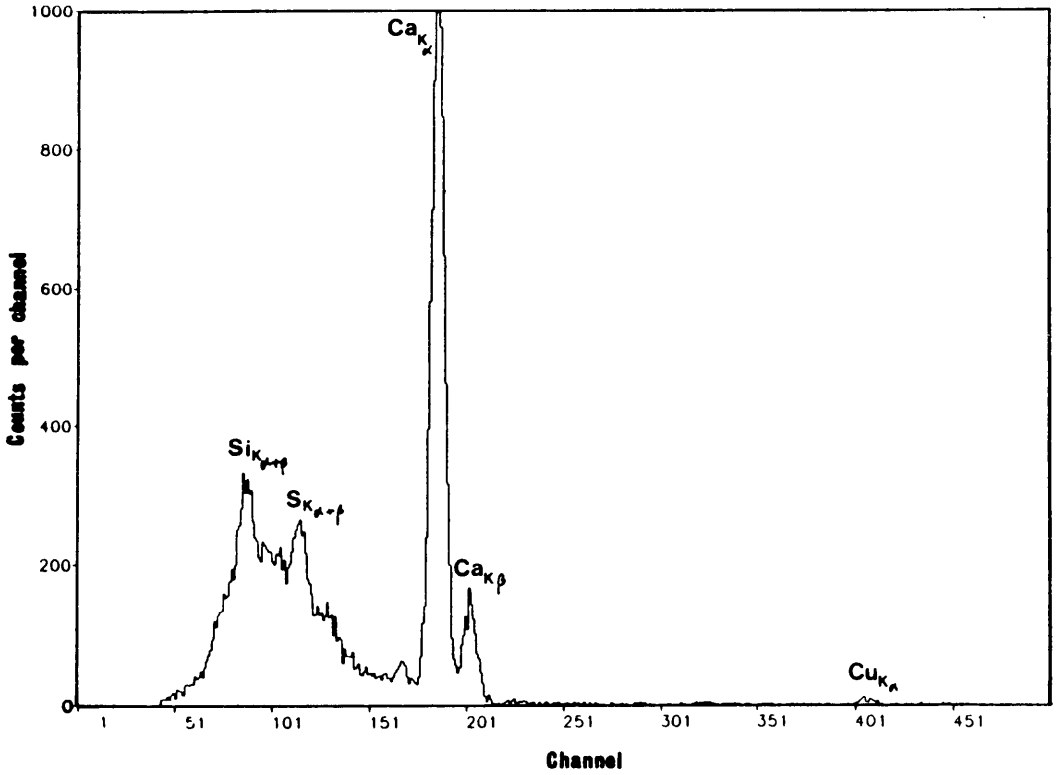

Figure 5.8: **PIXE spectrum of heavy impurities in an exposed sample**

Next the depth profile results obtained by the ERD measurements were checked. Similar carbon targets (treated in the same way as before) were implanted with deuterium of different fixed energies (3 keV and 6 keV) with an ion implanter to ensure that the system was properly calibrated, and to determine the resolution of the system. The resolution in these measurements was determined to obtain the error bars on measured depths, and these were used to obtain information on the resolution of the energies of the implanting beams of particles.

The characteristics of the implanted energies of the ICRH probes were confirmed with the series of measurements where the mean energies of the hydrogen and deuterium implants during the discharges were obtained. The main limitation of the analysis was the large error bars with respect to the depth resolution, which were of the order of 20 % to 30 %. This of course limited the conclusions that could be drawn from these measurements.

All probes exposed to ICRH heating were submitted to minority or second harmonic heating. This was done mainly in deuterium, but also in helium plasmas with the result that in none of the probes was the deuterium primarily heated. The results of these experiments done at ASDEX, and discussed in the next section, were reported earlier by Wesner *et al.* [WES90].

5.3 Minority heating

For minority heating (H-minority in He), 3 probes were exposed in the antenna at different ICRH power levels and different pulse lengths. One additional probe was used in a discharge with comparable plasma parameters, but with neutral injection heating and without ICRH. For one discharge a control probe was exposed with a manipulator at a toroidal distance of about 1.5 m from the antenna (used for the insertion of the probes during discharges) and 3 m from the other antenna. For all these probes both antennae were operated simultaneously with equal power and pulse length.

Depth profiles of hydrogen and deuterium, measured in an antenna probe and in the control probe away from the antenna, both exposed during the same discharge, are shown in Fig. 5.9. The mean energies corresponding to the depth values are also given in the figure. Since the deuterium content was quite small and uncontrolled, no conclusion should be drawn from the H/D ratio.

The total implanted amount of the H and D and its dependence on the product of power times pulse length (i.e. the total energy added to the plasma by the ICRH) is shown in Fig. 5.10. The equivalent values of the control probe without ICRH and of the probe installed far from the antenna are also plotted. The amounts

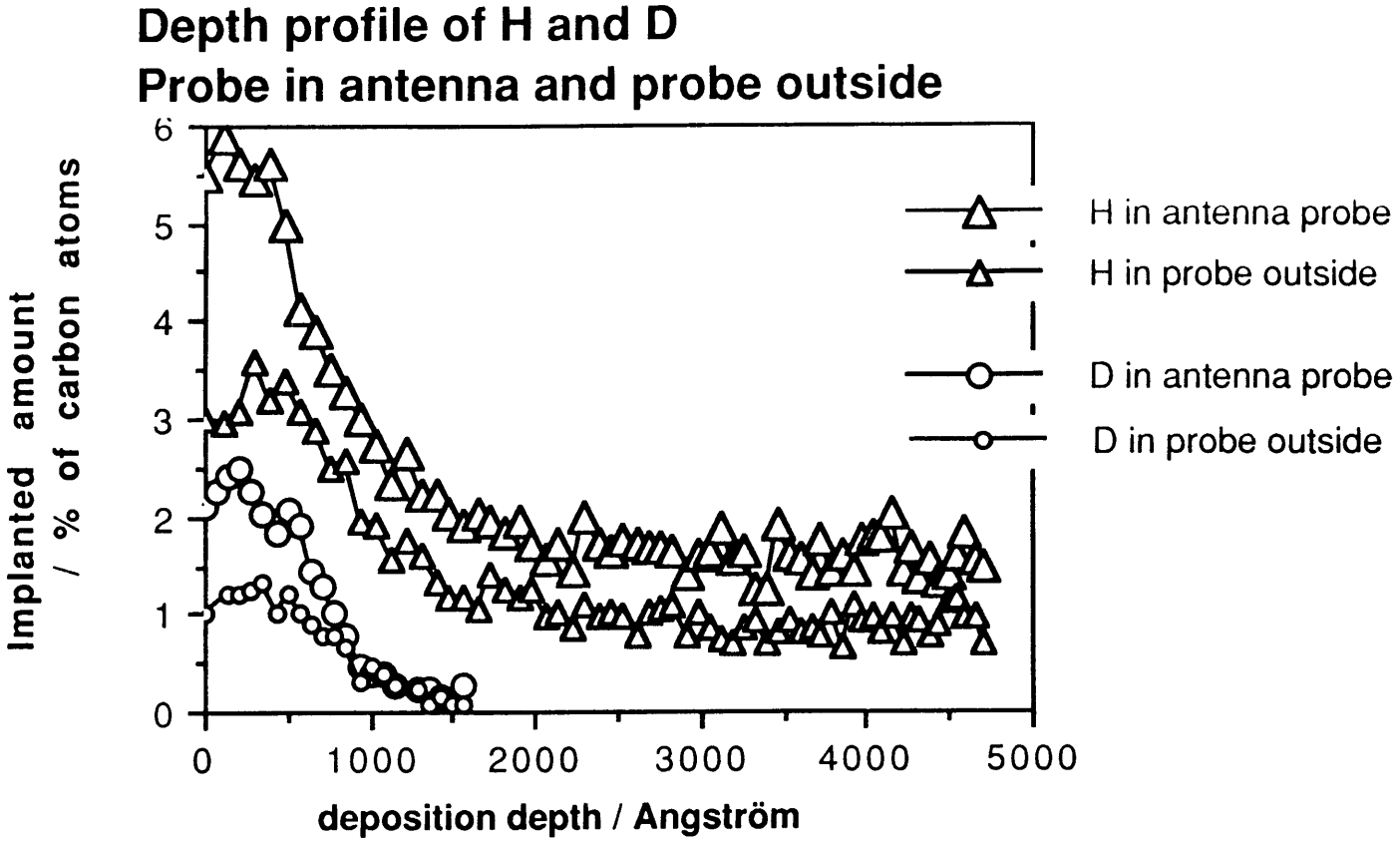

Figure 5.9: **Depth profiles of implanted hydrogen and deuterium atoms in the antenna probe and in the control probe at a toroidal distance of 1.5 m from the antenna (probes No. 7 and 7s, ASDEX shot No. 29 133). In the lower scale mean energy values are given, corresponding to the depth.**

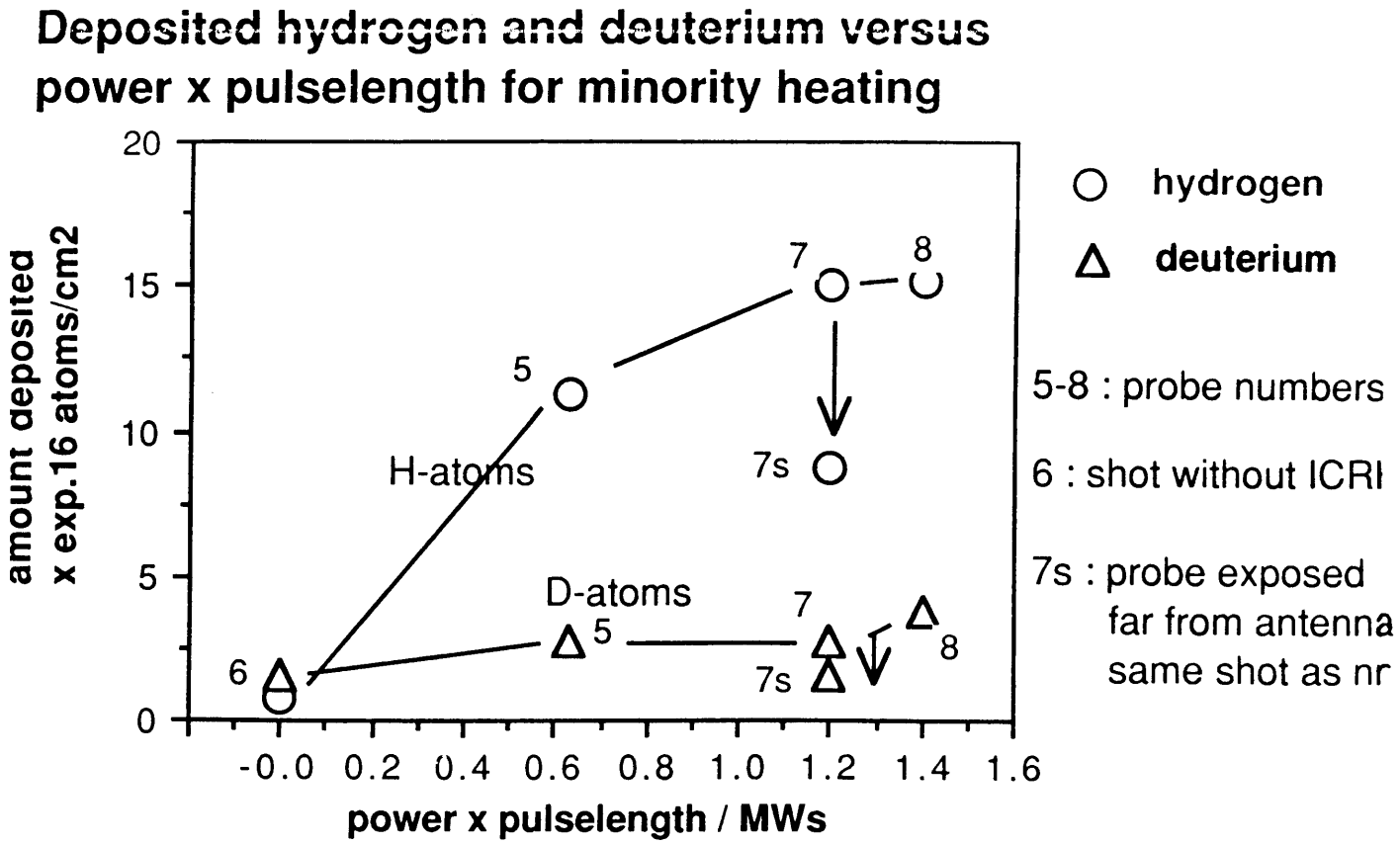

Figure 5.10: **Implanted hydrogen and deuterium versus ICRH power times pulse length for minority heating (H in He)**

increase with increasing power times pulse length. This is also more pronounced for hydrogen, which finally shows a saturation for larger amounts. Indeed, the maximum values for H correspond to the known saturation concentration of hydrogen in carbon [STA88A].

5.4 Second Harmonic heating

For the second harmonic heating of hydrogen (> 30 % of hydrogen in a deuterium plasma), 2 probes were exposed and analysed. The depth distribution showed a peak at 230 angstrom for H and 200 angstrom for D, corresponding to a mean energy of 1.6 keV and 1.4 keV respectively. The total amount is shown in Fig. 5.11 for both probes. The hydrogen is implanted to saturation in both cases, while the amount of deuterium increases again with total power applied.

Within the error bars no clear dependence of the depth of implantation, corresponding to their average energies of implantation, was observed in either of the two cases studied.

The results for the implanted amount of H and D in the exposed carbon show a

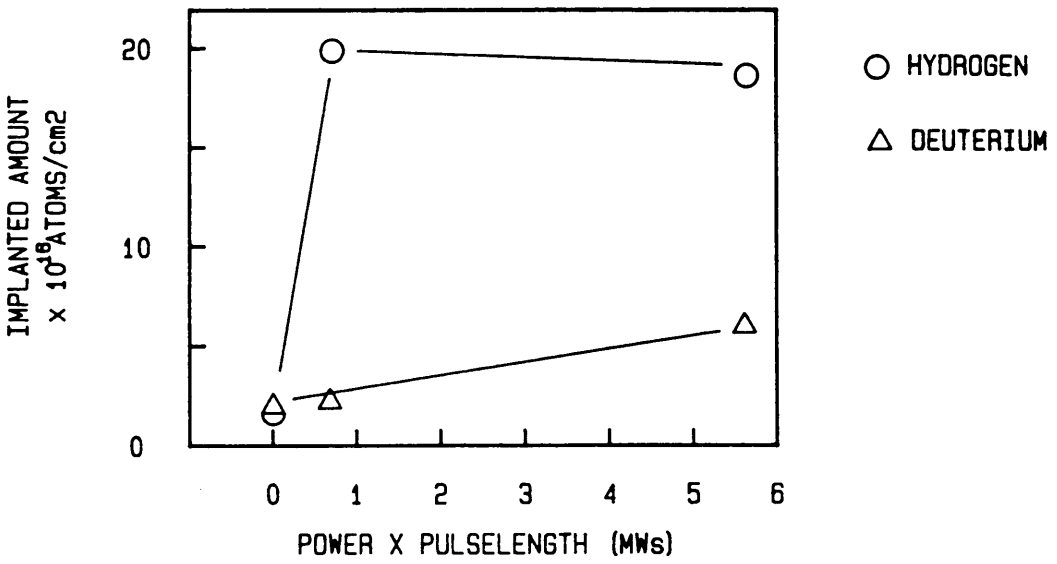

Figure 5.11: **Implanted hydrogen and deuterium versus the product of ICRH heating power and pulse length for two discharges with second harmonic heating. The values of the probe without ICRH are also included. Saturation is reached in the carbon for hydrogen implantation.**

clear tendency to increase with the power and pulse length, as long as saturation of hydrogen in the carbon was not reached. To avoid saturation (for hydrogen, especially in the case of second harmonic heating), shorter ICRH pulses should be applied.

5.5 Discussion

The small number of probes exposed does not allow detailed conclusions. The measured dependencies as shown in Figs. 5.9 - 5.11, however, gives some indication about the impurity production mechanism during ICRH. The measured amounts of H and D indicates a fluence of about 10^{20} D per m^2MWs, and of $> 10^{21}$ H per m^2MWs for both minority (H in He, containing some D) and second harmonic heating of H in a H/D mixture plasma. The average energies of these particles are in the range of 1 to 2 keV, assuming normal incidence, otherwise the energies are higher.

These fluxes are higher and more energetic than the charge exchange (CX) neutral particle fluxes as measured with a neutral particle detector at the midplane of ASDEX during ICRH heating in the same discharge. This is shown in Fig. 5.12, where the calculated depth profile due to the CX neutral bombardment is compared with the flux measured by the probes. The calculational procedure used is described in Appendix A, and the measured CX fluxes were obtained from Fahrbach and Hermann [FAH89]. The total fluence of the CX neutrals is about a factor 20 smaller and the average energy is considerably lower. This indicates that the particles measured by the probes during ICRH are probably energetic ions, and not neutrals.

The fast particles during ICRH are created either in front of the antenna, moving around the torus and sputter wherever they hit the shields, divertor plates or walls, or they are created all around the torus e.g. by waves, the maximum of this process still being in the antenna region. This is indicated by the depth distribution of the implanted H and D in the control probe distant from the antenna, which shows a similar function, but a smaller fluence (Fig. 5.12).

For the measured fluence, with a sputtering yield of 0.02 for D and $8{\cdot}10^{-3}$ for H and with the antenna shield area about 0.23 m^2 (ASDEX), a flux of about $2{\cdot}10^{18}$ atoms/s are sputtered from each antenna. If the area, at which these particles could hit the wall, is about 10 cm wide all around the torus (e.g. at the entrance of the two ASDEX divertors), this number would be further increased by a factor of 10. If only a few percent of these sputtered particles reaches the plasma core, they would explain the impurity production during ICRH.

From the measurements it was, however, clear that the acceleration process is not

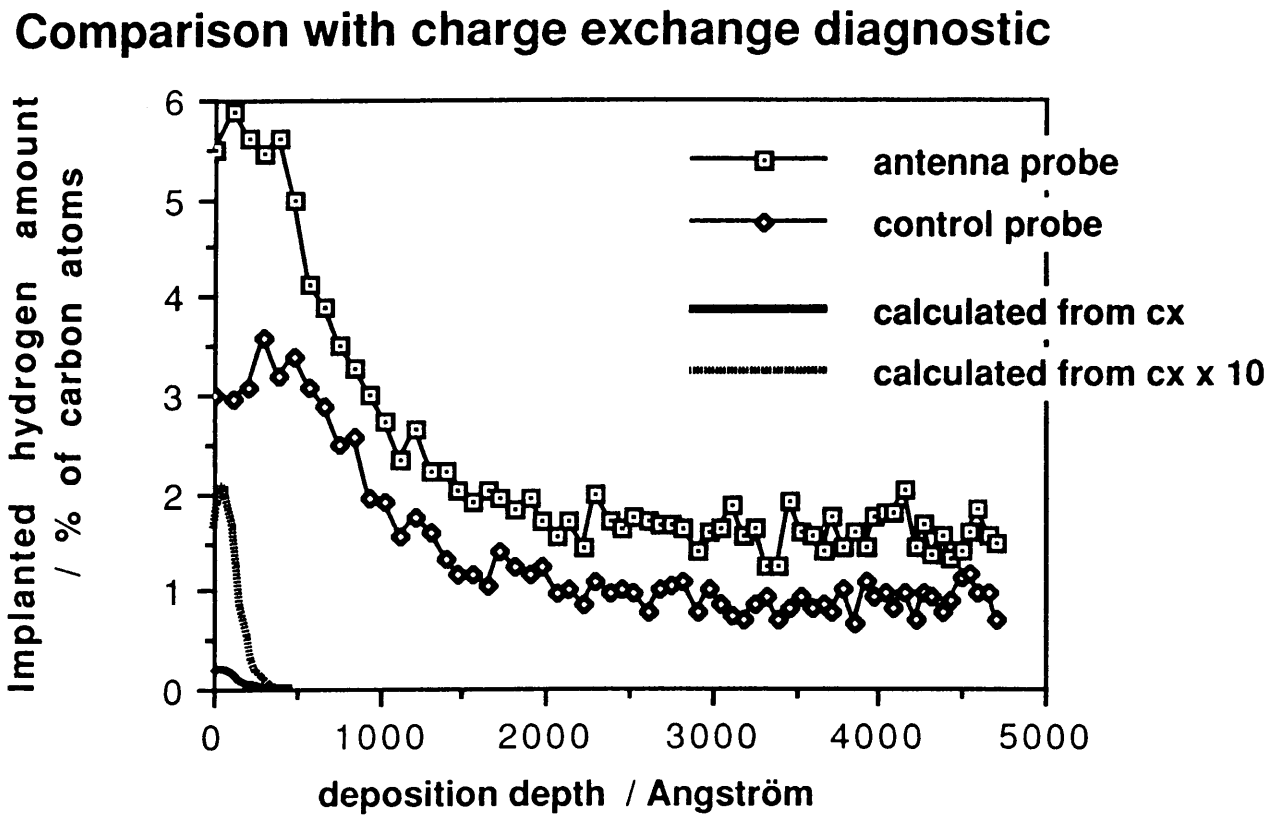

Figure 5.12: Comparison between the deposition profile of implanted hydrogen measured at the antenna probe and at the control probe with a profile calculated from the measured energy spectrum of the CX neutrals (solid line)

absolutely local. Although the region around the antenna showed the biggest effect, the measurements at the opposite side of the antenna also showed some effect of high energy particle implantation.

Chapter 6

A simple model of the charge exchange (CX) neutral flux to the first wall of a tokamak

In a tokamak the ions which are magnetically confined at high temperatures, with the ultimate goal of obtaining fusion, are always introduced as neutral particles fuelled into the plasma volume. Fuelling is done through gas puffing, pellet injection, neutral beam injection and also through recycling of fuel ions lost from the plasma column. In JET the particle confinement time is typically ~ 0.1 of the discharge time, i. e. on average every fuel particle strikes the limiter or wall ~ 10 times during the discharge. The molecules from refuelling and the neutral atoms and molecules from recycling can undergo several reactions as they enter the plasma.

Consider an ion leaving the plasma, striking the plasma-facing material (limiter or divertor) with an energy of 80 eV [HEI86], corresponding to an edge temperature of 16 eV (see eq. (3.104)). Here the ion has a finite probability of reflection or backscattering (i.e. recycling), which includes desorption of an atom of the same particle species. If the recycling coefficient is ~ 1, the recycled deuterium has a probability of ~ 0.3 to recycle as D^0, and ~ 0.35 to recycle as D_2^0 [HEI86] and can have, for example, an energy of 40 eV. The probabilty of recycling as an ion is negligible.

Reactions that dominate for the molecules flowing towards the plasma are:

$$D_2 + e^- \rightarrow D_2^+ + 2e^- \tag{6.1}$$

$$D_2 + e^- \rightarrow D^o + D^o + e^- \tag{6.2}$$

$$D_2 + e^- \rightarrow D^+ + D^o + 2e^- \tag{6.3}$$

and for the molecular ions:

$$D_2^+ + e^- \rightarrow D^+ + D^o + e^- \tag{6.4}$$

The reaction rates for the possible reactions of the molecules as a function of temperature are shown in Fig. 6.1 [HAR86]. A possible sequence of events is shown in Fig. 6.2 [HAR86] for a hydrogen molecule. The two primary processes of interest are ionisation (reaction (6.1) with probability 0.8) and dissociation (reaction (6.2) with probability 0.2). About half the atoms from reaction (6.1) join the recycling flux of neutral atoms and the other half is lost to the walls. The ionised molecule undergoes dissociation (reaction (6.4) with probability 0.98) and the ions participate as fuel ions in the plasma, while the neutrals become part of the neutral density. In a divertor operating in the high recycling regime the processes transforming the molecules to ions and atoms will predominantly take place in the SOL [HOW82]. In this way the neutral atoms make their way into the plasma, and can take part in the processes inside the bulk plasma.

Three dominant reactions take place [HAR86] as the neutral atoms cross the SOL and enter the plasma. These reactions are:

$$D^o + D^+ \rightarrow D^+ + D^o \tag{6.5}$$
$$D^0 + e^- \rightarrow D^+ + 2e^- \tag{6.6}$$
$$D^0 + D^+ \rightarrow 2D^+ + e^- \tag{6.7}$$

The atoms can be ionised, (6.6) and (6.7), and they can become part of the ion density participating in the fusion process, or they can undergo charge exchange (CX) processes, (6.5), with the ions. The reaction rates of these reactions are shown in Fig. 6.3 [HAR86]. The process of CX is important in fusion experiments, as the reaction is species-symmetric and resonant, with a high reaction rate, and the energetic neutrals created are not confined by the magnetic field, therefore they are lost from the plasma. Furthermore these particles lead to effective cooling of the plasma, as cold neutrals are exchanged for higher energy ions from the plasma. It is thus of importance to be able to model and understand the neutral particle flux from and into the plasma.

A complete neutral transport model must include at least the following parameters: (a) neutral plasma interactions, i.e. reactions of hydrogenic and impurity atoms that

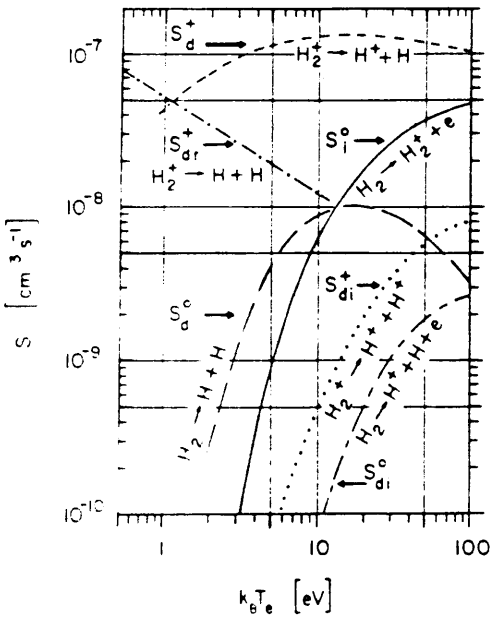

Figure 6.1: **The reaction rates for the dominant reactions for the molecules as a function of temperature**

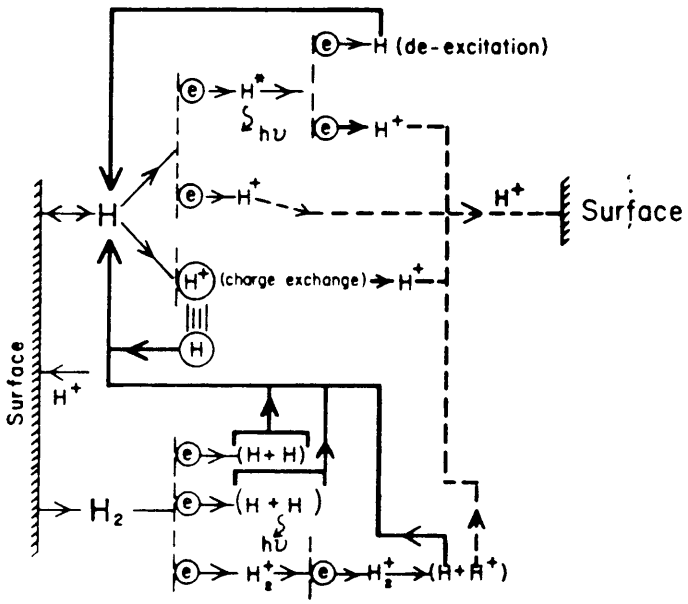

Figure 6.2: **A possible sequence of events for recycling deuterium**

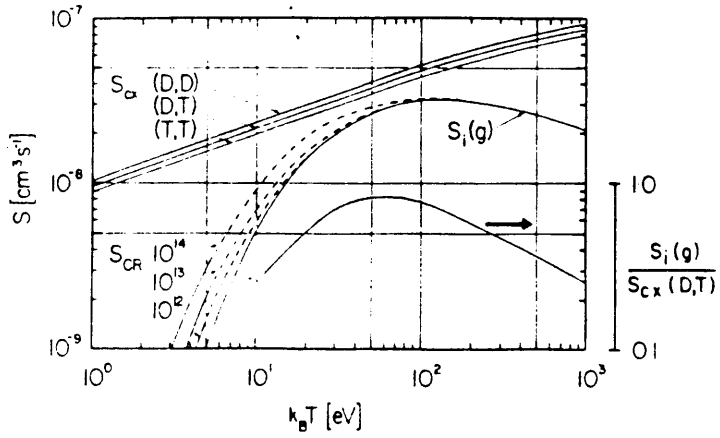

Figure 6.3: **The reaction rates for the dominant reactions for the neutral atoms as a function of temperature**

commonly occur in the plasma over a temperature range of 1 - 10^4 eV [HAR86]. (b) Neutral-neutral and neutral-ion elastic scattering processes for densities larger than 10^{20} m^{-3} (as is the case in high recycling divertors). (c) A realistic wall reflection model such as described in [BEH86] should be incorporated together with a model of wall sputtering for impurity transport studies. In relatively closed components such as divertors and pump ducts the geometry must also be taken into account.

Complex codes exist (mostly adapted from codes describing neutron transport) describing neutral particle transport in high temperture and high density plasmas. Monte Carlo codes such as DEGAS [HEI86], MARLOWE [ROB74] and AURORA [HUG78] are among those that are often used with good results. These codes include complex geometries, and all the relevant reaction mechanisms. They therefore also yield accurate results and are especially useful to study low-energy neutrals in closed geometries and near limiters, pump ducts etc. where the low-energy part of the neutral spectrum is generated to a large extent. These codes are, however, costly and time-consuming to run.

It is for this reason that it is also of interest to study semi-analytical global models, lacking detail in especially the low-energy neutral spectrum, that can be used to study effects of the neutral flux on the first wall components of a tokamak.

As tokamaks scale up to reach reactor operational conditions in terms of density and energy confinement, this invariably leads to larger machines. One would therefore also expect the CX fluxes to increase approximately linearly with respect to the small radius of a tokamak, corresponding to the volume to surface ratio of the plasma column. This ratio is ~ 1 for JET, and rises to ~ 1.5 for ITER. One would therefore expect the CX fluxes to follow this scaling.

Apart from the cooling consequences already pointed out, these CX neutral particles lead to effective cooling of the plasma through electron energy loss via ionisation. A further result of particles lost to the walls is sputtering of wall material with subsequent dilution of the plasma by high Z (> 3) impurities. This can have serious consequences, as e.g. a fully ionised carbon ion replaces six hydrogen ions for constant electron density, with the radiation energy scaling as Z^2. It has also been shown by Verbeek *et al.* [VER89] and Staudenmaier and Wampler [STA88A] that the charge exchange neutrals are mainly responsible for high Z impurities in the plasma in ASDEX.

In tokamaks with low Z plasma-facing components, the sputtering yield for hydrogenic bombardment peaks at a bombarding energy of $\sim$ 150 - 300 eV, and then decreases fairly quickly with energy [GAU90]. This indicates that the impurity concentration due to sputtering by the CX flux to the walls of a tokamak reactor will be mainly determined by the low-energy part of the CX spectrum (< 1000 eV). This makes the complex Monte Carlo codes the best candidates to realistically calculate

these fluxes and their influence. For the calculation of the contribution of the CX flux to fusion reactions in the walls, however, the maximum contribution is at ~ 50 keV, thereby making a global model of CX fluxes, during ohmic heating only, useful in extrapolating to reactor regimes.

Through charge exchange, and also to a smaller extent, recombination processes [DNE79,WEI75], considerable numbers of neutral particles are created. The model presented here derives a particle balance of the plasma ions from their imperfect confinement properties together with refuelling and recycling. The plasma parameters are used to obtain the energy-dependent charge exchange fluxes bombarding the walls. The model described here uses simple relations for the edge properties of the plasma, and includes the temperature and density profiles in the central region. This leads to relatively simple expressions describing the energy dependence of spectra, and linking the temperature profile of the plasma to these spectra. Quantitative results from the model were compared with JET data and extrapolated to the neutral flux in a reactor regime.

6.1 The model

Account is taken of the ions lost from the plasma (mainly to the limiter/divertor). These ions have a certain probability R_1 of being backscattered or re-emitted, and these mainly neutral particles stream towards the plasma. The model divides the plasma into two distinct zones, the edge and the central plasma, the central plasma properties being described by typical parabolic type profiles. The edge characteristics are derived from simple plasma edge considerations. At the boundary between the two zones the temperature and density satisfy certain boundary conditions

External fuelling via gas puffing and also pellet fuelling are included in a similar way. From these relations one can set up a particle balance and look at the behaviour of the neutrals in particular. It is also possible with the model to explain the decrease in fuelling efficiency with external fuelling.

The model is based on a similar model by Behrisch and Kadomtsev [BEH75] for the particle balance in a plasma which considered the helium flux in a burning D,T fusion plasma. No energy dependence of the helium flux was included in that study.

The model is graphically described in Figs. 6.4, 6.5 and 6.6. These three figures indicate the different sources for the creation of neutral fluxes. Fig. 6.4 shows the flux ($\Gamma = \frac{N}{\tau_p}$) of ions to the limiter/divertor due to the imperfect confinement of the ions. The limiter/divertor has a recycling coefficient R_1 and returns neutral atoms and molecules to the plasma. The interactions in the SOL are assumed to

be such that these particles are all D^+ and D^0 before they have entered the SOL significantly, and they have finite probabilities described by the edge properties of the plasma of undergoing different reactions. Only two major processes are considered here, namely CX and electron impact ionisation of the neutral particles.

The neutrals moving towards the plasma volume therefore have a certain probability of undergoing charge exchange interactions or being ionised in the SOL. The ions will be turned back to the walls due to the sheath potential, but about half of the charge exchange neutrals will penetrate the plasma, and undergo further charge exchange with the energetic ions in the plasma, or become ionised. These ions then become the source of fuel in the plasma. The neutrals leave the plasma as part of the total CX flux impinging on the walls.

The recycling coefficient of the wall is designated by R and the returning flux of neutrals are followed in the same way as before in repetition. This process leads to the establishment of power series describing the different fluxes.

In Fig. 6.5 the same process is indicated for the external gas fed into the chamber. The neutral particles are assumed to enter the plasma at the same velocity as recycling neutrals. The same interaction mechanisms are assumed in this case.

The following abbreviations are used:

$$A = 1 - \frac{p_{cx}}{2} - p_{iz} \tag{6.8}$$

$$B = AP_{cx} + \frac{p_{cx}}{2} \tag{6.9}$$

$$C = B + p_{iz} \tag{6.10}$$

with p_{cx} and p_{iz} the probabilities of charge exchange and electron impact ionisation respectively in the SOL. The corresponding probabilities for the main plasma are given by P_{cx} and P_{iz}. A is the probability, for a neutral moving from the wall or limiter, to reach the plasma volume. B is the fraction of the outward CX flux to the inward neutral flux reaching the bulk plasma and C is the fraction of consecutive generations of the inward neutral flux. Pellet fuelling (Fig. 6.6) is similarly analysed, the difference with respect to gas puffing arising from the fact that the primary flux of neutrals only interact in the central region of the plasma.

A particle balance can now be constructed for the source of ions entering the plasma, and those leaving the plasma. The resulting balance is given by:

$$\Gamma = \frac{N}{\tau_p}$$

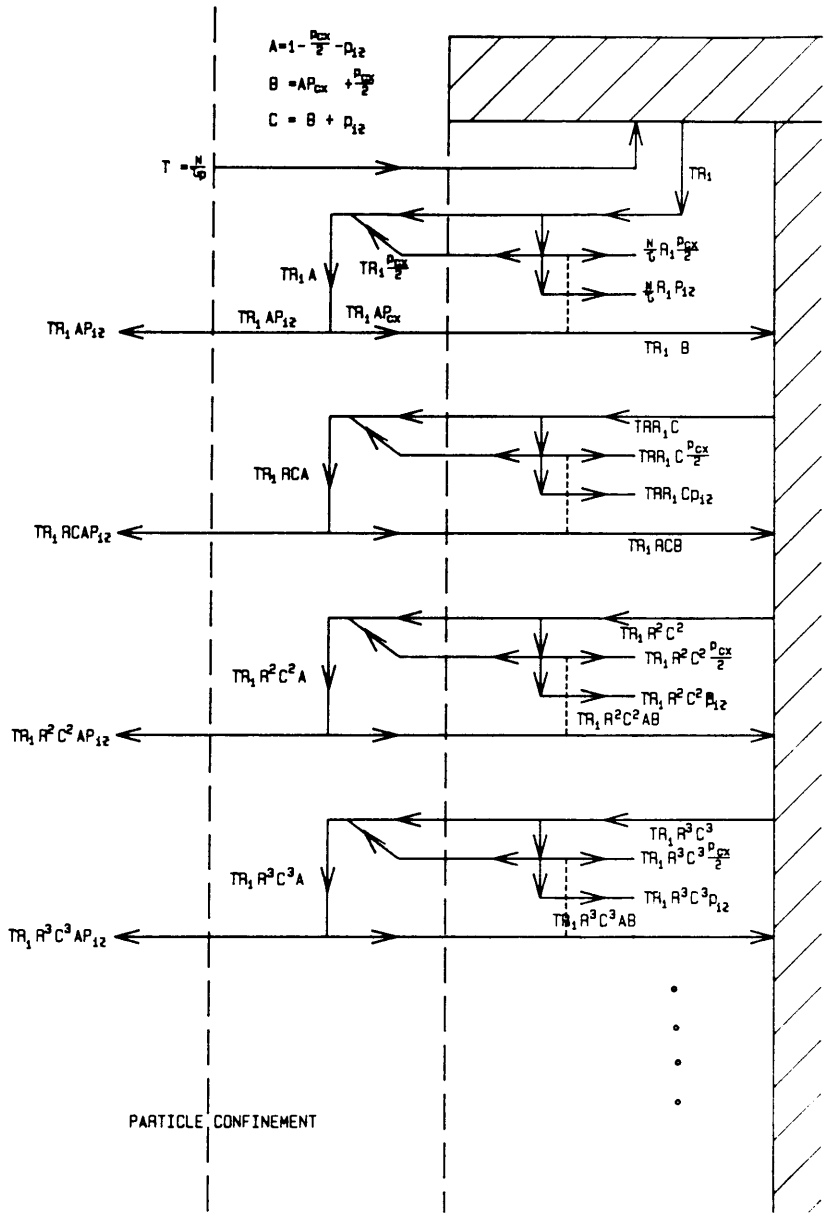

Figure 6.4: **A graphical description of the model considerations: Imperfect confinement of the fuel**

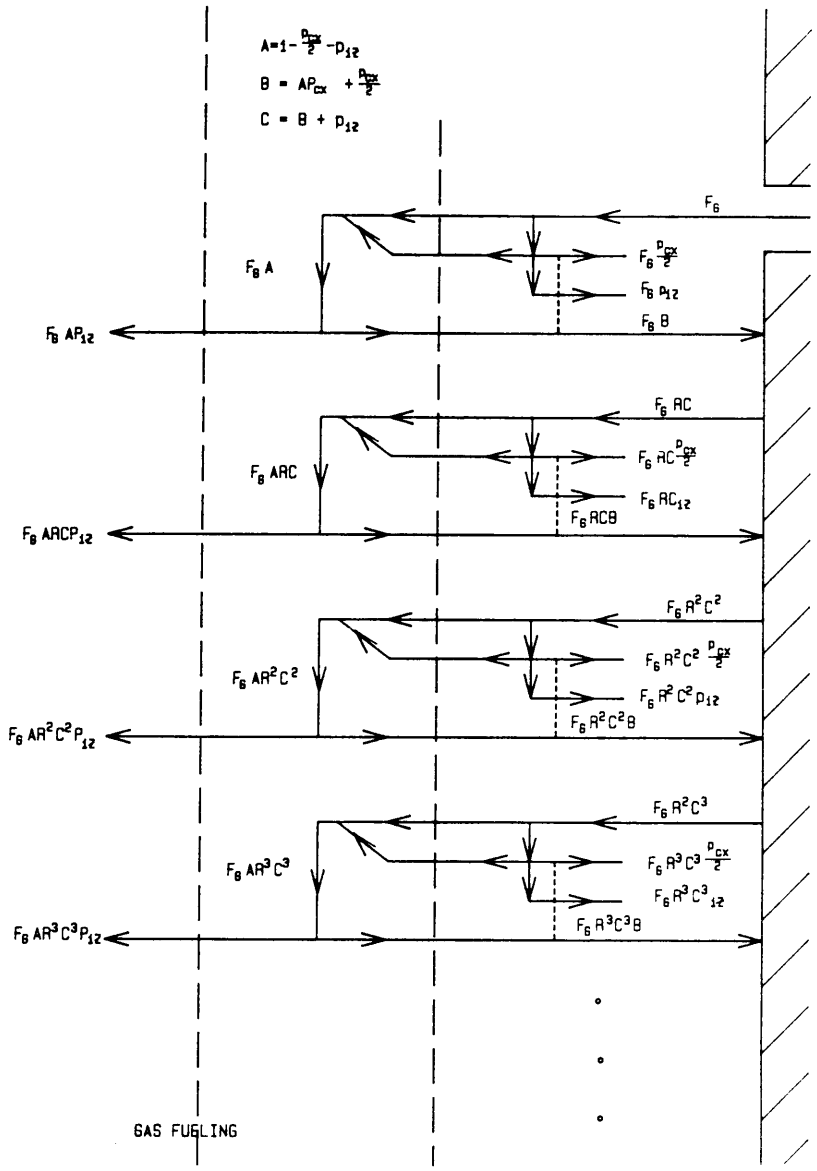

Figure 6.5: **A graphical description of the model considerations: Refuelling with gas puffs**

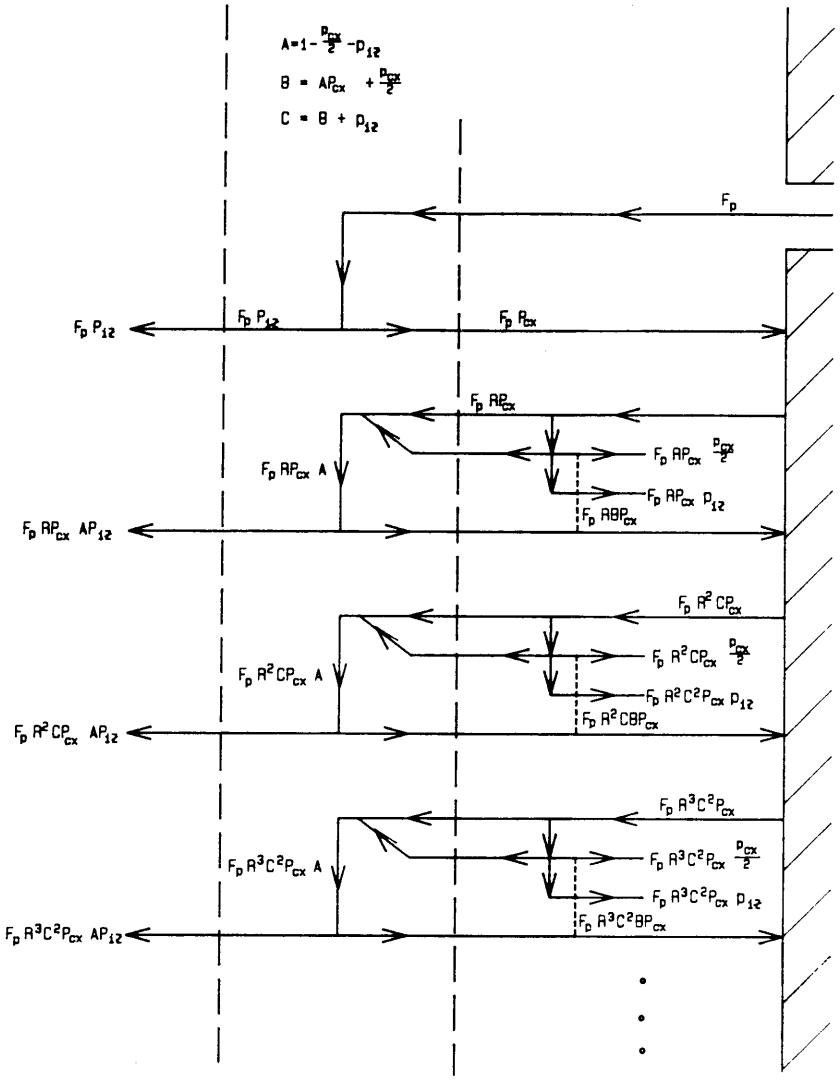

Figure 6.6: **A graphical description of the model considerations: Refuelling with pellets**

$$= \frac{P_{iz}}{(1 - RC - R_1 P_{iz} A)} \{F_G A + F_P \cdot [1 - RC + P_{cx} RA]\} \qquad (6.11)$$

with N being the total number of fuel particles in the plasma, τ_p the particle confinement time, F_G the gas-fuelling rate and F_P the pellet-fuelling rate.

From the above considerations the fuelling efficiency can be determined as a function of discharge time. This can be compared with the experimentally obtained fuelling efficiency on current operational tokamaks, such as the results of Ehrenberg *et al.* [EHR89] on JET. The fuelling efficiency, in general, decreases with increasing time for a constant recycling coefficient.

Assuming only gas puffing, i.e. $F_p = 0$, the fuelling efficiency is given by the ratio of the total number of fuel particles in the plasma to the total number of particles fed into the plasma. If we assume that the fuelling is done to keep the total particle density constant, the efficiency is given by:

$$\epsilon(t) = \frac{N}{N + N_G} \qquad (6.12)$$

as a function of time, with N_G the total number of gas fuel particles fed into the plasma at time t. Substituting the ratio of N and $F_G t = N_G$ of (6.11) into (6.12), assuming that $R_1 \sim R$, the result is simply:

$$\epsilon(t) = \frac{1}{1 + \frac{(1-R)}{P_{iz} A \tau_p} t} \qquad (6.13)$$

The fact that the fuelling efficiency increases rapidly for $R \geq 1$, can be seen with the change of the sign of the denominator, and this results in the divergence of the fuelling efficiency to infinity at some critical time t_0. This time is given by $t_0 = P_{iz} A \tau_p / (R - 1)$. The fuelling efficiency $\epsilon(t)$ is shown for different values of R as a function of time in Fig. 6.7. Together with (6.13) the experimental values obtained [EHR89] are shown. The correspondence is clear, and with the values assumed for JET of $\tau_p = 0.4$ s, $p_{cx} = 0.3$, $p_{iz} = 0.15$ and $P_{iz} = 0.3$ the model corresponds to the experiment at a recycling coefficient $R = 0.94 - 0.96$, a value typical for the recycling for JET [STA90].

Constrained by the convergence of the power series, these relations, however, only hold for the condition $RC < 1$. This translates into:

$$R[AP_{cx} + \frac{p_{cx}}{2} + p_{iz}] < 1 \qquad (6.14)$$

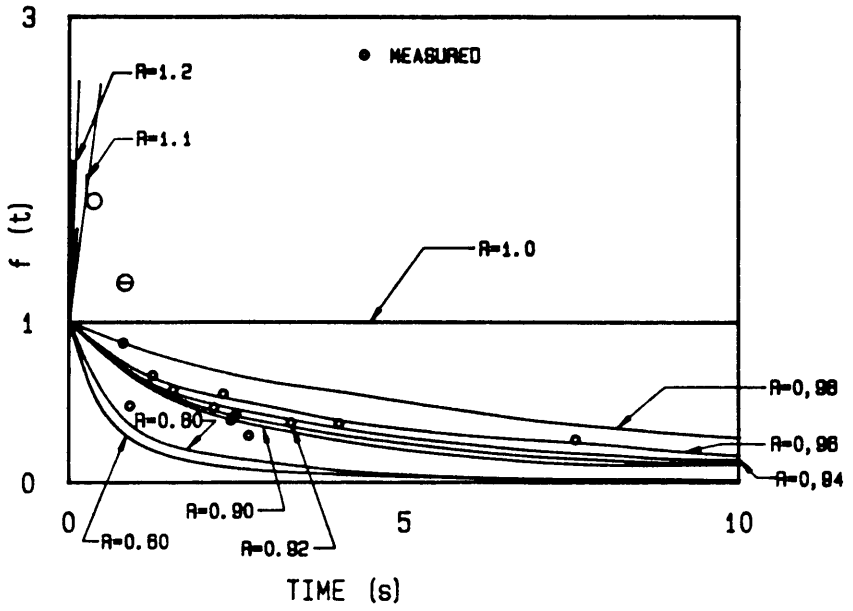

Figure 6.7: **The fuelling efficiency $\epsilon(t)$ for different values of R as a function of time. Together with the model, experimental values are shown.**

For similar values assumed as in the previous case and with $P_{cx} = 0.7$, we obtain for JET a maximum of $R < 1.3$. For larger R the model does not converge into power series.

The CX flux to the walls can also be constructed from Figs. 6.4, 6.5 and 6.6. The same principle is used as in the particle balance and using this eq. (6.11), the total flux of CX neutrals to the wall is given by:

$$\begin{aligned}\phi_{CX} &= \frac{1}{1-RC}\{[\frac{BP_{iz}R_1A}{1-RC-R_1P_{iz}A}+1]\cdot F_G \\ &+ [\frac{BP_{iz}R_1(1-RC+P_{cx}RA)}{1-RC-R_1P_{iz}A}+P_{cx}(1-RC+BR)]\cdot F_P\} \end{aligned} \quad (6.15)$$

From here onwards only gas fuelling was assumed for simplicity and due to the fact that the arguments for both methods are similar and the results for the two processes in terms of the CX neutral flux is very much the same. Using eq. (6.11):

$$\phi_{CX} = \frac{\pi B}{A_p(1-RC)}[\Gamma R_1 + F_g] \quad (6.16)$$

where π is the contribution from a cosine distribution assumption for the fluxes to the wall (see p 152) and A_p is the plasma surface. From the arguments presented, the energy dependence of the neutral flux is inherent in B, which now can be written:

$$B(v,r) = AP_{cx}\hat{f}_c(v,r) + \frac{p_{cx}}{2}\hat{f}_e(v,a) \quad (6.17)$$

where $\hat{f}_c(v,r)$ is the normalised velocity distribution of the ions in the central region of the plasma ($r < a$), and $\hat{f}_e(v,a)$ the velocity distribution at the edge ($r = a$).

With a returning energy of 75 eV for a deuterium atom, with the edge electron density $n_e \sim 1 \cdot 10^{13}$, the edge temperature $T_e \sim 50$ eV and the small radius of the device equal to $a \sim 50$ cm, the total mean free path length for the deuteron is $\lambda_{tot} \approx 13$ cm [HEI86]. This includes CX reactions, electron impact ionisation and the constraints of the vessel walls, thereby indicating that the particle entering the plasma has a limited probability of moving to the central parts of the plasma. It has, however, been found that the measured CX fluxes do not correspond well to this fact, and even in the large devices and densities used today the CX fluxes represent the full temperature profile of the plasma, up to the centre [DNE79] to a certain extent. This can be explained by the fact that the inward bound neutrals have the largest probability of undergoing CX processes with an ion in the plasma, typically being

a factor of 3 larger than the probability of electron impact ionisation at the edge of the plasma. As the CX neutrals can go deeper into the plasma, and the plasma temperature increases above $\sim$ 100 eV, the ratio [HAR86] between the reaction rate for CX and ionisation increases quickly, e.g. at $T = 1$ keV, the ratio is > 4. For higher temperatures the ratio increases even faster. This phenomenon can lead to deep penetration of the multiple generations of these CX neutrals into the plasma. Attenuation of these fluxes is, however, a complicating factor as these neutrals can be absorbed on their path outward from the plasma, and this would tend to flatten the CX spectrum, making it less representative of the plasma temperature profile.

Normalisation is obtained in this model by assuming that the complex process of multiple CX processes and ionisation, as the neutral particles move towards the centre of the plasma, can be approximated by the normalisation $\int_V P_{cx}\hat{f}_c(v,r)dV + \int_V P_{iz}\hat{f}_e(v,r)dV = 1$. In effect it is assumed that the inward bound neutrals are normalised to the probability of undergoing one ionisation or CX in the plasma volume.

6.2 Edge considerations

The edge parameters as described in section 2.1 are used for assigning values to the density e - folding length λ_n from eq. (2.20). The mean free path for CX by the inward neutrals is given by:

$$\lambda_{cx} = \frac{v_d}{n_e(a)\langle\sigma v\rangle_{cx}(kT_e)} \tag{6.18}$$

where v_d denotes the velocity of the impinging neutral, $n_e(a)$ is the electron density at the edge and $\langle\sigma v\rangle_{cx}(kT_e)$ is the CX reaction rate at the edge. Similarly for electron impact ionisation the mean free path is:

$$\lambda_{iz} = \frac{v_d}{n_e(a)\langle\sigma v\rangle_{iz}(kT_e)} \tag{6.19}$$

The probabilities p_{cx} and p_{iz} are then given by:

$$p_{cx} = \frac{\lambda_n}{\lambda_{cx}} \tag{6.20}$$

$$p_{iz} = \frac{\lambda_n}{\lambda_{iz}} \tag{6.21}$$

6.3 Bulk plasma considerations

We assume a Maxwellian distribution for the centre and the edge, and parabolic profiles for the temperature and electron densities described in eqs. (3.33) and (3.34).

Neutrals that are not ionised in the SOL enter the plasma volume, and similar to (6.18) the mean free path for CX at a given r is proportional to:

$$\lambda_{cx}(v) \propto \frac{1}{n_e(r)\sigma_{cx}(v)\hat{f}(v,r)dv} \tag{6.22}$$

with $\hat{f}(v,r)$ the normalised Maxwellian distribution described by:

$$\hat{f}(v,r) = [\frac{m_D}{2\pi kT(r)}]^{0.5} e^{-\frac{m_D v^2}{2kT(r)}} \tag{6.23}$$

After transformation to energy the probability of a CX process occurring in the region $(r, r+dr)$ is given by the following:

$$\begin{aligned} P_{cx}(v,r)drdv &\propto \frac{drdv}{\lambda_{cx}(v)} \\ P_{cx}(E,r)dEdr &\propto \frac{\sigma_{cx}(E)}{\sqrt{2m_D}} n_e(r)\hat{f}(E,r)E^{-0.5}dEdr \end{aligned} \tag{6.24}$$

The total probability is then given by:

$$\begin{aligned} P_{cx}(E)dE \propto \frac{n_e(0)}{2}\frac{1}{\sqrt{\pi kT(0)}} E^{-0.5}\sigma_{cx}(E)\int_0^a [1-\frac{r^2}{a^2}]^{(\alpha_n - 0.5\alpha_T)} \\ \exp[\frac{-E}{kT(0)}(1-\frac{r^2}{a^2})^{-\alpha_T}]drdE \end{aligned}$$

and with normalisation

$$P_{cx}(E)dE = \frac{1}{N_{cx}} \cdot \frac{n_e(0)}{2}\frac{1}{\sqrt{\pi kT(0)}} E^{-0.5}\sigma_{cx}(E)I_{ci}(E)dE \tag{6.25}$$

with N_{cx} the normalisation coefficient for the processes in the central parts of the plasma, and I_{ci} the integral over small radius. This is the equation [STR89] for determining the ion temperature of the plasma from the measured CX flux, and N_{cx} is given by:

$$N_{cx} = \frac{n_e(0)}{2} \frac{1}{\sqrt{\pi k T(0)}} \int_0^\infty E^{-0.5} (\sigma_{cx}(E) + \sigma_{iz}) I_{ci}(E) dE \tag{6.26}$$

This results in the total probability of CX in the plasma:

$$P_{cx}(E)dE = \frac{\sigma_{cx}(E) E^{-0.5} I_{ci}(E) dE}{\int_0^\infty (\sigma_{cx}(E) + \sigma_{iz}(E)) E^{-0.5} I_{ci}(E) dE} \tag{6.27}$$

Similarly the probability P_{iz} is given by:

$$P_{iz}(E)dE = \frac{\sigma_{iz}(E) E^{-0.5} I_{ci}(E) dE}{\int_0^\infty (\sigma_{cx}(E) + \sigma_{iz}(E)) E^{-0.5} I_{ci}(E) dE} \tag{6.28}$$

From these relations, eqs. (6.20), (6.21), (6.27) and (6.28), the total CX flux, with energy dependence through $B(E)$, can be obtained numerically. The contribution from the edge has been found to be a small effect.

The reaction cross section for CX used in the calculations was [GRE84]:

$$\sigma_{cx} = (7.07 - 1.83 \log_{10} v)^2 \tag{6.29}$$

For the reaction rate $\langle \sigma v \rangle_{cx}$ a power fit was made to the data by Harrison [HAR83] and the following expression was used:

$$\langle \sigma v \rangle_{cx} = 1 \cdot 10^{-8} T(r)^{0.33} \qquad \text{cm}^3/\text{s} \tag{6.30}$$

For the electron ionisation cross sections the analytical expressions from the work of Bell [BEL82] was used.

6.4 Results

The resulting equations were used to simulate CX spectra for specific plasma conditions in the JET tokamak. The measured plasma parameters and the geometry of JET were used as input for the model calculation.

Directly measured spectra were obtained from JET from stripping cell measurements [COR89] for comparison. The discharge used was # 16952 with $T(0) = 3$ keV and $n_e(0) = 5 \cdot 10^{13}$ cm^{-3}. The other plasma parameters used are shown in the caption to Fig. 6.8 where the model is compared to the measured spectrum. The references are also indicated for the values accepted. The correlation to this spectrum is good with the particle confinement time τ_p assumed to be 0.4 s. The shape and also the absolute quantitites of the spectra compare reasonably to the actual data. The value of $\tau_p = 0.4$ s is also realistic when compared to the scaling of Stangeby and McCracken [STA90] of particle confinement time with mean density for JET.

The good comparison with the experimental values from JET shows that the assumptions of the model are valid for determining the CX flux to the wall of a tokamak such as JET. Also calculated was the CX flux for a device like ITER and the expected contribution to fusion reactions in the walls of ITER by CX neutral fluxes during ohmic heating phases (section 7). The conceptual parameters of ITER were used for the model calculation and the resulting spectrum is shown in Fig. 6.9. The large increase in the absolute amount and the average energy of the fluxes indicated the expected increase of the wall load due to the increased power loss from CX neutrals.

This wall load was calculated with the model results and the load on the walls is ~ 2 MW/m^2. The effect of sputtering can also be obtained for this flux and this was modelled for deuterium and tritium on carbon, resulting in a global sputtering tempo of $2 \cdot 10^{22}$ atoms/s. If the screening factor is 0.05, the density of the plasma would increase by $1 \cdot 10^{12}$ atoms/s cm^3. This shows that the effect of the CX neutrals would need to be further studied to avoid impurity problems in a reactor such as ITER.

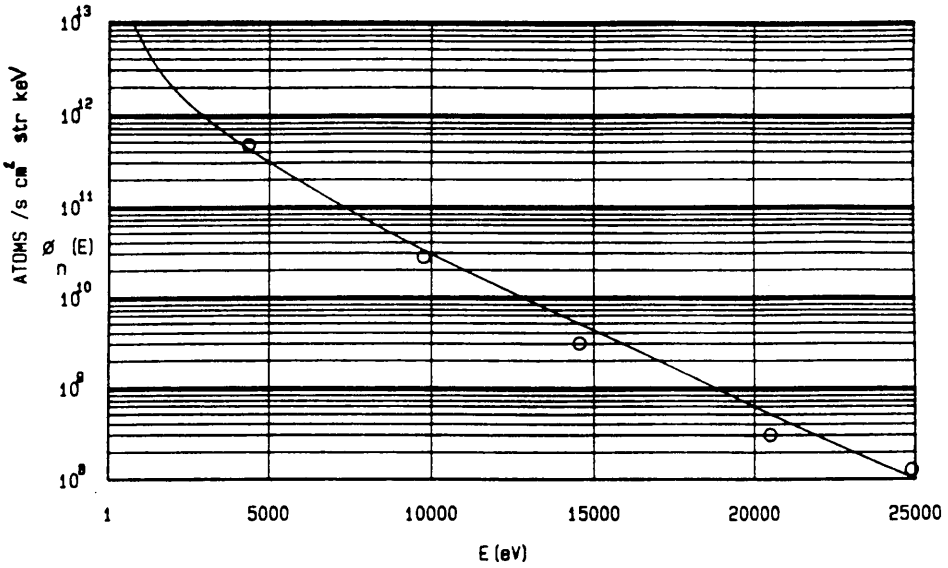

To = 3000 eV
Te = 50 eV
N_0 = 5 x 10^{13} cm^{-3}
N_e = 4 x 10^{12} cm^{-3}
D_t = 4000 cm^2/s
L_c = 4000 cm
V_d = 10 eV
R = 0.90 (STA 90)
R_1 = 1.0
V = 200 m^3
A = 200 m^2
τ_p = 0.4 s (STA 90)

α_T = 1.0

α_n = 0.6

Figure 6.8: **CX flux comparison of the model to measured flux. The solid line is the model simulation, with experimental points.**

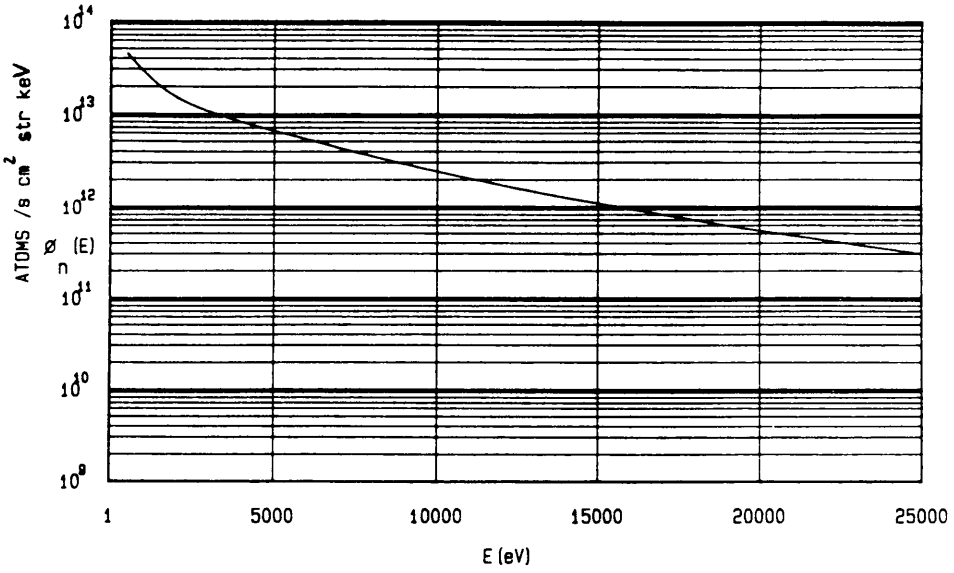

R = 6 m
a = 2.15 m
T_o = 12000 eV
T_e = 100 eV
N_o = 2×10^{14} cm^{-3}
N_e = 4×10^{13} cm^{-3}
D = 4000 cm^2/s
L_c = 8000 cm
V_d = 40 eV
R = 0.90 R_1 = 1.0
τ_p = 1.8 $= \tau_E$
V = 800 m^3, A = 500 m^2

α_T = 1.0
α_n = 0.4

Figure 6.9: **CX flux as calculated for typical ITER operational conditions. The plasma parameters are indicated.**

Chapter 7

Fusion processes in the limiters and walls of a tokamak

7.1 Introduction

In a tokamak like JET a large number of discharges are studied per annum ($\sim$ 3 000), and the upper layers of the limiters and walls are constantly bombarded with deuterium ions and neutrals. All the major tokamaks in the world now have low Z materials as plasma-facing components, especially carbon and beryllium. The choice of low Z materials are mainly because higher concentrations of these materials can be allowed in the plasma compared to high Z materials, of which the radiation losses in the plasma severely limit the concentration in the plasma. One of the main characteristics of especially carbon is the high retention of hydrogen and its isotopes in the limiter and wall material, up to 40 atomic % [BEH87] with beryllium also showing the same tendency, although not to the same extent. The retention of deuterium and tritium in a D,T reactor have serious consequences for the of the tritiuminventory. The upper layers have been shown to be rich in deuterium by analyses [BEH87] of the wall and limiter material for deuterium discharges.

In a deuterium plasma there is a constant flux of deuterium ions to the limiters and neutrals to the walls and limiters during a discharge. Bombardment of the fuel-rich layers of the walls and limiters by these particles can lead to a fusion reaction yield during the discharge. The energies of the ions leaving the plasma are mainly determined by the plasma edge temperature, which is normally less than 1 keV. Assuming that ICRH heating effects such as described in chapter 5 do not heat the edge plasma excessively, these ions will not contribute substantially to fusion reactions in the limiter material. Escaping charge exchange neutrals, on the

other hand, preserve the plasma temperature distribution and lead to high energy bombardment of the limiters and walls. This can be viewed as a high energy tail in the neutral energy spectrum. The addition of auxiliary heating with neutral beam injection (NBI) increases the energy of this tail, further increasing the fusion reaction rate due to the bombardment of the deuterium-rich layers. This section describes the importance of the plasma limiters and vessel walls to the fusion processes in deuterium plasmas in JET and in a reactor.

The reaction of interest is the production of tritium from DD reactions. The cross section for the neutron producing reaction (1.2) is approximately the same for typical plasma ion energies, with the branching ratio of the two reactions ~ 0.5. The cross sections are negligible below 3 keV, increasing strongly with higher energy, peaking at energies in excess of 1 000 keV. At higher energies the cross section decreases weakly. The interest in this study arose because of the energy distribution of the charge exchange neutral flux to the walls and the energy of the neutral particles injected during auxiliary heating phases. The beam energy used was 80 keV, enhancing the energy of the neutral flux to the wall substantially up to 80 keV.

The reaction products, or ash, of reactions (1.3) and (1.2) are protons and tritons, and neutrons and ^{3}He respectively. The neutrons leave the plasma losing little of their energy, but the other nuclei are deposited in the limiter and wall material of the tokamak as the fusion processes in the plasma itself lead to an ion flux, mainly to the limiters, that consists partly of these ash nuclei. The flux of neutral particles undergoing resonant charge exchange reactions consists mainly of deuterium, and leads to deposition on and implantation into the walls and limiters. During this dynamic process hydrogen isotopes in the wall can be desorbed by the particle and heat flux, with a fraction of the flux being reflected back to the plasma. This leads to an equilibrium distribution of the ash and fuel in the wall and in the limiters.

One of the diagnostics of measuring the fusion yield in JET, like many other tokamaks, is the measurement of the flux of neutrons from the tokamak. The reaction yield of neutrons and tritons is similar, indicating that the measured neutron yield should correspond to the triton yield in the walls and limiters, plus the number of tritons pumped from the plasma chamber. The measurement of tritium in the wall material therefore lends itself to the determination of the fraction of the fusion yield that remains in the walls.

The location of the tritium is important with respect to the inventory of ash in deuterium plasmas, and also with a view to the use of tritium as part of the plasma fuel. There has been considerable effort [SAR90] to find out where the tritium is located.

The total amount and depth profile of tritium in the walls of the JET tokamak had previously been obtained [GOO88] and showed that the tritium content peaks

at a depth of approximately 6 μm. This is surprising as the origin of the tritium should mainly be from the bulk plasma, where tritium ions are generated from fusion processes. These ions gyrate through the plasma and some of them are lost from the confining magnetic field. Some ions are then implanted inside the walls and limiters of the vessel.

This should, however, lead to a very shallow peak in the depth profile of the tritium content, as the angles of incidence of these ions are glancing with respect to the limiters and walls, leading to the tritium being trapped close to the surface. One possible other source for the tritium is from DD fusion processes inside the walls of the tokamak as energetic (10 keV to 200 keV) deuterium neutrals impinge on the walls and create a buildup of tritium inside the wall, or from the large flux of ions hitting the limiters. It is possible to obtain this contribution by simulating such a process mathematically. The fluxes of neutral deuterium atoms to the walls are routinely measured on JET as a function of energy and angle of incidence, and these fluxes can be used to simulate fusion processes in the walls of JET. The profile of the measured tritium indicates that this contribution might be more important than previously believed. The aim of the current study was to determine, with the aid of an analytical model, the contribution of the fusion reaction yield that is the result of reactions in the walls, compared with the fusion yield from the plasma.

7.2 Fusion processes in the limiters

The number of fuel particles (N_{Lim}) (mainly ions) that hit the limiters per unit time during a discharge can be estimated to be:

$$N_{Lim} = \frac{\bar{n}V}{\tau_p}$$

where $\bar{n}$ is the mean density of fuel particles, V is the plasma volume and τ_p is the particle confinement time. This rate is of the order of 10^{22} particles per second for a typical JET discharge, which is extremely high and may lead to significant fusion rates.

The fusion reaction rate from reaction (1.3) is then given by:

$$R_{Lim} = N_{Lim}\rho_D \int_0^{E_{max}} \hat{f}_e(E_0) \int_0^{E_0} \frac{\sigma(E)}{S(E)} dE dE_0 \qquad (7.1)$$

with ρ_D the atomic concentration of deuterium atoms in the upper layers of the limiter ($\approx 10^{23} cm^3$ [COA89]) and $\hat{f}_e(E_0)$ is the distribution function for the ions

impinging on the limiter. In general we shall have ρ(x), the deuterium concentration a function of depth, but here it is assumed constant. $\sigma(E)$ is the cross section for the reaction and S(E) is the stopping of the ions in the limiter material. For the purpose of this study consideration was given to the limiters of JET during the carbon phase, i.e. when the wall material and limiter material consisted mainly of carbon.

Using eq. (7.1) and for extrapolation of the functional fit [KRA87] to the cross section to typical edge energies (50 - 100 eV), the fusion yield is found to be negligible. The reaction rate for an edge plasma with a Maxwellian velocity distribution, with a temperature of 50 eV, is $\approx 2 \cdot 10^{-27}$ reactions per second, and even with an unrealistic edge temperature of 5 keV the reaction rate is $\approx 2 \cdot 10^{-7}$ reactions per second.

7.3 Fusion processes in the walls - depth distribution

Fusion processes in the walls of a limiter plasma can be ascribed to neutral deuterium particles leaving the plasma and hitting the walls at high enough energies for fusion to take place. The largest proportion of these neutral fluxes originate from charge exchange processes in the plasma. Measurement of neutral fluxes on JET are made routinely through the use of a stripping cell [ROQ85]. During normal ohmic discharges the energies of these neutrals, mainly from charge exchange processes, are low (representing the bulk energy distribution of the plasma ions and the plasma temperature) and they should not contribute much to fusion processes. The interesting phase, however, is during NBI, when 80 keV neutral deuterium is shot into the plasma. During this phase a high flux of high-energy deuterium atoms leave the plasma and hit the walls and limiters.

7.3.1 Depth profile of reactions in the wall

We assume that the escaping deuterium atoms enter the limiters and walls and have a probability to undergo fusion reactions with deuterium atoms resident in the wall and limiters.

The geometry used to analyze the problem is shown in Fig. 7.1. Deuterium is shown impinging with an energy E_0 on the surface with an angle Θ to the normal of the surface. At a depth x_1 a fusion reaction occurs, and the tritium product is emitted at an angle $\phi + \Theta$ with respect to the normal of the surface, and come to rest at a

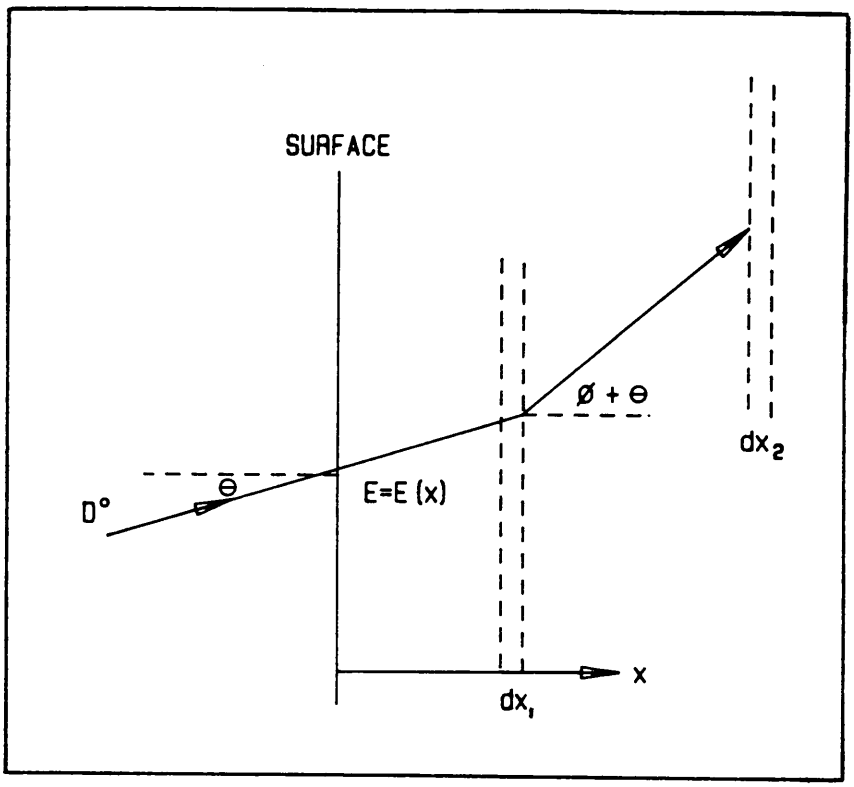

Figure 7.1: **The geometry used with deuterium impinging with an energy E_0 on the surface at an angle Θ to the normal of the surface**

depth x_2.

Under the assumption [ZIE77] that the stopping of deuterons ($E_d \leq 100$ keV) is linear with velocity, and is the same as for protons with the same velocity, we can write:

$$\frac{dE}{dx'} = \frac{dE}{dx_1} cos(\Theta) = -k\sqrt{E} \tag{7.2}$$

Solving this differential equation one obtains:

$$\sqrt{E} = \frac{-k}{2cos(\Theta)} x_1 + \text{constant} \tag{7.3}$$

The constant is found to be $\sqrt{E_0}$ from the initial conditions at $x = 0$, with E_0 the impinging energy. The energy as a function of incoming angle and depth normal to the surface is:

$$E(x_1, \Theta) = [\sqrt{E_0} - \frac{k}{2cos(\Theta)} x_1]^2 \tag{7.4}$$

The tritium produced in the depth interval dx_1 is emitted in all directions $\phi + \Theta$ with the energy defined by the kinematics of the reaction. This relationship is given by [PEA86]:

$$E_T(E, \phi) = E m_D \frac{m_T}{(m_T + m_p)^2} [2cos^2(\phi) + \eta(E) + 2cos(\phi)[cos^2(\phi) + \eta(E)]^{0.5}] \tag{7.5}$$

with

$$\eta(E) = m_p \frac{(m_p + m_t)}{(m_D + m_T)} [\frac{Q}{E} + 1 - \frac{m_D}{m_p}]$$

and E the incoming deuteron energy given by eq. (7.3) with the masses of the particles as indicated. The energies of the emitted tritium ions range from 650 to 1500 keV over all angles of emission (for $E < 100$ keV) and the range of tritium ($R_T(E, \phi)$) at these energies can be approximated as having exponential dependencies with energies.

The exponential function fitted to the data of Ziegler [ZIE77] is:

$$R_T(E, \phi) = 3.97 e^{\frac{1.14 \cdot 10^{-3}}{3} E_T(E, \phi)} \tag{7.6}$$

where $R_T(E, \phi)$ is in keV/μm and $E_T(E, \phi)$ in keV. In the construction of (7.6) the range of tritons was scaled to the range of protons with the same velocity.

The final distribution is dependent on the depth of interaction, with the projection of the range added on the depth axis:

$$x_2(E, \phi, \Theta) = x_1(E, \Theta) + R_T(E, \phi) cos(\phi + \Theta) \tag{7.7}$$

and from (7.4):

$$x_2(E, \phi, \Theta) = \frac{2cos(\Theta)}{k} (\sqrt{E_0} - \sqrt{E}) + R_T(E, \phi) cos(\phi + \Theta) \tag{7.8}$$

This relation must then be integrated over a realistic range of θ and ϕ.

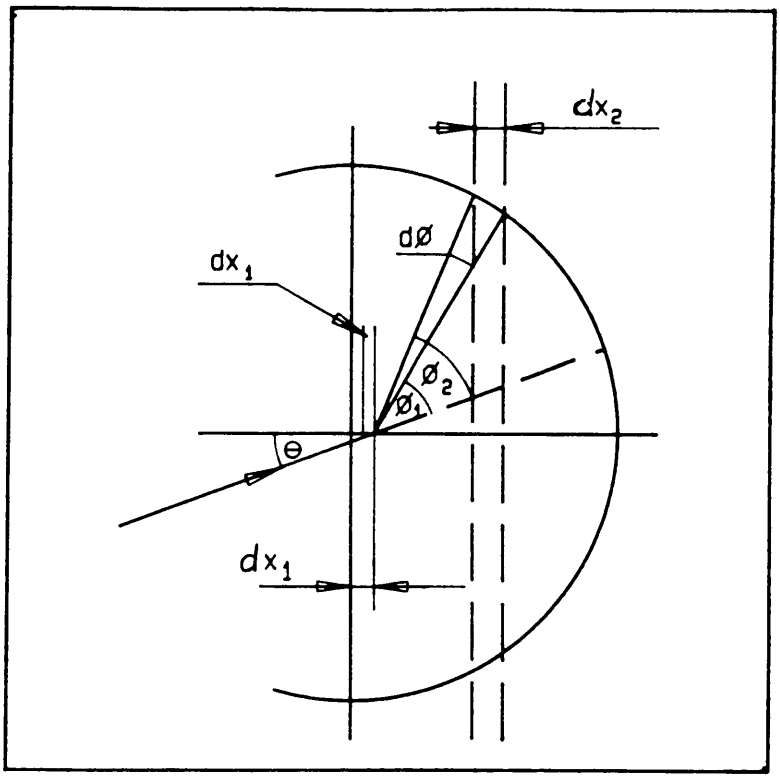

Figure 7.2: **The geometry used for determining the probability of a DD reaction**

7.3.2 Probability of a reaction in the wall

The probability of a reaction can be calculated with the help of the geometry in Fig. 7.2. With the only interest the depth distribution of the produced tritium, the geometry is simplified to be planar. The probability $N_T(E, \phi, d\phi)$ of the realisation of a reaction in the wall in the depth interval dx_1, with emission of tritium into the angle cone $d\phi$, due to a deuterium atom with an energy of E is:

$$N_T(E, \phi, d\phi) = \rho_D \sigma(E, \phi) \frac{dx_1}{cos(\Theta)} \frac{d\phi}{2\pi} \tag{7.9}$$

where ρ_D is the concentration of target atoms, i.e. deuterium atoms in the wall, assumed to be constant. $\frac{d\phi}{2\pi}$ was introduced as the normalisation factor over all angles of emission of reaction products assuming isotropic emission of reaction products. For the carbon limiters in JET, during the carbon phase, $\rho_D \approx 10^{23}$ atoms/cm^3 [COA89]. $\sigma(E, \phi)$ is the cross section of reaction (1.3).

7.3.3 The cross section for the reaction

The cross section for the reaction of incident deuterium atoms with deuterium atoms in the wall must be evaluated at the centre of mass angles and energies, as the assumption of [KRA87] is that the emission of reaction products is isotropic in the centre of mass frame.

In the centre of mass frame the following relations are valid [PEA86]:

$$E = \frac{m_D + m_D}{m_D} E_{CM} = 2E_{CM} \tag{7.10}$$

and

$$\phi = arctan[\frac{sin(\phi_{CM})}{cos(\phi_{CM} + \gamma_b(E_{CM}))}] \tag{7.11}$$

with

$$\gamma_b(E_{CM}) = [\frac{m_T}{m_P}\frac{E_{CM}}{E_{CM} + \epsilon_{DD}}]^{0.5} \tag{7.12}$$

where ϵ_{DD} is the energy release per reaction.

The cross section in the laboratory frame is related to the values in the centre of mass frame by [PEA86]:

$$\sigma(\phi) = \frac{[1 + 2\gamma_b(E_{CM})cos(\phi) + \gamma_b(E_{CM})^2]^{1.5}}{1 + \gamma_b(E_{CM})cos(\phi)}\sigma(\phi_{CM}) \tag{7.13}$$

The isotropic reaction cross section is described by a Gamov function, fitted to the following expression [ROT90,KRA87] in the centre of mass frame:

$$\sigma(E_{CM}) = \frac{S_\sigma(E_{CM})}{E_{CM}} e^{\frac{-C}{\sqrt{E_{CM}}}} \tag{7.14}$$

with $S_\sigma(E_{CM})$ and C constants in the energy range 1 keV to 100 keV, which is the range of interest in this analysis. The constants have the values:

$$S_\sigma(E_{CM}) \approx 55\text{keV barn} \tag{7.15}$$

$$C \approx 31.39\sqrt{\text{keV}} \tag{7.16}$$

for E_{CM} in keV. The cross section is valid at least down to $E_d = 3$ keV ($E_{CM} = 1.5$ keV) [ROT90].

After transformation to laboratory parameters, for isotropic emission of the reaction products in the centre of mass frame and with emittance angle of tritium (ϕ) defined as in Fig. 7.2, we find:

$$\sigma(E,\phi) = \frac{2(1+2\gamma_b(E)cos(\phi)+\gamma_b(E)^2)^{\frac{3}{2}}}{1+\gamma_b(E)cos(\phi)} \frac{S_\sigma}{E} e^{-C\sqrt{\frac{2}{E}}} \tag{7.17}$$

It is now preferable to transform the depth interval dx_1 in (7.9) to an energy interval dE through the use of (7.2):

$$dx_1 = -\frac{cos(\Theta)}{k\sqrt{E}} dE \tag{7.18}$$

The negative sign is converted to positive when the energy is increased instead of decreased. Then we can write the reaction probability as:

$$N_T(E,\phi,d\phi) = \rho \frac{(1+2\gamma_b(\frac{E}{2})cos(\phi)+\gamma_b(\frac{E}{2})^2)^{\frac{3}{2}}}{\pi(1+\gamma_b(\frac{E}{2})cos(\phi))} \frac{S_\sigma}{k} E^{-1.5} e^{-C\sqrt{\frac{2}{E}}} dE d\phi \tag{7.19}$$

It is also preferable to transform $d\phi$ to dx_2, which is a fixed depth interval in which the tritium comes to rest. With the geometry of Fig. 7.3 we get:

$$cos(\phi_2+\Theta) = \frac{x_2-x_1}{R_T(E,\phi_2)} \pm \frac{dx_2}{R_T(E,\phi_2)} \tag{7.20}$$

where the + sign is used for $\phi+\Theta > \pi$, and the - sign for $\phi+\Theta \leq \pi$ and

$$cos(\phi_1+\Theta) = \frac{x_2-x_1}{R_T(E,\phi_1)} \tag{7.21}$$

For small $d\phi$: $R_T(E,\phi_1) \sim R_T(E,\phi_2)$ and this reduces to:

$$d\phi_2(E,\phi,\Theta) = acos[cos(\phi_1+\Theta) \pm \frac{dx_2}{R_T(E,\phi_1)}] - \Theta - \phi_1 \tag{7.22}$$

This $d\phi(E,\phi,\Theta)$ must now be substituted in (7.19) with the final result:

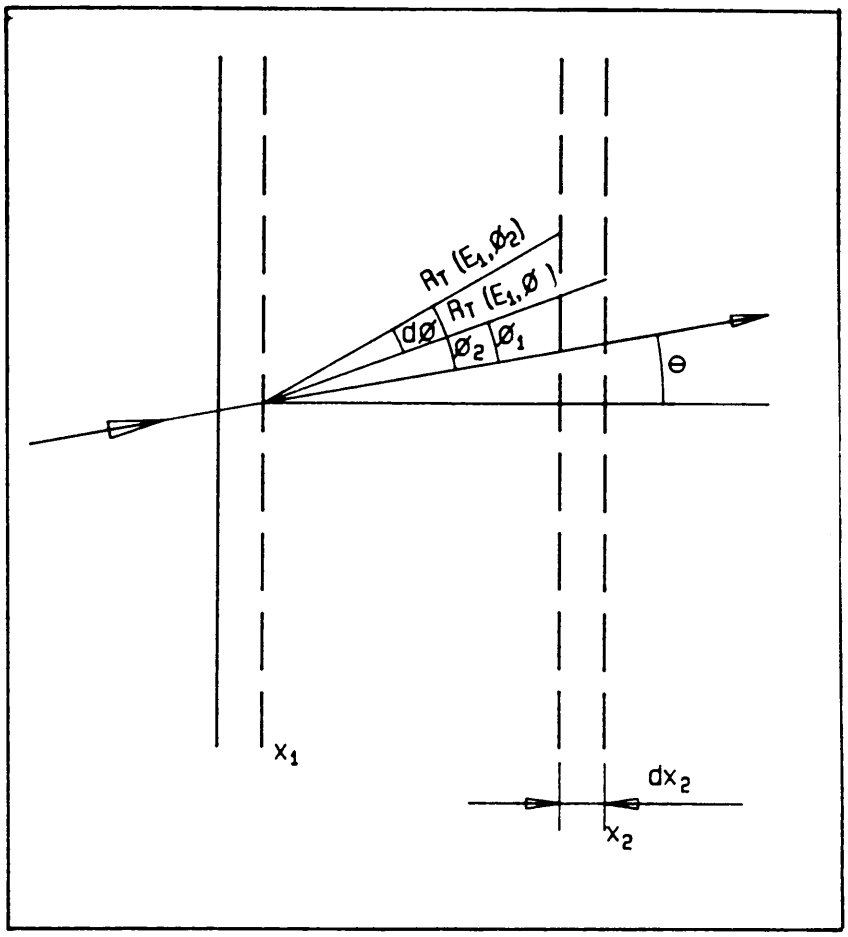

Figure 7.3: **The geometry used to determine the position of tritium produced in the wall**

$$N_T(E,\phi,\Theta,dx_2) = \rho\frac{(1+2\gamma_b(E)cos(\phi)+\gamma_b(E)^2)^{\frac{3}{2}}}{\pi(1+\gamma_b(E)cos(\phi))}\frac{S_\sigma}{k}E^{-1.5}e^{-C\sqrt{\frac{2}{E}}} \quad (7.23)$$

$$[acos[cos(\phi_1+\Theta)\pm\frac{dx_2}{R_T(E,\phi_1)}]-\Theta-\phi_1]dE \quad (7.24)$$

and the tritium so produced comes to rest at the depth $x_2(E,\phi,\Theta)$ described by (7.8).

For $E_{CM} \ll Q$ the following assumptions can be made:

$$\gamma_b \simeq 0 \quad (7.25)$$

which is similar to:

$$\phi \simeq \phi_{CM} \quad (7.26)$$

This is valid for incident energies $E \leq 100$ keV ($E_{CM} \leq 50$ keV), as the ϵ-value for the reaction is 4 032 keV. The largest error for this approximation is at $E_d = 100$ keV, with the reaction product emitted at an angle $\phi = \frac{\pi}{2}$, being 12 % in this extreme case.

These equations could only be solved numerically, and a program was written in MATHCAD to solve the problem. The results are discussed in section 7.4.1. $N_T(E,\phi,\Theta,dx_2)$ only gives the reaction probability for a given particle impinging with energy E_0 onto the target with angle Θ. The energy and angle spectrum of the neutral fluxes must be folded into these values. From earlier measurements [VER89] a near cosine distribution was obtained over the angle Θ. With this assumption and the spectrum of the flux at $\Theta = 0$, which is the angle at which these spectra are measured, the final absolute number of tritium particles coming to rest at x_2 is:

$$N_{Total}(E,\phi,\Theta,dx_2) = N_T(E,\phi,\Theta,dx_2)\Gamma(E_0)cos(\Theta) \quad (7.27)$$

where $\Gamma(E_0)$ is the measured flux function.

7.4 Fusion processes in the walls - total number of reactions

The problem of obtaining the total number of fusion reactions in the wall can be solved analytically for a given energy and incident angle. This problem was treated separately. The aim was to obtain the number of reactions during a single representative discharge, and to compare the contribution due to fusion in the walls to the total fusion yield from the discharge, and the fusion yield of a whole discharge campaign.

As the incident angle is not important in this case, this angle is averaged over, and the analysis is done for a deuterium atom with energy E_0 impinging onto the wall. The stopping is described by (7.4) which is now written as:

$$E(x) = [\sqrt{E_0} - \frac{k}{2}x]^2 \tag{7.28}$$

This gives the maximum penetration depth as:

$$x_{max} = \frac{2\sqrt{E_0}}{k} \tag{7.29}$$

Using eqs. (7.10) and (7.14) the cross section now becomes:

$$\sigma(E(x)) = \frac{2S_\sigma(\frac{E(x)}{2})}{E(x)e^{\frac{C}{\sqrt{E(x)/2}}}} \tag{7.30}$$

and the total reaction probability is given by:

$$R(x) = \int_0^{x_{max}} \rho\sigma(E(x))dx \tag{7.31}$$

From (7.28) and (7.30) we find:

$$R(x) = 2\rho S_\sigma \int_0^{x_{max}} \frac{1}{[\sqrt{E_0} - \frac{k}{2}x]^2} e^{-\frac{C\sqrt{2}}{\sqrt{E_0}-\frac{k}{2}x}} dx \tag{7.32}$$

With the substitution:

$$y = -\frac{\sqrt{2}}{kC} e^{-\frac{\sqrt{2}C}{\sqrt{E_0}-\frac{k}{2}x}} \tag{7.33}$$

it is easy to obtain:

$$R(E_0) = \frac{2\sqrt{2}\rho S_\sigma}{kC} e^{-\frac{\sqrt{2}C}{\sqrt{E_0}}} \tag{7.34}$$

We now use eq. (7.16) to obtain:

$$R(E_0) = \frac{5 \cdot 10^{-24}\rho}{k} e^{-\frac{44.4}{\sqrt{E_0}}} \tag{7.35}$$

with E_0 in keV. This equation gives the probability for a fusion reaction in the wall from an impinging ion with energy E_0.

The total reaction rate per unit area is obtained from the expression:

$$R_{tot} = \int_0^\infty \Gamma(E_0) R(E_0) \Omega dE_\alpha$$

in reactions/s·cm^2, where $\Gamma(E_0)$ is the flux function for the deuterium and Ω is the contribution from space considerations assuming a cosine distribution for the flux.

The value for k was obtained by assuming that the wall consisted of a layer containing 0.4 atoms deuterium per carbon atom. From the coefficients [ZIE77] for pure carbon and hydrogen, and the use of Bragg's rule (linear additivity) one can obtain the value of k to be:

$$k = 3.136 \frac{\sqrt{\text{eV}}}{10^{15}\text{atoms/cm}^2}$$

To obtain the stopping in keV/μm, a multiplication factor of 11.36 $\frac{10^{18}\text{atoms/cm}^2}{\mu m}$ was used, and with the assumption that the stopping of a deuteron is the same as for a proton with half the energy, the final value for k was obtained:

$$k_{a-C:D} = 25.19 \frac{\sqrt{keV}}{\mu m}$$

7.4.1 Comparison of experimental and calculated results

The results were obtained for a suitable discharge (#16 952) of JET of which measured spectra were obtained for the flat-top part of the discharge. First a spectrum

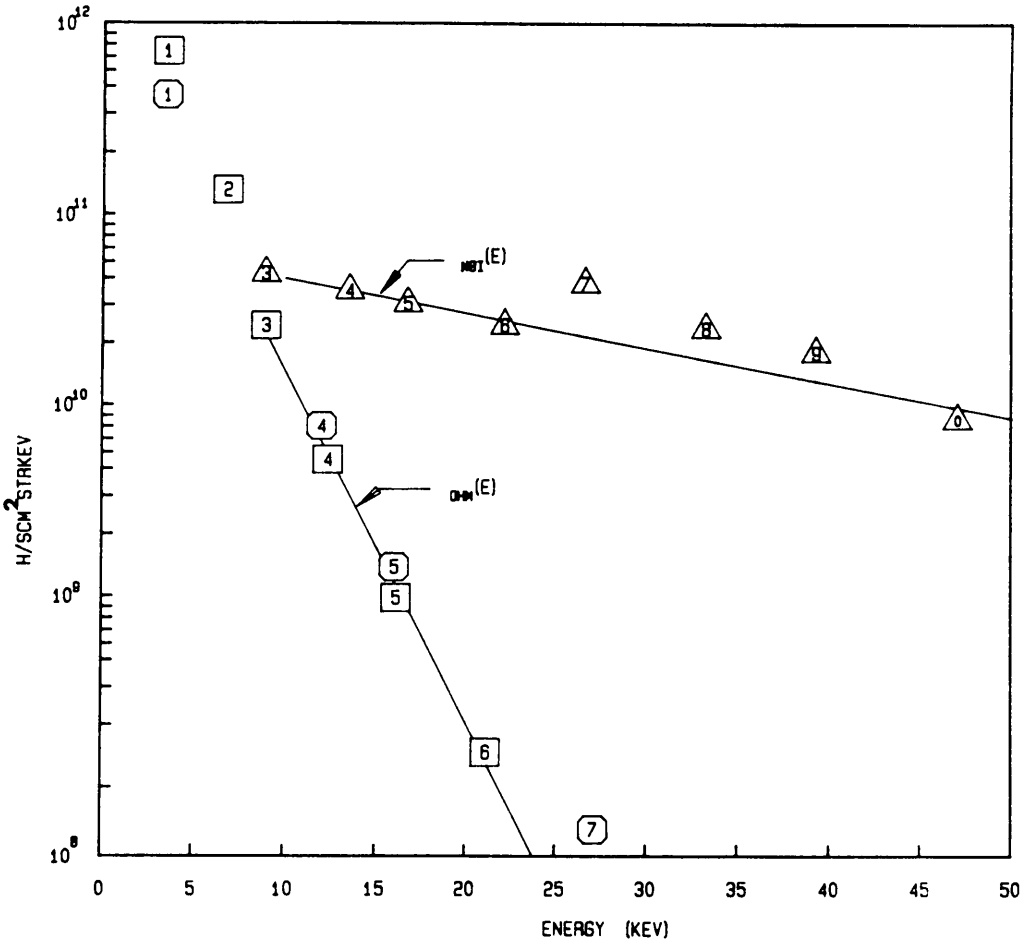

Figure 7.4: **Measured spectra of the neutral particle flux to the wall of a tokamak during ohmic heating and during NBI [COR89]**

was obtained for the part of the discharge where only ohmic power was used as input, and finally a spectrum was obtained during the NBI phase. These spectra are shown in Fig. 7.4.

The high energy tails of these spectra were fitted to exponential functions, which are the lines drawn in Fig. 7.4, and the two functions are:

Ohmic:

$$\Gamma_{ohm}(E) = 7.04 \cdot 10^{11} e^{-0.3667E}$$

and NBI:

$$\Gamma_{NBI}(E) = 6.78 \cdot 10^{10} e^{-0.0387E}$$

with the energy E in keV and Γ(E) in atoms/(cm^2·sr·s·keV), the units in which these spectra are experimentally determined. The respective ion temperatures T_i obtained from these fits were 2.7 keV and 25 keV (T_e was 2 keV and 2.5 keV respectively). It is clear from Fig. 7.4 that the high-energy tail of the ohmic part of the discharge is dramatically smaller than the corresponding NBI tail. This already suggests that the fusion yields will differ quite a lot. The NBI-high energy tail is solely due to the presence of high-energy primary neutrals which are injected into the plasma.

The depth distribution was obtained for the NBI part of the discharge with the use of eq. (7.27), and the results are indicated in Fig. 7.5. The measured depth dependence [GOO88] is also indicated (broken line) with the Y - axis on a relative scale.

The comparison is good when it is considered that the measurement of the tritium present in the wall is done after a large number of discharges ($\sim$ 3 000) of very variable nature. The latter may also account for the fact that the profile is much more smeared out, even though the depth resolution of the measurement was not very good. This result suggests that the fusion in the wall phenomenon may be responsible for the bulk of the tritium present in the wall, and not from tritium produced in the plasma volume and lost to the walls.

The next step was to calculate the total fusion yield due to the walls. The number of neutrons observed in the discharges, the neutral particle flux and the total amount of tritium measured after a campaign are all known [GOO88], and the calculated numbers can be compared with the experimental values which were obtained independent of the origin of the reaction. The comparison between these values would indicate the importance of the walls to the fusion yield.

The numerical result for production of tritons as a function of incoming energy is shown in Fig. 7.6, where the vertical axis indicate the number of reactions at the

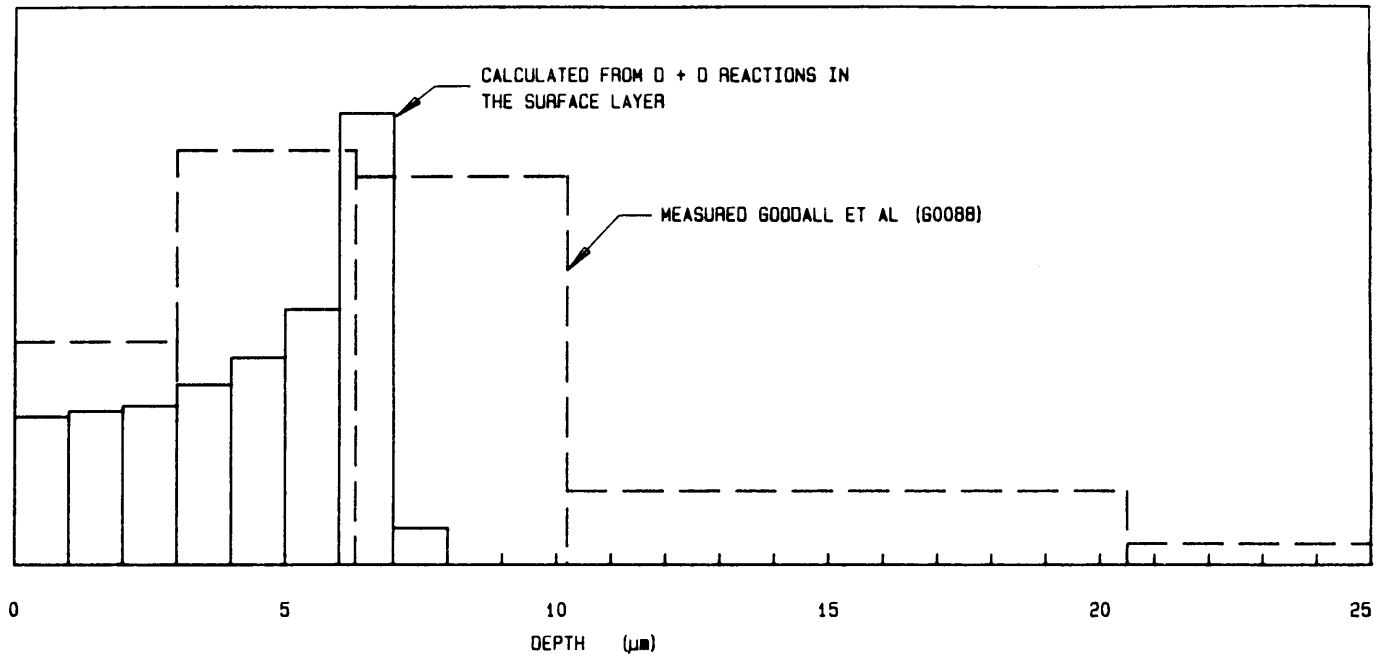

Figure 7.5: **The depth distribution obtained for the NBI part of the discharge. The measured depth dependence [GOO88] is also indicated (broken line) with the Y-axis on a relative scale.**

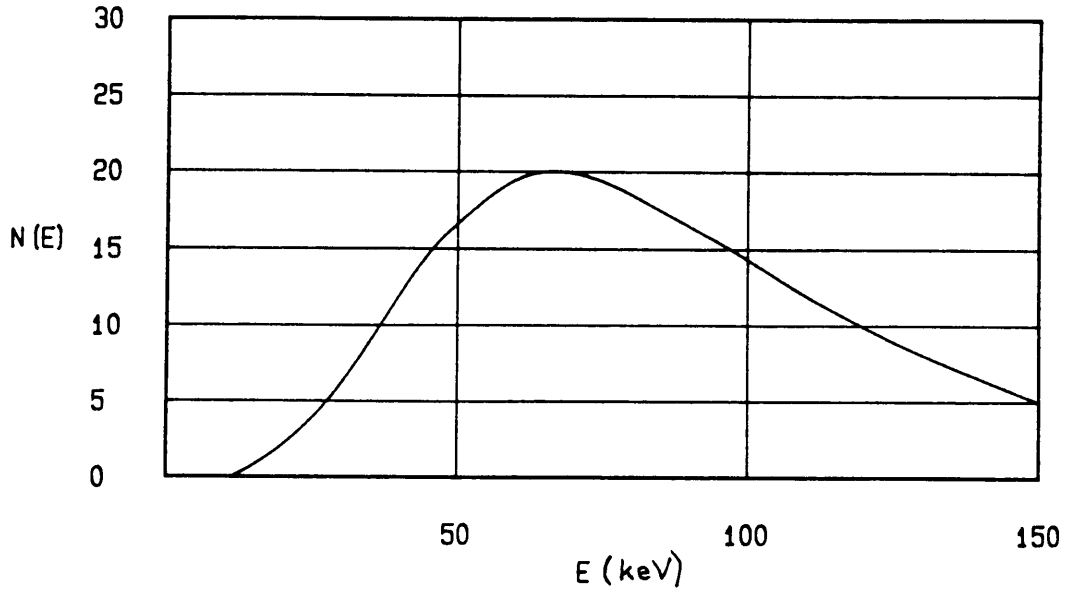

Figure 7.6: **The number of reactions as a function of incoming energy for the CX flux measured in JET, and the DD reaction**

specific energy. The neutral particle flux has already been folded into the results. The curve indicates that the most important energy range is the range from approximately 45 keV to 90 keV. This is exactly the energy range where the neutral fluxes would be excessively high during NBI in the future when the energy of the neutral beams will be raised to 140 keV on JET. This will give rise to higher fluxes of deuterium to the walls, with a higher reaction yield. The integral over all the energies and an assumed cosine distribution over all incident angles yield the expected amount of neutrons.

The contribution of the assumption of a cosine distribution to an integral in space is obtained from the fact that $d\Omega = sin(\Theta)d\Theta d\phi$ and the integral over all values of Θ and ϕ:

$$\Omega = \int_0^{2\pi} \int_0^{\frac{\pi}{2}} cos(\Theta)sin(\Theta)d\Theta d\phi \tag{7.36}$$

With $cos(\Theta)sin(\Theta) = \frac{1}{2}sin(2\Theta)$ it is easy to obtain that:

$\Omega = \pi$

For the ohmic phase the total reaction rate is found to be $3.3{\cdot}10^3$ reactions/m$^2{\cdot}$s which is insignificant. During the NBI phase the total reaction rate was $5.2{\cdot}10^7$ reactions/m$^2{\cdot}$sec. The contribution of this rate to the whole campaign of discharges is not easy to simulate, but during the 1986 campaign [GOO88] 2 800 discharges were fired, and a total of $2.7 \cdot 10^{18}$ was deduced from the total neutron flux. For the sake of this calculation we assumed an average of 2 seconds NBI per discharge. The surface of JET is $\sim$ 200 m^2 and the total tritium produced during the campaign, as calculated in this analysis, was found to be $5.8 \cdot 10^{13}$ tritons. This contributed therefore only $2 \cdot 10^{-3}$ % of the measured tritium production.

A further indication could be found from the total number of neutrons measured for discharge #16 952 and the comparison with the calculated result from the walls. As the branching ratio for the triton producing and neutron-producing reactions is about 50 %, the total number of neutrons calculated was $2 \cdot 10^{10}$, compared to the measured value of $3.5 \cdot 10^{15}$. The contribution of the walls were therefore limited to $6 \cdot 10^{-4}$ % of the total yield.

This result indicates that the similarity of the tritium depth distribution with the distribution expected from wall-related processes must be explained by some other mechanism, as it is highly unlikely that such a small fraction of the tritium produced will play a major role in the depth distribution.

Even when considering that not all the tritium produced in the plasma ends up in the wall does not alter the position much. The tritons produced for the whole campaign, with a retention of 80 % [SAR90], indicate that the tritium content of the walls should be $\sim 1 \cdot 10^{12}$ tritons/cm^2. The content measured differs by a factor of only 10 [GOO88] (being $\sim 10^{11}$ tritons/cm^2), and does not influence the expected impact of wall-related fusion processes much.

Another explanation for the measured tritium depth distribution is to consider the dynamic process of deposition and erosion that takes place in the first layers of the wall surface. This dynamic environment lends itself to areas where tritium can be deposited on the wall surface, to be covered later by carbon.

The problem might be answered with precise data of the tritium depth distribution. A better technique [CAT86] of measuring the depth profile of the tritium would be the use of reaction (1.1) in a nuclear analytical laboratory with an ion accelerator where deuterium is accelerated towards the target containing tritium. This method is sensitive to $\sim 20\mu m$ and has a superior depth resolution of $\sim$ 20 nm. Such

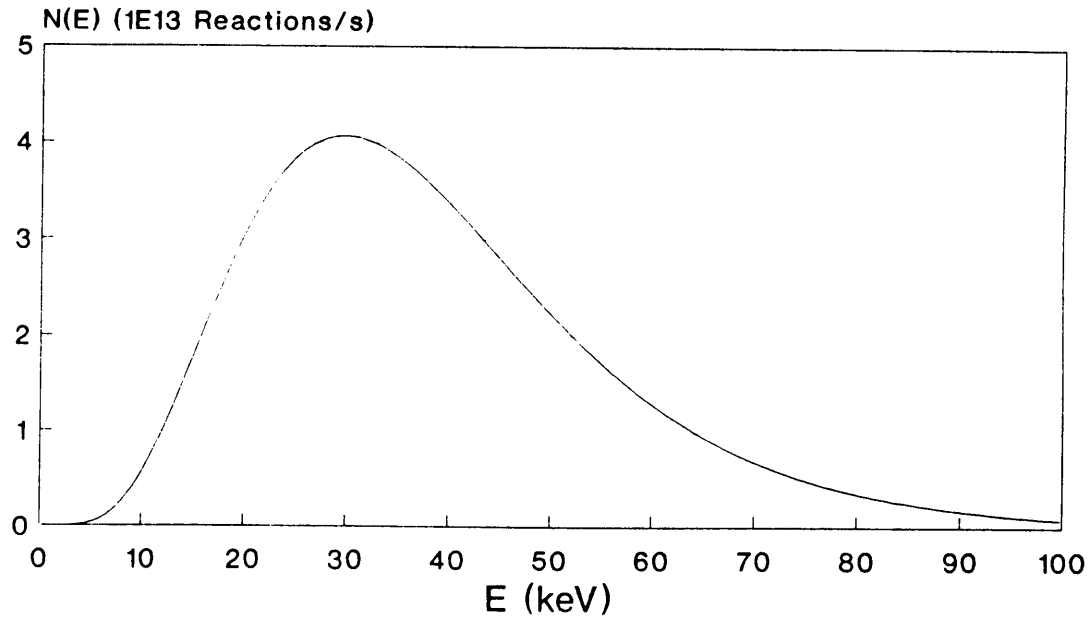

Figure 7.7: **The number of reactions as a function of incoming energy for the CX flux determined for ITER, with the DT reaction**

measurements would be able to identify if the depth distribution corresponds to wall-related processes.

The contribution of the fusion yield in the walls compared with the plasma fusion yield can approximately be determined for typical ITER plasma parameters.This can be done with the aid of the CX flux as a function of energy determined in section 6.4 for ITER operation. With the same analysis as used for the determination of DD reaction rate in the walls, the DT fusion reaction rate can be determined. We assume a D,T plasma with equal concentrations of deuterium and tritium ($\rho_T = \rho_D = 5 \cdot 10^{22}$ atoms/cm^2) in the walls. The fuel is assumed to consist of equal fractions of deuterium and tritium resulting in the CX flux also consisting of equal contributions from the two elements.

With the cross section of the DT reaction, the ITER vessel parameters and for plasma parameters similar to those used in the determination of the CX flux, the rate of fusion reactions in the wall is shown as a function of energy in Fig. 7.7 for the reactor regime, and can be compared to Fig. 7.6 which describes the DD reaction in JET.

The total rate of fusion in the wall is determined to be $\sim 2{\cdot}10^{18}$ reactions per second. This compares with a rate of fusion in the plasma of $\sim 1{\cdot}10^{23}$ reactions per second, indicating that the fusion yield in the wall is only a negligible fraction ($\sim 2{\cdot}10^{-5}$) of the total fusion yield.

This relative decrease of the fusion contribution in the walls can be ascribed to the faster rate of increase of the fusion reaction yield in the plasma with increasing size of the tokamak, compared to the increase of the CX flux as a result of the increase of the volume-to-surface ratio. The indication is, however, that the walls do not contribute significantly to the fusion process in current tokamaks, nor will they do so in future reactors.

Chapter 8

Summary and conclusions

The main emphasis in this thesis is the study of the importance of some aspects of, on the one hand, the negative influence of imperfect confinement of particles and energy, leading to undesirable phenomena in the plasma, such as fuel dilution and enhanced radiation losses from the plasma due to impurities, which directly influence the efficiency of a tokamak reactor. Another crucial parameter used in the study is the energy confinement time, which is the global parameter of establishing ignition and ultimately burn of a plasma. On the other hand, for the helium ash and other impurities in the plasma the imperfect confinement is necessary to keep the plasma from being poisoned by non - fuel nuclei. These aspects are studied theoretically and experimentally, and where appropriate the results are applied to a fusion reactor scenario, mostly to a tokamak similar to ITER.

The criteria for maintaining a steady state burn condition in a reactor by linking the confinement of the helium and energy, which are created in the same position in the plasma volume, shows that steady state burn conditions can only be achieved in a D,T plasma within certain limits of the ratio of helium confinement time to energy confinement time. For other fusion plasmas, like D + ^{3}He, similar bounds exist which are in general more restrictive than in the case of D + T [REI90]. From a zero - dimensional approach this ratio is about 9 for a clean plasma. This maximum ratio decreases sharply when impurities are included in the plasma. When profile effects are added to such a model, this ratio stays to a large extent the same, and even for a limited one - dimensional approach the values are similar. The one - dimensional approach, when compared to an exact solution of the one - dimensional diffusion equations for energy and helium, shows the same qualitative behaviour with limited quantitative interpretation, for typical plasma parameters in a burning fusion plasma.

In such a phenomenological analysis the impurity concentration in the plasma, other

than helium, is normally prescribed. The study of the burn and exhaust criteria is extended in this work to simulate time dependent reactor operation, with impurity generation by the ion flux leaving the plasma, bombarding the divertor material. This study shows the crucial effect of the confinement of these impurities and helium ash in the plasma. When confined for too long in the plasma, the burn is quenched.

The definition of the maximum impurity concentration allowed in the plasma during steady state operation, is normally defined as the impurity concentration where the power produced is equal to the total radiative power lost from the plasma, a non - physical operational condition in the plasma. The approach used in this study to include the exhaust of helium from the plasma, leads to a more restrictive definition, and is compatible with the operation of a reactor in steady state conditions.

Even though the study does not include the real life complex three dimensional geometries and plasma properties, some physical insight is obtained by studying these effects of imperfect confinement.

Experimental results presented, of a study of the ion loss from the plasma and subsequent bombardment of the walls and limiters in JET, show that the erosion and deposition phenomena in the SOL are not well understood and indicated only nett deposition in the SOL, whereas some erosion must also take place at certain positions in the SOL. The measurements were made for the different stages of the plasma discharge, as a function of the radial distance from the plasma volume. Probes were inserted into the edge plasma of JET. These probes were pre - implanted with molybdenum markers at a specific depth to study deposition and erosion processes, and the exposed probes were analysed with nuclear techniques based on the van de Graaff accelerator at Garching.

Further similar studies must be made to check the consistency of such results for different discharge conditions and plasma parameters. This is needed in the light of the crucial aspect of diveror integrity of future fusion devices. Maintenance of the divertor plates in a fusion reactor will be a difficult procedure and therefore the lifetime of the plates are crucial parameters in terms of economics, as well as the creation of impurities that may enter the plasma.

Experimental data presented on the measurement of the creation of abnormally high energy particles in the edge plasma during the application of additional heating by the ICRH (Ion Cyclotron Resonance Heating) method confirms the existence of fast particles in the edge plasma with energies ($\sim$ 1 keV) that roughly corresponds to the maximum of the sputtering yield for typical wall materials, thus contributing dominantly to the higher concentration of impurities in the plasma of ASDEX. This phenomenon also occured at JET, but operation of the ICRH antennaes in the beryllium phase [BUR90] tend to indicate that the problem has been solved to a large extent. Whether the application of beryllium to the plasma chamber will be

a viable concept for reactor operation is still an open question, and the problem of the influx of impurities during ICRH operation may persist in future devices.

The large number of neutral particles that are created in the plasma volume, and are not confined by the magnetic field, are lost from the plasma volume. These particles have several effects on the plasma, such as sputtering of the wall material with subsequent dilution of the plasma fuel as well as radiative losses. A simple model to describe the neutral flux from the plasma volume during ohmic discharges is presented, and the effects of sputtering of the wall material is simulated, for the JET configuration as well as a tokamak like ITER.

A direct effect of the neutrals bombarding the walls and their contribution to the fusion process inside the walls is discussed. The contribution of this process during discharges on JET were considered and found to be negligible when compared to the total fusion yield in the plasma. The same calculation was made for ITER, with the neutral flux obtained in the analysis of section 6. In this calculation the result is of the same order as for JET operation, indicating that the fusion yield in the walls will probably not be significant in future tokamak devices.

While most of the results presented in this thesis can be achieved by use of large computer codes, the simplified analytical treatment presented makes it possible to gain insight into the mechanisms of particle and energy confinement The study aims to focus on some confinement related problem areas in the field of thermonuclear fusion, and some relevant problems and criteria are presented with the aim of furthering the understanding of the mechanisms that control working conditions for a burning tokamak reactor.

Appendix A

The depth distribution in a carbon target as a result of the CX neutral flux measured at ASDEX was calculated using the following:

It was assumed that the particles hitting the probe would penetrate the probe and come to rest at a depth related to the range of the particles, but not at a single depth due to the straggling of the particles in the probe. The distribution was assumed to be Gaussian described by:

$$f(x) = A \exp^{[-\frac{(x-x_0(E))^2}{\Delta_E(E)^2}]} \tag{8.1}$$

with $x_0(E)$ the centre of the implant depth, and $\Delta_E(E)$ the half width of the implant obtained from the straggling function for hydrogen in carbon. This function was obtained from [ZIE77A], by fitting a power function to the data points provided. The power function is given by:

$$\Delta_E(E) = 135E^{0.386} \tag{8.2}$$

with $\Delta_E(E)$ in $\mathring{A}$ and E in keV. The centre of the implant, given by the range of the particles in the probe, was obtained from the same reference and was also fitted to a power function, resulting in:

$$x_0(E) = 107.8E^{1.397} \tag{8.3}$$

with $x_0(E)$ in $\mathring{A}$ and E in keV. The value of A was obtained from the normalisation of the Gaussian distribution to the total number of particles impinging on the probe with energy E. This was found to be:

$$A(E) = \frac{\Gamma_D(E)}{\Delta_E(E)\sqrt{\pi}} \tag{8.4}$$

The total contribution of the CX neutrals to the depth distribution is:

$$f'(x) = \int_0^\infty A(E) \exp -\frac{(x - x_0(E))^2}{\Delta_E(E)^2} dE \tag{8.5}$$

This depth distribution was then folded with the depth resolution of the detection system for the ERD measurements, with the depth resolution $\Delta_{det} \sim 150$ $\mathring{A}$, and assumed constant. Again a Gaussian distribution was assumed, with

$$f''(x, x_f) = B(x) \exp -\frac{(x - x_f)^2}{\Delta_{det}^2} \tag{8.6}$$

$B(x)$ was obtained in the same way as $A(E)$:

$$B(x) = \frac{f'(x)}{\Delta_{det}\sqrt{\pi}} \tag{8.7}$$

and the final measured distribution was given by:

$$F_{dist}(x_f) = \int_0^{x_{max}} \frac{f'}{\Delta_{det}\sqrt{\pi}} \exp -\frac{(x_f - x)^2}{\Delta_{det}^2} dx \tag{8.8}$$

The flux function $\Gamma(E)$ was obtained by fitting the sum of two power functions to the measured spectra supplied by Fahrbach and Hermann [FAH89]. The two power functions were used to simulate the low-energy (< 3 keV) part of the spectrum, with a much steeper slope as a function of energy, as well as the more slowly varying high-energy (> 3 keV) part. For the discharge used, # 28525, the function fitted to the measured flux was:

$$\Gamma(E) = 1.177 \cdot 10^{10} \exp -0.462E + 7.894 \cdot 10^{-2.280E} \tag{8.9}$$

with E in eV and $\Gamma(E)$ in atoms/s·cm^2· eV·str. The reflection of particles hitting the probe was also taken into account, but the effect was found to be negligible.

Bibliography

[ART64] L. Artsimovich, Controlled themonuclear reactions, Gordon and Breach, New York (1964).

[BEC84] Becker, G., Nucl. Fusion, 24 (1984) 1364.

[BEC88] Becker, G., Nucl. Fusion, 28 (1988) 1458.

[BEH75] Behrisch, R. and Kadomtsev, B. B., IAEA - CN - 33/S2(1975)229.

[BEH86] Behrisch, R. and Eckstein, W., in Physics of Plasma - Wall Interactions in Controlled Fusion Devices, Ed. D. E. Post and R. Behrisch, NATO ASI Series B: Physics, Vol. 131, 1974.

[BEH86A] Behringer, K. H., *et al.*, Proc. 13th European Conf. on Cont. Fusion and Plasma Heating, Schliersee (1986)176.

[BEH87] Behrisch, R., *et al.*, Proc. 14th European Conf. on Cont. Fusion and Plasma Heating, Madrid, (1987)778.

[BEH89] R. Behrisch, W. Möller, J. Roth and B. M. U. Scherzer, Nucl. Fusion, Vol. 29, No. 7(1989)1187.

[BEH89A] Behrisch, R., *et al.*, J. Nucl. Mat. 162 - 164(1989)598.

[BEH90] Behrisch, R., Personal Communications.

[BEH90A] Behrisch, R. and Prozesky, V.M., Nucl. Fusion, Vol. 30, No. 10(1990)2166.

[BEL82] Bell, K. L., Atomic and Molecular Data for Fusion, Part 1, "Recommended Cross Sections and Rates for Electron Ionisation of Light Atoms and Ions, CLM R216, Culham Laboratory, Abingdon Oxfordshire (1990).

[BER90] Bergsaker, H., *et al.*, J. Nucl. Mat. 176 & 177(1990)941.

[BOH49] Bohm, D., The characteristics of electrical discharges in magnetic fields, Eds Guthrie, A. and Wakerling, R. K., McGraw - Hill, New York, 1949.

[BOH84] Langley, R. A., In Data Compendium for Plasma Surface Interactions,, Nucl. Fusion, Special Issue, 1984.

[BOR87] Borras, K., Phys. Scr. 16 (1987)107.

[BOS91] Bosch, H. S. and Schumacher, U., Internal Report on the Workshop on Helium Transport and Removal in Gatlinberg, Garching, 1991.

[BRA85] Brambilla, M., and Ottaviani, M., Plasma Phys. Contr. Fusion, 27 1(1985)1.

[BRO83] Brooks, J. N., Nucl. Tech./Fusion 4(1983)33.

[BRO90] Brower, D. L., *et al.*, Phys. Rev. Letters, Vol. 65, No. 3(1990)337.

[CAT77] Cathanei, G. and Croci, R., Nucl. Fusion 17, 2 (1977)239.

[CAT86] M. Caterne, D. A. Thompson and P. T. Wan, Nucl. Instr. and Meth., B15(1986)535.

[CEC80] Cecchi, J. L.,Plasma Surface Interactions in Controlled Fusion Devices, Proc. of the Fourth Int. Conference, Garmisch-Partenkirchen, FRG, 21-25 April 1980.

[CHA90] Chang, C. S., Kaye Imre, and Weitzner, H., Thirteenth Int. Conf. on Plasma Phys. and Controlled Nuclear Fusion, Washington, DC, USA, 1990.

[CHA91A] Chang, C. S., and Hu, S. C., in Workshop on Helium Transport and Removal, Gatlinberg, Tennessee, April 1991.

[CHE74] Chen, F. F., Introduction to Plasma Physics, Plenum Press, New York, 1974.

[CHI83] Chiu, S. C., and Mau, T. K., Nucl. Fusion 23 12(1983)1613 411.

[CHR90] Christiansen, J. P., Cordey, J. G., and Thornsen, K., Nucl. Fus. Vol. 30, No. 7(1990)1183.

[COA89] Coad, J. P., *et al.*, J. Nucl. Mat. 162 & 164(1989)533.

[COH90] Cohen, S. A., in Workshop on Power and Particle Control for ITER, 9 - 10 Jan. 1990, PPL, Princeton University, p. 1.

[COL84] Colestock, P. L.,IEEE Trans. Plasma Phys. 2 2(1984)64.

[COP80A] Coppi, B., Comments on Plasma Phys. and Controlled Fusion, Vol. 5, No. 6(1980)195.

[COP80] Coppi, B., Comments on Plasma Phys. and Controlled Fusion, Vol. 5, No. 6(1980)225.

[COR89] Corti, S., Private Communication.

[DNE79] Dnestrovskij, Y. N., Lysenko, S. E. and Kislyakov, A. I., Nucl. Fusion, Vol. 19, No. 3(1979)293.

[DOL82] Dolan, T. J., Fusion Research, Principles, Vol. 1, Pergamon Press, New York, 1982.

[EHR89] Ehrenberg, J., J. Nucl. Mat. 162 - 164(1989)63.

[ENG78] Engelhardt, W., and Feneberg, W., J. Nucl. Mat. 76 & 77(1978)518.

[ENG80] F. Engelmann, A. Nocentini, Comments Plasma Phys. Controll. Fusion, 5(1980)253.

[FAH89] Fahrbach, H. U., and Hermann, W., Personal Communication, 1989.

[FIN90] Finken, K. H., *et al.*, J. Nucl. Mat. 176&177(1990)816.

[FUS89] G. Fussmann and the ASDEX, NI, and ICRH team, J. Nucl. Mater. 162 - 164(1989)14.

[GAL91] J. D. Galambos and Y. K. Marin Peng, Fusion Tech., Vol. 19, Jan 1991, p31.

[GAU90] Gauthier, E. Eckstein, W., László, J., and Roth, J., J. Nucl. Mat., 176 & 177(1990)438.

[GLA64] S. Glasstone and R. H Lovberg, Controlled themonuclear reactions, van Nostrand, Princeton, NJ, Toronto, ,New York, London (1960).

[GON88] Gondhalekar, A., JET-P(88)60.

[GON89] Gondhalekar, A., *et al.*, Plasma Physics and Controlled Fusion, Vol. 31, No. 5(1989)805.

[GOO88] D. H. J. Goodall, G. M. McCracken, J. P. Coad, R. A. Causey, G. Sadler and O. N. Jarvis, J. Nucl. Mat., 162-164, (1989), p1059.

[GRE84] Greenland, P. T.,"Low Energy Charge Capture Cross Sections",Report AERE - R11282, Atomic Energy Establishment, Harwell (1990).

[HAR83] Harrison, M. F. A.,"Applied Atomic Collision Physics", Ed. Massey, H. S. W., McDaniel, E. W. and Bederson, B., Academic Press, New York and London (1990)395.

[HAR84] Harrison, M. F. A., "Atomic and Molecular Collisions in the Plasma Boundary, NATO ASI, Val Morin, Canada, 1984.

[HAR86] Harrison, M. F. A., in Physics of Plasma - Wall Interactions in Controlled Fusion Devices, Ed. D. E. Post and R. Behrisch, NATO ASI Series B: Physics, Vol. 131, 1974.

[HAW89] N. Hawkes, Z. Wang, and R. Bransley, Controlled Fusion and Plasma Physics, Vol. 13B, part 1, European Physical Society (1989)79.

[HEI82] Heifetz, D. B., *et al.*, J. Comp. Phys. 46(1982)309.

[HEI86] Heifetz, D. B., in Physics of Plasma - Wall Interactions in Controlled Fusion Devices, Ed. D. E. Post and R. Behrisch, NATO ASI Series B: Physics, Vol. 131, 1974.

[HIL91] Hillis, D. L., in Workshop on Helium Transport and Removal, Gatlinberg, Tennessee, April 1991.

[HOG90] O' Rourke, J., Sips, A. C. C., de Haas, J. C. M., European Physical Society, Amsterdam 1990 p 158.

[HOG91] Hogan, J., in Workshop on Helium Transport and Removal, Gatlinberg, Tennessee, April 1991.

[HOW82] Howe, H. C., J. Nucl. Mat. 111 - 112(1982)424.

[HUG78] Hughes, M. H. and Post, D. E., J. Comp. Phys. 28(1978)43.

[IGI90] Igitkhanov, Yu. L., J. Nucl. Mat. 176 & 177(1990)102.

[BUR90] Bureš, M. *et al.*, J. Nucl. Mat. 176 & 177(1990)387.

[JEN77] Jensen, R. V. *et al.*, Nucl. Fusion 17, 6 (1977) 1187.

[KAU85] M. Kaufmann, K. Lackner, J. Neuhauser and H. Vernickel, Nucl. Fusion 25(1985)89.

[KEI90] M. Keilhacker and the JET team, Phys. Fluids B2(1990)1291.

[KRA87] A. Krauss, H. W. Becker, H. P. Trautretter, C. Rolfs and K. Brand, Nucl. Phys. A465(1987)150.

[LAN84] Langley, R. A., *et al.*, Nucl. Fus. Special Issue 1984, Data Compendium for Plasma - Surface Interactions, IAEA, Vienna, 1984.

[LAN85] Langer, W. D. and Singer, C. E., Vol. PS-13, No. 3(1985)163.

[LAW57] J. D. Lawson, Proc. Phys. Soc., B70 (1957)6.

[LOM89] Lomas, P. J., JET-P(89)09.

[MAN86] Manning, H. L., *et al.*, Nucl. Fusion 26 12(1986)1665.

[MAN91] Mandrekas, J., and Stacey, W. M. Jr., Fusion Tech. Vol. 19, Jan. 1991 p57.

[MCC87] McCracken, G. M., *et al.*, J. Nucl. Mat. 145 - 147(1987)621.

[MCC87A] McCracken, G. M., Plasma Phys. and Controlled Fusion, Vol. 29, No. 10A(1987)1273.

[MCC89] McCracken, G. M., *et al.*, J. Nucl. Mat. 162 - 164(1989)356.

[MCC90] McCracken, G. M., *et al.*, J. Nucl. Mat., 176&177(1990)392.

[MEA74] Meade, D. M., Nucl. Fusion, 14 (1974) 289.

[MIL74] Miley, G., H.,Tower, H., Ivich, N.,"Fusion Cross Sections and Reactivities", University of Illinois, Report 00-2218-17 (1974).

[MIL89] G. Miley, S. Hu, and V. Varadarajan, "Epithermal - thermal alpha transport and control", Presented at IAEA Technical Committee Meeting on Alpha Particle Confinement and Heating, Kiev, 23 - 26 October 1989.

[NAK91] Nakamura, H., in Workshop on Helium Transport and Removal, Gatlinberg, Tennessee, April 1991.

[NOT86] Noterdaeme, J. M., *et al.*, MPI Report IPP III/110, 1986.

[ONO86] Ono, K., *et al.*, Phys. Rev A, 34 2(1986)1328.

[PEA86] J. M. Pearson, Nuclear Physics, Publ. Adam, Higler Ltd, Bristol, England.

[PER89] Perkins, F. W., Nucl. Fusion, 29 4(1989)583.

[PIT88] Pitcher, C. S., *et al.*, Contrib. Plasma Physics 28(1988)489.

[POS91] Post, D., in Workshop on Helium Transport and Removal, Gatlinberg, Tennessee, April 1991.

[RAE81] J. Raeder *et al.*, Kontrollierte Kernfusion, Teubner, Stuttgart (1981).

[RED89] Redi, M. H. and Cohen, S. A., Report PPPL2641, Princeton Plasma Physics Laboratory, Princeton University, Princeton, NJ 08543, 1989.

[RED90] Redi, M. H. and Cohen, S. A., J. Nucl. Mat., 176 & 177(1990)262.

[RED91] Redi, M. H., Cohen, S. A. and Synakowski, E. J. Nucl. Fusion, Vol. 31, No. 9(1991)1689.

[REI89] Reichle, R. R., *et al.*, Proc. 1st European Conference on Application of Accelerators in Research and Technology. (1989).

[REI90] Reiter, D., Wolf, G. H. and Kever, H., Report Jül-2342, KFA, Forschungszentrum Jülich GmbH, Institut für Plasmaphysik, Association EURATOM-KFA, January 1990.

[REI90A] Reiter, D., Wolf, G. H., and Kever, H., J. Nucl. Mat. 176 & 177(1990)756.

[ROB74] Robinson, M., *et al.*, Phys. Rev. B9(1974)5008.

[ROQ85] Roquemore, A. L., *et al.*, Rev. Sci. Instr., 58(1985)1120.

[ROT80] J. Roth and G. Janeschitz, Nucl. Fusion, 29(1989)915.

[ROT90] J. Roth, R. Behrisch, W. Möller, and W. Ottenberger, Nucl. Fusion, Vol. 30, No. 3, 1990.

[SAG89] Sager, G. T., DOE/ER/52127 - 36, US Dept. of Energy, 1989.

[SAR90] R. Sartori, G. Saibene, D. H. J. Goodall, E. Usselman, P. Coad and D. Holland, J. Nucl. Mat., 176 & 177, (1990)624.

[SCI90] Scientific American, Special Edition, September 1990.

[SIP89] A. C. C. Sips, J. C. M. de Haas, G. M. D. Hogeweij, R. Prentice, and A. E. Costley, Bull. Am. Phys. Soc., 34 9(1989)2055.

[SOD88] Söder, B., IPP Report 9/63, 1988.

[STA80] Staudenmaier, G., *et al.*, Nucl. Fusion 20 1(1980)96.

[STA88] Stangeby, P., Contrib. Plasma Phys. 28(1988)501.

[STA88A] Staudenmaier, G.and Wampler, W. R., J. Nucl. Mat., 162 & 164(1989)414.

[STA90] Stangeby, P. C., and McCracken, G. M., Nucl. Fus. Vol. 30, No. 7(1990)1225.

[STE89] Stevens, J. E., *et al.*, Princeton Report PPPL - 2680, 1989.

[STI75] Stix, T. H., Nucl. Fusion, 15 (1975)737.

[STR89] Stroth, U., *et al.*, Nucl. Fusion, 29(1989)789.

[SYN91] Synakowski, E., in Workshop on Helium Transport and Removal, Gatlinberg, Tennessee, April 1991.

[TAY90] Taylor, R. J., Fried, B. D., and Morales, G. J., Comments on Plasma Phys. and Controlled Fusion, Vol. 13, No. 5(1990)227.

[THO90] Thomas, P. R., and the JET Team, J. Nucl. Mat. 176 & 177(1990)3.

[TOM88] K. Tomabechi, Plasma Phys. and Controlled Nucl. Fusion Research 1988, Proc. 12th Int. Conf, Nice, Vol. 3 IAEA, Vienna, (1989)215.

[UCK88] Uckan, N. A. *et al.*, Fusion Technology 13 (1988) 411.

[UCK88A] Uckan, N. A., and International Thermonuclear Experimental Reactor Physics Group (1988).

[VER78] Vernickel, H. and Bohdansky, J., Nucl. Fusion 18, 10 (1978) 1467.

[WAG82] Wagner, F., J. Vac. Sci. Technol., 20(1982)1211

[VER89] Verbeek, H., *et al.*, J. Nucl. Mat. 162 - 164(1989)557.

[VOJ90] Vojtsenya, V. S., and Cohen, S. A., J. Nucl. Mat., 176 & 177(1990)611.

[WEI75] Weisheit, J. C., J. Phys. B: Atom. Molec. Phys., Vol. 8, No, 15(1975)2556.

[WEY74] Weynants, R. R., Phys. Rev. Letters 33 2(1974)78.

[WES87] Wesson, J., Tokamaks, Oxford Engineering Science Series No. 20, Oxford Science Publications, Clarendon Press, Oxford, 1987, p83.

[WES90] Wesner, F., Prozesky, V. M., Behrisch, R., and Staudenmaier, G., Fusion Engineering and Design, 12(1990)193.

[ZIE77] H. H. Andersen and J. F. Ziegler, Hydrogen Stopping Powers and Ranges in all elements, Pergamon Press, 1977.

[ZIE77A] Ziegler, J. F., and Anderson, H. H., Stopping Powers and Ranges of Ions in Matter, Vol. 3, Pergamon Press, 1977.